



NAVAL POSTGRADUATE SCHOOL

MONTEREY, CALIFORNIA

THESIS

**QUANTUM TUNNELING MODEL OF A P-N JUNCTION
IN SILVACO**

by

Jeffrey Lavery

September 2008

Thesis Advisor:
Second Reader:

Sherif Michael
Todd Weatherford

Approved for public release; distribution is unlimited

THIS PAGE INTENTIONALLY LEFT BLANK

REPORT DOCUMENTATION PAGE			<i>Form Approved OMB No. 0704-0188</i>	
Public reporting burden for this collection of information is estimated to average 1 hour per response, including the time for reviewing instruction, searching existing data sources, gathering and maintaining the data needed, and completing and reviewing the collection of information. Send comments regarding this burden estimate or any other aspect of this collection of information, including suggestions for reducing this burden, to Washington headquarters Services, Directorate for Information Operations and Reports, 1215 Jefferson Davis Highway, Suite 1204, Arlington, VA 22202-4302, and to the Office of Management and Budget, Paperwork Reduction Project (0704-0188) Washington DC 20503.				
1. AGENCY USE ONLY (Leave blank)		2. REPORT DATE September 2008	3. REPORT TYPE AND DATES COVERED Master's Thesis	
4. TITLE AND SUBTITLE Quantum Tunneling Model of a P-N Junction in Silvaco			5. FUNDING NUMBERS	
6. AUTHOR(S) Jeffrey Lavery				
7. PERFORMING ORGANIZATION NAME(S) AND ADDRESS(ES) Naval Postgraduate School Monterey, CA 93943-5000			8. PERFORMING ORGANIZATION REPORT NUMBER	
9. SPONSORING /MONITORING AGENCY NAME(S) AND ADDRESS(ES) N/A			10. SPONSORING/MONITORING AGENCY REPORT NUMBER	
11. SUPPLEMENTARY NOTES The views expressed in this thesis are those of the author and do not reflect the official policy or position of the Department of Defense or the U.S. Government.				
12a. DISTRIBUTION / AVAILABILITY STATEMENT Approved for public release: distribution is unlimited			12b. DISTRIBUTION CODE	
13. ABSTRACT (maximum 200 words) The focus of this research is to accurately model the tunnel junction interconnect within a multi-junction photovoltaic cell. A physically based 2-D model was created in Silvaco Inc.'s ATLAS [®] software to model the quantum tunneling effect that is realized within a multi-junction cell. The tunnel junction interconnect is a critical factor in the design of multi-junction photovoltaics and the successful modeling of the junction will lead to the ability to design more efficient solar cells. The quantum tunneling effect is based on the non-local band-to-band and trap assisted tunneling probability described by the Wentzel-Kramers-Brillouin (WKB) method.				
14. SUBJECT TERMS Quantum tunneling, multi-junction photovoltaic cell, Silvaco, Wentzel-Kramers-Brillouin.			15. NUMBER OF PAGES 119	
			16. PRICE CODE	
17. SECURITY CLASSIFICATION OF REPORT Unclassified	18. SECURITY CLASSIFICATION OF THIS PAGE Unclassified	19. SECURITY CLASSIFICATION OF ABSTRACT Unclassified	20. LIMITATION OF ABSTRACT UU	

NSN 7540-01-280-5500

Standard Form 298 (Rev. 2-89)
Prescribed by ANSI Std. Z39-18

THIS PAGE INTENTIONALLY LEFT BLANK

Approved for public release; distribution is unlimited

QUANTUM TUNNELING MODEL OF A P-N JUNCTION IN SILVACO

Jeffrey B. Lavery
Lieutenant, United States Navy
B.S./ B.A., University of San Diego, 2003

Submitted in partial fulfillment of the
requirements for the degree of

MASTER OF SCIENCE IN ELECTRICAL ENGINEERING

from the

**NAVAL POSTGRADUATE SCHOOL
September 2008**

Author: Jeffrey Lavery

Approved by: Sherif Michael
Thesis Advisor

Todd Weatherford
Second Reader

Jeffrey B. Knorr
Chairman, Department of Electrical and Computer Engineering

THIS PAGE INTENTIONALLY LEFT BLANK

ABSTRACT

The focus of this research is to accurately model the tunnel junction interconnect within a multi-junction photovoltaic cell. A physically based 2-D model was created in Silvaco Inc.'s software to model the quantum tunneling effect that is realized within a multi-junction cell. The tunnel junction interconnect is a critical factor in the design of multi-junction photovoltaics and the successful modeling of the junction will lead to the ability to design more efficient solar cells. The quantum tunneling effect is based on the non-local band-to-band and trap assisted tunneling probability described by the Wentzel-Kramers-Brillouin (WKB) method.

THIS PAGE INTENTIONALLY LEFT BLANK

TABLE OF CONTENTS

I.	INTRODUCTION.....	1
A.	BACKGROUND	1
B.	OBJECTIVES AND APPROACH.....	1
C.	RELATED WORK	2
D.	ORGANIZATION	2
II.	SEMICONDUCTOR PHYSICS.....	3
A.	MATERIAL SCIENCE AND BOHR'S MODEL.....	3
B.	CRYSTAL STRUCTURE.....	6
C.	CARRIERS.....	8
D.	ENERGY BANDS.....	10
E.	INTRINSIC SEMICONDUCTORS AND DOPING	12
F.	FERMI LEVEL.....	14
G.	MOBILITY.....	17
H.	CURRENT DENSITY	18
I.	GENERATION AND RECOMBINATION	20
J.	SUMMARY	23
III.	P-N JUNCTIONS.....	25
A.	INTRODUCTION TO JUNCTIONS.....	25
B.	BASIC STRUCTURE.....	25
C.	REVERSE BIAS	28
D.	FORWARD BIAS	30
E.	BREAKDOWN/ZENER TUNNELING	33
F.	LOSSES	34
G.	SUMMARY	35
IV.	TUNNEL JUNCTION.....	37
A.	TUNNELING THEORY	37
B.	PURPOSE.....	37
C.	THE JUNCTION	40
D.	THERMAL EQUILIBRIUM.....	41
E.	REVERSE BIAS	42
F.	FORWARD BIAS	43
G.	NEGATIVE RESISTANCE.....	44
H.	THERMAL CURRENT FLOW.....	45
I.	DIRECT AND INDIRECT TUNNELING	47
J.	TUNNELING CURRENT.....	48
K.	WENTZEL-KRAMERS-BRILLOUIN METHOD (WKB).....	49
L.	SUMMARY	52
V.	SIMULATION SOFTWARE	53
A.	SILVACO	53
B.	ATLAS [®] /DECKBUILD.....	53

C.	SYNTAX	54
D.	STRUCTURE SPECIFICATION	55
1.	Mesh	55
2.	Region.....	57
3.	Electrode	57
E.	QUANTUM TUNNELING MESH	59
F.	MATERIAL MODELS SPECIFICATION	60
1.	Material.....	60
2.	Models	60
3.	Contact	60
G.	NUMERICAL METHOD SELECTION.....	61
H.	SOLUTION SPECIFICATION.....	61
1.	Log.....	61
2.	Solve	61
3.	Save.....	62
I.	RESULTS ANALYSIS	62
VI.	TUNNEL JUNCTION RESULTS.....	65
A.	SEMICONDUCTOR MATERIAL	65
B.	TUNNEL JUNCTION DOPING	66
1.	GaAs Tunnel Junction.....	67
2.	InGaP Tunnel Junction	70
C.	SUMMARY	73
VII.	SOLAR CELL IMPLEMENTATION.....	75
A.	SOLAR RADIATION	75
B.	I-V CURVE.....	75
C.	SINGLE CELL.....	77
D.	MULTI CELLS	80
VIII.	RECOMMENDATIONS AND CONCLUSION.....	83
A.	RECOMMENDATIONS.....	83
1.	Physical Experiment	83
2.	Other Software	83
3.	Temperature and Radiation Effects.....	84
B.	CONCLUSION	84
APPENDIX.	ATLAS [®] SOURCE CODE	85
A.	MAIN STRUCTURE.....	85
B.	TUNNEL JUNCTION	85
C.	COMMON SECTIONS.....	86
D.	INGAAS / GAAS SINGLE AND DUAL JUNCTION CELL.....	88
	LIST OF REFERENCES.....	97
	INITIAL DISTRIBUTION LIST	99

LIST OF FIGURES

Figure 1.	Resistivity for various material types, from [4].	4
Figure 2.	Bohr's model of allowable electron orbits in a hydrogen atom, from [5].	5
Figure 3.	Degree of atomic order classification within solids: (a) amorphous (b) polycrystalline (c) crystalline, from [5].	6
Figure 4.	Breavais lattice cubics, from [6].	7
Figure 5.	Cubic-Diamond lattice structure, from [6].	8
Figure 6.	Intrinsic carrier density vs. Temperature, from [7].	10
Figure 7.	Energy band diagrams, from [8].	11
Figure 8.	Energy band structure vs. wave vector for Ge, Si and GaAs, from [7].	12
Figure 9.	Fermi distribution function, from [5].	15
Figure 10.	Schematic band diagram, density of states, Fermi-Dirac distribution and the carrier concentrations for intrinsic, n-type and p-type semiconductors at thermal equilibrium, from [7].	16
Figure 11.	Mobility vs. doping level, from [7].	18
Figure 12.	Diffusion current, from [2].	19
Figure 13.	Drift current in the presence of an electric field, from [2].	20
Figure 14.	Energy band visualization of recombination and generation processes, from [5].	22
Figure 15.	(a) Simplified P-N junction; (b) doping profile, from [9].	25
Figure 16.	P-N junction depletion region formed by diffusion, from [9].	26
Figure 17.	P-N junction energy band diagram with Fermi level.	27
Figure 18.	Reversed bias p-n junction schematic, from [2].	28
Figure 19.	Reversed bias p-n junction energy band diagram.	29
Figure 20.	Reversed bias p-n junction I-V characteristic.	30
Figure 21.	Forward bias p-n junction schematic, from [2].	31
Figure 22.	Forward bias p-n junction energy band diagram.	32
Figure 23.	Forward bias p-n junction I-V characteristic.	33
Figure 24.	Zener breakdown p-n junction I-V characteristic.	34
Figure 25.	p-n junction I-V characteristic.	35
Figure 26.	Tandem solar cells.	38
Figure 27.	Tandem solar cell with parasitic junction.	38
Figure 28.	Tandem solar cell example with oxide/conductor contact separation, from [2].	39
Figure 29.	Tandem cell with tunnel junction.	40
Figure 30.	Degenerately doped tunnel junction energy band diagram.	41
Figure 31.	Tunnel junction energy band and I-V characteristic at thermal equilibrium, from [7].	42
Figure 32.	Tunnel junction energy band and I-V characteristic in forward bias (reverse bias), from [7].	43
Figure 33.	Tunnel junction energy band and I-V characteristic in forward bias (peak tunneling), from [7].	44

Figure 34.	Tunnel junction energy band and I-V characteristic in forward bias (negative resistance), from [7].	45
Figure 35.	Tunnel junction energy band and I-V characteristic in forward bias (thermal current flow), from [7].	46
Figure 36.	Characteristic I-V curve of a tunnel (red) and conventional (blue) p-n junction.	46
Figure 37.	(a) Direct band tunneling process. (b) Indirect band tunneling process, from [7]	48
Figure 38.	Triangular potential barrier for tunneling model, from [7]	50
Figure 39.	Silvaco Inc.'s simulation environment, from [10].	54
Figure 40.	ATLAS [®] command groups with the primary statements in each group, from [11].	55
Figure 41.	Tunnel junction mesh.	56
Figure 42.	Tunnel junction region.	57
Figure 43.	Tunnel junction qtx.mesh and qty.mesh.	59
Figure 44.	Silicon tunnel junction I-V curve in ATLAS [®]	63
Figure 45.	GaAs tunnel junction ($p = 3e20/cm^3$ $n = 9e18/cm^3$) (A/cm^2 versus volts in a $1\mu m$ thick junction).	65
Figure 46.	InGaP tunnel junction ($p = 2e20/cm^3$ $n = 9e18/cm^3$) (A/cm^2 versus volts in a $1\mu m$ thick junction).	66
Figure 47.	GaAs IV characteristics and energy band diagram ($p = 1e20/cm^3$ $n = 9e18/cm^3$) (A/cm^2 versus volts in a $1\mu m$ thick junction).	67
Figure 48.	GaAs IV characteristics and energy band diagram ($p = 3e20/cm^3$ $n = 9e18/cm^3$) (A/cm^2 versus volts in a $1\mu m$ thick junction).	68
Figure 49.	GaAs IV characteristics and energy band diagram ($p = 6e20/cm^3$ $n = 9e18/cm^3$) (A/cm^2 versus volts in a $1\mu m$ thick junction).	68
Figure 50.	GaAs IV characteristics and energy band diagram ($p = 3e20/cm^3$ $n = 6e18/cm^3$) (A/cm^2 versus volts in a $1\mu m$ thick junction).	69
Figure 51.	GaAs IV characteristics and energy band diagram ($p = 3e20/cm^3$ $n = 9e18/cm^3$) (A/cm^2 versus volts in a $1\mu m$ thick junction).	69
Figure 52.	GaAs IV characteristics and energy band diagram ($p=3e20/cm^3$ $n=2e19/cm^3$) (A/cm^2 versus volts in a $1\mu m$ thick junction).	70
Figure 53.	InGaP IV characteristics and energy band diagram ($p = 8e19/cm^3$ $n = 9e18/cm^3$) (A/cm^2 versus volts in a $1\mu m$ thick junction).	70
Figure 54.	InGaP IV characteristics and energy band diagram ($p = 2e20/cm^3$ $n = 9e18/cm^3$) (A/cm^2 versus volts in a $1\mu m$ thick junction).	71
Figure 55.	InGaP IV characteristics and energy band diagram ($p = 4e20/cm^3$ $n = 9e18/cm^3$) (A/cm^2 versus volts in a $1\mu m$ thick junction).	71
Figure 56.	InGaP IV characteristics and energy band diagram ($p = 2e20/cm^3$ $n = 6e18/cm^3$) (A/cm^2 versus volts in a $1\mu m$ thick junction).	72
Figure 57.	InGaP IV characteristics and energy band diagram ($p = 2e20/cm^3$ $n = 9e18/cm^3$) (A/cm^2 versus volts in a $1\mu m$ thick junction).	72
Figure 58.	InGaP IV characteristics and energy band diagram ($p = 2e20/cm^3$ $n = 2e19/cm^3$) (A/cm^2 versus volts in a $1\mu m$ thick junction).	73

Figure 59.	(a) Dark (blue) and illuminated (red) current characteristic curve of the solar cell. (b) Solar cell current characteristic curve with FF.	76
Figure 60.	Optimized InGaP cell structure.....	78
Figure 61.	Optimized InGaP I-V curve. (A/cm^2 versus voltage).	78
Figure 62.	Optimized GaAs cell structure.....	79
Figure 63.	Optimized GaAs I-V curve. (A/cm^2 versus voltage).	79
Figure 64.	Multi-junction solar cell (InGaP/GaAs) with tunnel junction.	80
Figure 65.	Multi-junction solar cell (InGaP/GaAs) I-V curve. (A/cm^2 versus voltage).	81
Figure 66.	Optimized multi-junction solar cell (InGaP/GaAs) I-V curve. (A/cm^2 versus voltage).....	82

THIS PAGE INTENTIONALLY LEFT BLANK

LIST OF TABLES

Table 1.	Intrinsic carrier concentration at room temperature (300K).....	13
----------	---	----

THIS PAGE INTENTIONALLY LEFT BLANK

EXECUTIVE SUMMARY

The production of electrical power is of growing concern in today's world. Renewable energy has been on the forefront of this issue and continues to provide promising results. Biofuels, wind turbines, hydroelectric, and geothermal energy are all sources of renewable energy. However, solar energy has proven to be a viable candidate for many niche applications. Whenever there is a need for a small, lightweight, low to no maintenance, completely independent source of energy, photovoltaic solar cells routinely provide a leading solution.

Modern solar cell technology has been around since the 1950s and has greatly matured over the last half century. Solar power has developed into a multi-billion dollar a year industry [1] providing electric power to everything from spacecraft to automobiles. Although photovoltaic cells are a proven technology, there is always room for improvement. One major disadvantage of photovoltaic technology is the power density of the cells, which depends on the cell type and cell location.

One solution to improve photovoltaic power density is to place cells of different material in tandem. These cells are connected with a tunnel junction in order to minimize shadowing of the sub-cells and maximize the number of photons absorbed. According to the DOE, a tunnel junction interconnect is a Tier 2 Technical Improvement Opportunity [1]. The potential for such a highly optimized photovoltaic cell depends on the ability to accurately model the quantum tunneling phenomenon in the tunnel junction.

The focus of this research was to model the quantum tunneling phenomenon in a degenerately doped p-n junction. This was achieved using Silvaco Inc.'s ATLAS[®] software. Silicon (Si), gallium arsenide (GaAs) and indium gallium phosphide (InGaP) tunnel junctions were realized using this software and the affects of varying doping levels in response to a forward bias was investigated.

The validity of the model was tested by implementing the successfully developed tunnel junction into a multi-junction solar cell with a known I-V curve. The multi-junction cell model was developed by Panayiotis Michalopoulos [2] and the model was

compared to the experimental data found by the Central Research Laboratory, Japan Energy Corporation [3]. The simulated power density was calculated to be within 3.8% difference from the experimental results.

ACKNOWLEDGMENTS

Many contributions were made in the process of this research. First, I would like to thank my advisor, Prof. Sherif Michael, whose knowledge and guidance on photovoltaic technology was essential to the process and greatly appreciated. Second, I would like to thank Prof. Todd Weatherford for his superb understanding of solid state electronics as well as the time he spent helping me understand the difficult concepts. Both professors were an inspiration to my research and will continue to inspire me in future work. I would also like to thank Dr. Robin Jones of Silvaco Inc. who was of great help with the modeling software.

Lastly, I thank my family for their patience and understanding throughout this process. To my wife Maureen, daughter Rory and son Peter, thank you for your love and encouragement.

THIS PAGE INTENTIONALLY LEFT BLANK

I. INTRODUCTION

A. BACKGROUND

Photovoltaic solar cells are an excellent source of renewable energy in countless applications. From Mars rovers to orbiting satellites, the need for a lightweight, renewable, low maintenance energy source is necessary to extend equipment lifetimes and remain at the leading edge of technology and exploration. UAVs, sensor nodes and entire command posts are all using solar energy to power their systems to remain remote, untethered tools of our military. Even the modern war fighter is becoming more and more reliant on gadget technology including night vision, satellite radios and GPS units, which are routinely issued to provide an advantage over an adversary. Considering these and many other photovoltaic applications, efficiency and size are paramount in research and development.

Currently single cell photovoltaic energy sources are restricted to a small spectrum of emitted energy depending on the semiconductor used. Operating at between 25 to 30% efficiency, the need for more power only increases array weight by requiring more cells to produce a specified output power. To increase efficiency, multi-junction solar cells have been developed in order to absorb a wider array of the solar spectrum. By stacking cells of competing semiconductor material, efficiency can theoretically be increased to upwards of 60%, which would lead to smaller arrays with increased power.

The one flaw to simply stacking cells one on another is the parasitic junction developed at the junction between the solar cells. This problem is solved by manufacturing a tunnel junction between each cell in order to ensure that the current flow in the cell and at the junction is in the same direction.

B. OBJECTIVES AND APPROACH

The purpose of this thesis is to accurately model the quantum tunneling phenomenon within a degenerately doped p-n junction. The junction will be modeled using Silvaco Data System Inc.'s ATLAS[®] software. ATLAS[®] is a multi-physics semiconductor simulation tool which provides the user with the ability to design and

evaluate changes to a product before fabrication. Once designed, the developed junction will be applied to a multi-junction photovoltaic cell in order to increase the efficiency while decreasing the development time and money spent.

C. RELATED WORK

This research is related to a Naval Postgraduate School thesis completed in March 2002 by Panayiotis Michalopoulos titled *A Novel Approach for the Development and Optimization of State-of-the-art Photovoltaic Devices Using Silvaco*. Although this thesis was very successful in optimizing a multi-junction photovoltaic cell, the forward bias I-V characteristic of the tunnel junction was not modeled. The ability to model this detail will further press the optimization of photovoltaic technology.

D. ORGANIZATION

The following two chapters are a discussion of semiconductor physics and how they apply to a standard p-n junction. Chapter IV extrapolates this information and applies it to a degenerately doped tunnel junction. The simulation software along with the tunnel junction simulation code is discussed in Chapter V. The results of the tunnel junction model are presented in Chapter VI followed by the successfully implemented dual-junction solar cell in Chapter VII. Finally, the recommendations and conclusions are presented in Chapter VIII.

II. SEMICONDUCTOR PHYSICS

The basic material properties introduced in this section are essential to the understanding of the following research. Although there are more detailed works on this subject, this discussion will be limited to the essential properties related to silicon (Si), germanium (Ge), gallium arsenide (GaAs) and indium gallium phosphide (InGaP); semiconductors typical to photovoltaic applications.

A. MATERIAL SCIENCE AND BOHR'S MODEL

One common way to categorize a material is by its electrical properties. Depending on the level of an element's resistivity, it can be categorized as an insulator, conductor, or semiconductor. The ability of a material to resist or conduct electricity is dependent on many factors, including lattice structure, free electrons, energy bandgap, and temperature. Some materials have very discrete electrical properties which define them as either an insulator or conductor. However, other materials such as silicon (Si) and gallium arsenide (GaAs) can act as either an insulator or conductor and are therefore considered semiconductors. Figure 1 shows the typical range of conductivities for insulators, conductors, and semiconductors.

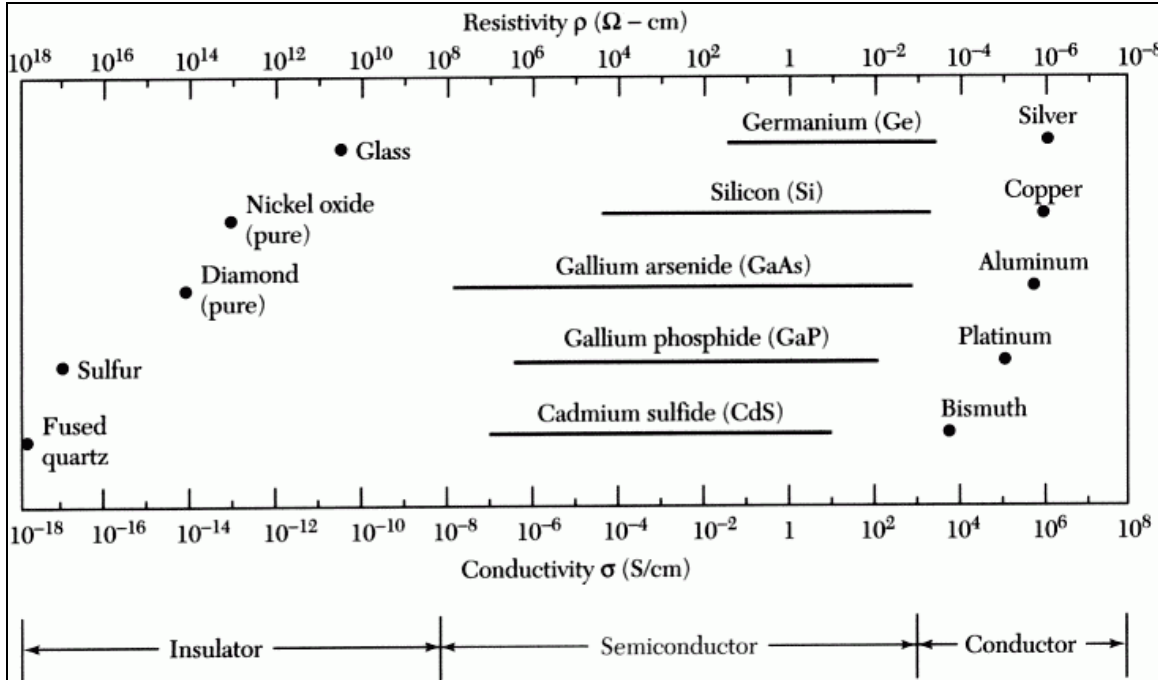


Figure 1. Resistivity for various material types, from [4].

Bohr's model can be derived as a first order approximation of quantum mechanics yet its simplicity is valuable to the understanding of the electrical characteristics of materials on a large scale. According to Niels Bohr, atoms are comprised of three subatomic particles: a negative charged electron, a positive charged proton, and a neutron with no charge. Compared to the electron, the high mass proton and neutron form what is known as the nucleus, which sits at the center of the model. The electron, which is about 1,836 times smaller than the proton, revolves around the nucleus at a specific energy level known as an orbit or shell. The three subatomic particles are held together by the electrostatic force between the electron and proton similar to the way planets are held in orbit by gravity. Each shell must contain a set number of electrons before the outermost shell, known as the valence shell, can be occupied.

Modeling the simplest of atomic structures, the hydrogen atom, Bohr assumes that an electron in orbit around the nucleus can take on only certain levels of angular momentum ($n\hbar$). This quantization of the electron's angular momentum is then related to the electron's energy level by Equation 2.1 below, where m_0 is the mass of a free

electron, q is the electron charge, ε_0 is the permittivity of free space, n is the electron orbit and \hbar is the reduced Plank's constant $\left(\hbar = \frac{h}{2\pi}\right)$.

$$E_H = -\frac{m_0 q^4}{2(4\pi\varepsilon_0 n \hbar)^2} = -\frac{13.6}{n^2} eV \quad \text{Eqn. 2.1}$$

As explained by Equation 2.1 and Figure 2, it is clear that as the orbits increase, the energy at that particular orbit also increases by a factor of the orbit squared. It also follows that for an electron to move from an outer orbit to an inner orbit ($E_2 - E_1$), it must give off some of its energy, which it does in the form of light at a discrete wavelength (Eqn. 2.2).

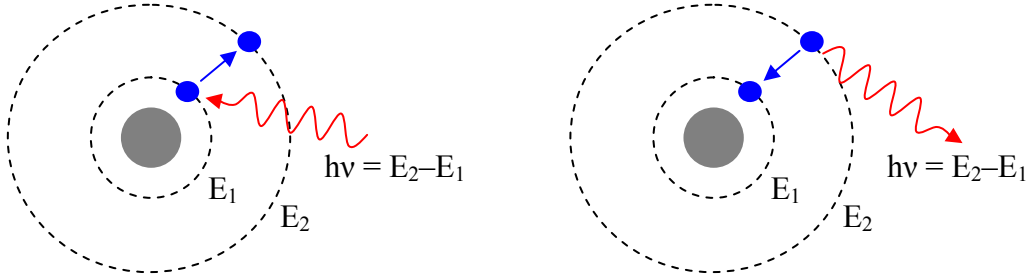


Figure 2. Bohr's model of allowable electron orbits in a hydrogen atom, from [5].

$$\lambda = \frac{hc}{E} \quad \text{Eqn. 2.2}$$

As I will discuss later, this requirement of an electron to lose energy in order to move from an outer shell to an inner shell is the same principle a solar cell uses to absorb light and generate power.

B. CRYSTAL STRUCTURE

The spatial arrangement of the atoms within a physical structure greatly affects the precise properties of a given material. As Figure 3 illustrates, a solid can be classified into three separate degrees of atomic order: amorphous, polycrystalline and crystalline. Amorphous structures are arranged in such a way that any one section within the structure is different from any other section. Crystalline structures are arranged such that the atoms are arranged in the same manner throughout the solid. Polycrystalline structures are a combination of both amorphous and crystalline. Although it is possible for a semiconductor to be arranged in any of the three atomic order classifications, polycrystalline solids are most prominent in today's market due to cost, ease of manufacturing and adequate reliability in photovoltaic applications.

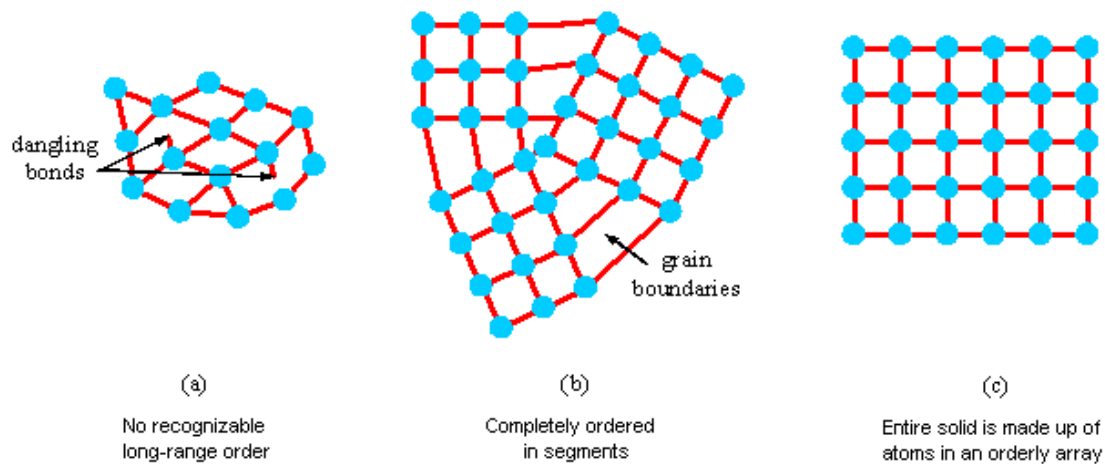


Figure 3. Degree of atomic order classification within solids: (a) amorphous (b) polycrystalline (c) crystalline, from [5].

The atomic structure of a semiconductor can be further described by its lattice structure within a unit cell. The typical way to describe an atomic structure is to use the Brevais lattice system, which describes the symmetry of a crystal by the three-dimensional (3-D) geometric arrangement of the atoms in it. Although there are seven separate categories within the Brevais system with fourteen total arrangements, the simplest of the arrangements can be divided into three categories: the simple cubic, body-centered cubic and face-centered cubic (Figure 4).

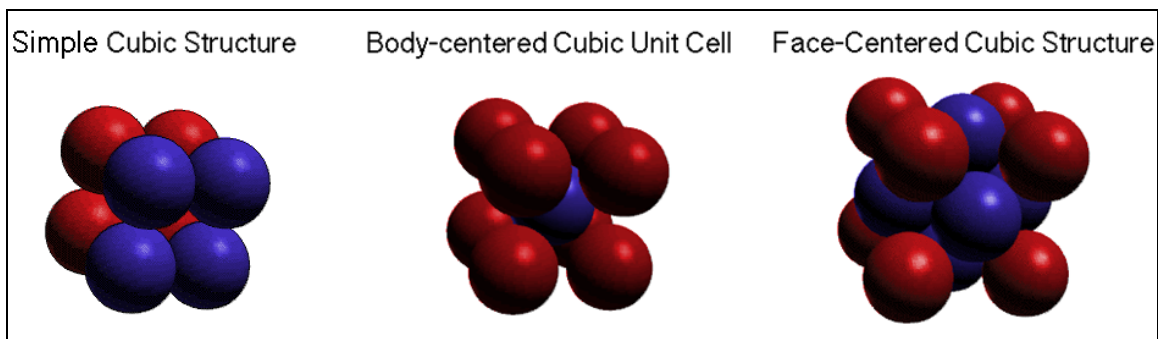


Figure 4. Brevais lattice cubics, from [6].

Taking a closer look at the lattice structure of an element with four valence electrons, such as carbon, silicon and germanium, there are small differences from the lattice structures described above and those of the group IV elements (those with four valence electrons). Figure 5 is a diamond lattice in which two face centered cubic lattices are interpenetrating. The blue and green spheres represent the first interpenetrating face centered cubic and the light blue sphere represents the second interpenetrating face centered cubic. The second face centered cubic is diagonally shifted $\frac{1}{4}$ of the unit distance. All element IV semiconductors are described as having cubic-diamond lattice and are so named because each falls under the carbon element, which is the basic building block of diamond. Within this lattice structure each atom is equidistant from its four nearest neighbors. Silicon's and germanium's lattice constants are 5.437 Å and 5.660 Å respectively.

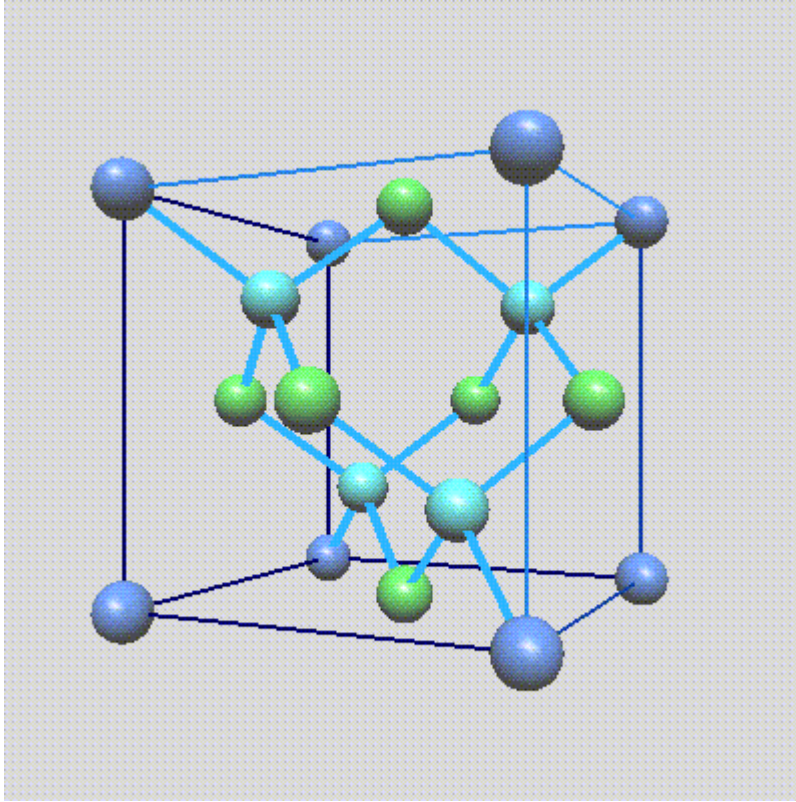


Figure 5. Cubic-Diamond lattice structure, from [6].

C. CARRIERS

Carriers within a material provide an avenue for the transport of an electric charge and therefore electric current. Similar to the Bohr model of the hydrogen atom, the electrons within a Si atom only occur at certain energy levels. However, since the silicon atom is a multi-electron atom, the associated shell model is slightly more complex. The innermost filled shells along with the nucleus are often referred to as the core of the atom because they are tightly bound by the electrostatic force between these shells and the nucleus. The remaining electrons of the atom that fill the outer shell have a weak bond to the core, and are referred to as the valence electrons due to their strong participation in chemical reactions.

Silicon has fourteen electrons, ten of which occupy the two inner most shells (atom core) leaving four valence electrons. When the lattice is formed between the different atoms, there is a finite probability that at any temperature above zero Kelvin (0K), an electron from the valence band will be knocked free and an electron deficiency known as a hole will be left behind. The hole left behind retains a positive charge equal to the absolute value of the electron charge. The free electron along with the hole is known as an electron hole pair (EHP) and can be described by the phenomenon of ionization or generation. When a free electron and hole combine they disappear, a process which is known as recombination. The rate of recombination is proportional to the number of free electrons and existing holes. When in thermal equilibrium the generation and recombination keep the number of EHPs constant. Germanium reacts in much the same way although it has thirty-two total electrons, twenty-eight of which constitute the atom core, leaving four valence electrons. Recombination and generation will be discussed in more detail later.

An intrinsic material has no impurities (doping) in it and will not produce EHPs at 0K. However, the EHPs will increase logarithmically as a function of temperature (Figure 6) and therefore conductivity will also increase.

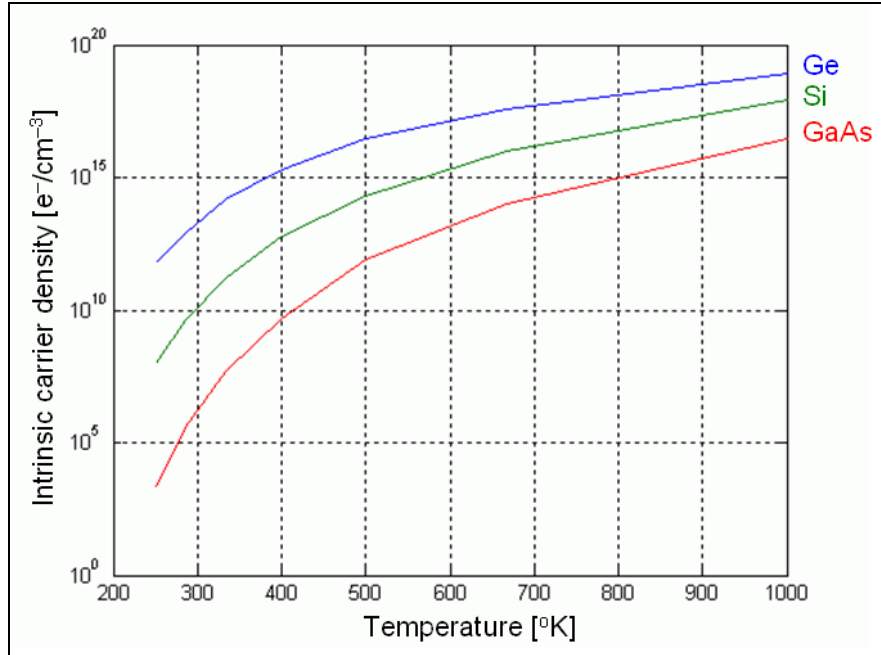


Figure 6. Intrinsic carrier density vs. Temperature, from [7].

D. ENERGY BANDS

The energy band model is a useful way to visualize the differences between an insulator, conductor and semiconductor (Figure 7). When looking at a material rather than a free atom, the electrons within the material form energy bands known as a valence band and conduction band at a specific energy state. The difference between the valence and conduction band is known as the bandgap. The conductivity of a material is dependent on the number of free electrons in the conduction band.

An insulator has a large bandgap that an electron must overcome in order for it to flow in the conduction band. Conversely, a conductor is described as material with the valence and conduction bands overlapping in which case the free electrons do not require any energy to traverse an energy barrier. As expected, a semiconductor has a bandgap that is not overlapping yet the energy difference between the valence and conduction band is minimal.

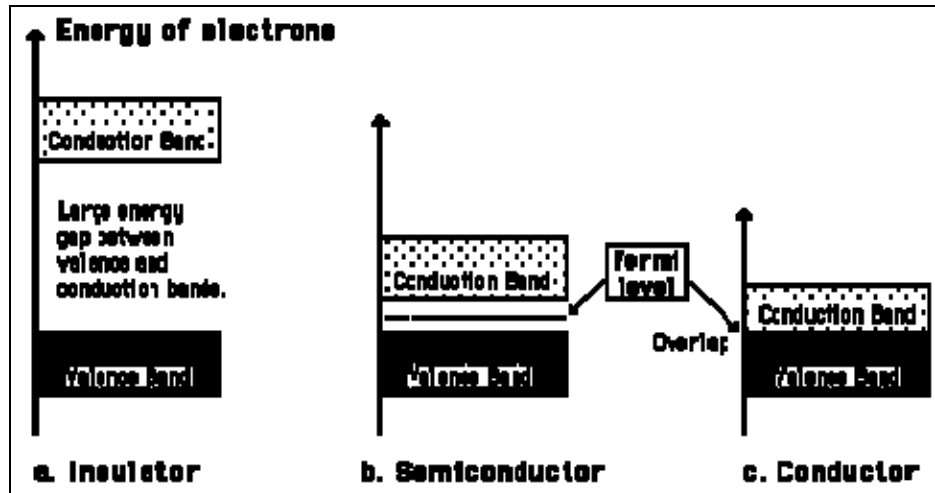


Figure 7. Energy band diagrams, from [8]

Within the energy band there is a distinction between a direct bandgap and an indirect bandgap based on the relative momentum between the valence band hole and the conduction band electron. A direct bandgap semiconductor is one in which the maximum energy level of the valence band and the minimum energy of the conduction band occur at the same momentum. Examples of direct bandgap semiconductors are GaAs and InP which are sometimes referred to as radiant recombination semiconductors because of the band-to-band recombination and release of energy in the form of photons or radiation wavelengths of light.

Indirect bandgap semiconductors have maximum and minimum energy band levels at different momentums. Examples of indirect bandgap semiconductors are Si, Ge and GaP. The energy released during indirect recombination cannot be direct band-to-band and requires the assistance of a third party or defect in the material. This energy is given off in the form of phonons or quasi-particles of quantized sound waves. The energy band structure for Ge, Si and GaAs are compared in Figure 8. This relationship will become more clear when discussing recombination and generation.

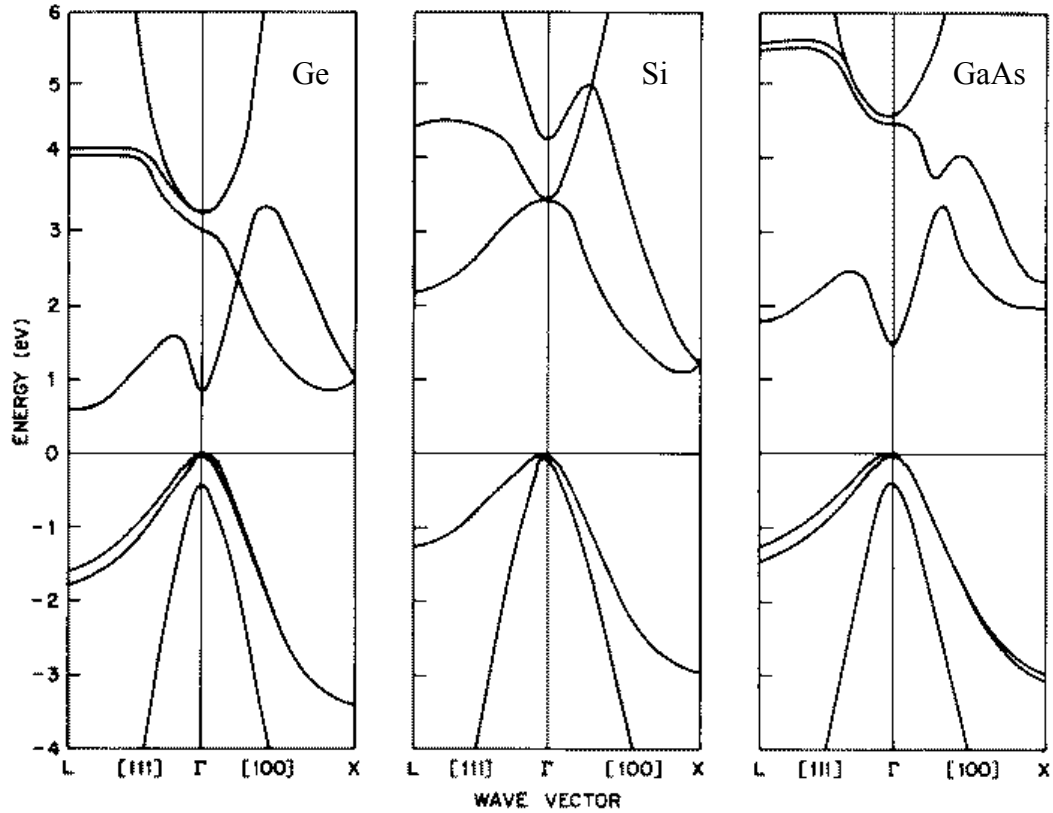


Figure 8. Energy band structure vs. wave vector for Ge, Si and GaAs, from [7].

E. INTRINSIC SEMICONDUCTORS AND DOPING

An intrinsic semiconductor is one with no impurities in it. Therefore, it exhibits properties inherent to the pure semiconductor sample which can be used to identify the material. Under equilibrium conditions, an intrinsic semiconductor has an equal number of holes (p) and electrons (n) which is ultimately equal to the intrinsic carrier concentration (n_i). The number of p and n are equal in an intrinsic semiconductor because carriers are only created in pairs in a highly pure material. If an intrinsic semiconductor bond is broken, a free electron and a hole are created simultaneously. Similarly, if an electron is excited from the valence band to the conduction band then a hole will simultaneously be created in the valence band. A list of common semiconductor materials and their intrinsic carrier concentrations at room temperature are

given in Table 1. Although these concentrations may seem high, they are only a small fraction of the total number of bonds in the respective materials.

Table 1. Intrinsic carrier concentration at room temperature (300K).

Carrier Concentration (n_i) per cm^3	Material
2×10^6	GaAs
1×10^{10}	Si
2×10^{13}	Ge

Adding impurity atoms to a material changes its electrical properties, a process known as doping. Doping is used to control the number of electrons or holes in a material by the addition of a controlled amount of a specific impurity atom. The doping of intrinsic material results in either a p-type or an n-type material, meaning it has an excess number of holes or electrons respectively. With respect to IV elements, acceptors (III elements) are added to produce a p-type material and donors (V elements) are added to produce n-type materials. This is due to the number of valence electrons in the dopant atom. From Section II.A we know that IV elements have four valence electrons. If an element with three valence electrons is added to the diamond lattice the three valence electrons will not be able to complete all of the semiconductor bonds with the element IV atoms. Therefore, the excess electron will continue to be accepted by the dopant atom, and an excess hole will be allowed to wander throughout the structure without the creation of a free electron. Conversely, if a donor is added to the intrinsic element IV material then all the semiconductor bonds will be made, leaving an excess electron to roam throughout the lattice. Only a small amount of dopant, on the order of one atom for every 10^{16} atoms, is required to significantly affect the electrical properties of a material.

F. FERMIL LEVEL

The Fermi level describes the top of the collection of electron energy levels at 0K and is based on the Fermi-Dirac probability equation (Eqn. 2.3). The Fermi-Dirac probability equation is a particle statistic function that determines the distribution of fermions (particles with half-integer spin) at a particular energy state at absolute zero.

$$f(E) = \frac{1}{e^{(E-E_F)/kT} + 1} \quad \text{Eqn. 2.3}$$

At 0K all the available energy states below E_F will be filled by fermions of one and only one particle which are constrained by the Pauli Exclusion Principle. At low temperatures, any energy below the Fermi level will have a probability of 1 and any energy above the Fermi level will have a probability of essentially 0. As the temperature rises, EHPs are created and electrons of higher energy than the Fermi energy emerge in the conduction band. Figure 9 illustrates this distribution for increased temperatures in an intrinsic material.

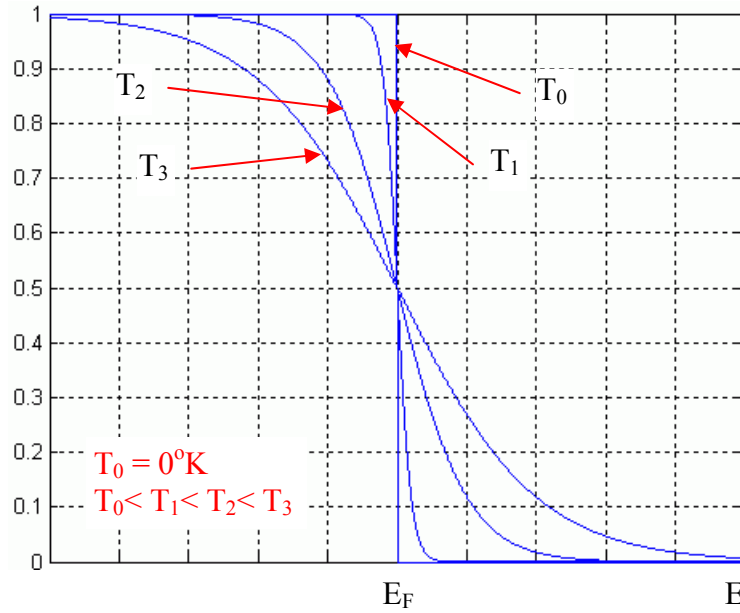


Figure 9. Fermi distribution function, from [5].

The Fermi level can be manipulated by doping the material either with an acceptor or donor, resulting in a p-type or n-type semiconductor respectively. By raising or lowering the Fermi level, one can specify the required energy for an electron to transition from the valence band to the conduction band. As in Figure 10, an intrinsic material has a Fermi level at the center of the band gap. An n-type material shifts the Fermi level closer to the conduction band producing shallow donors. Similarly, a p-type material shifts the Fermi level closer to the valence band producing shallow acceptors. With the Fermi level closer to the valence and conduction bands, only a small amount of energy is required to ionize a hole or electron into their respective bands.

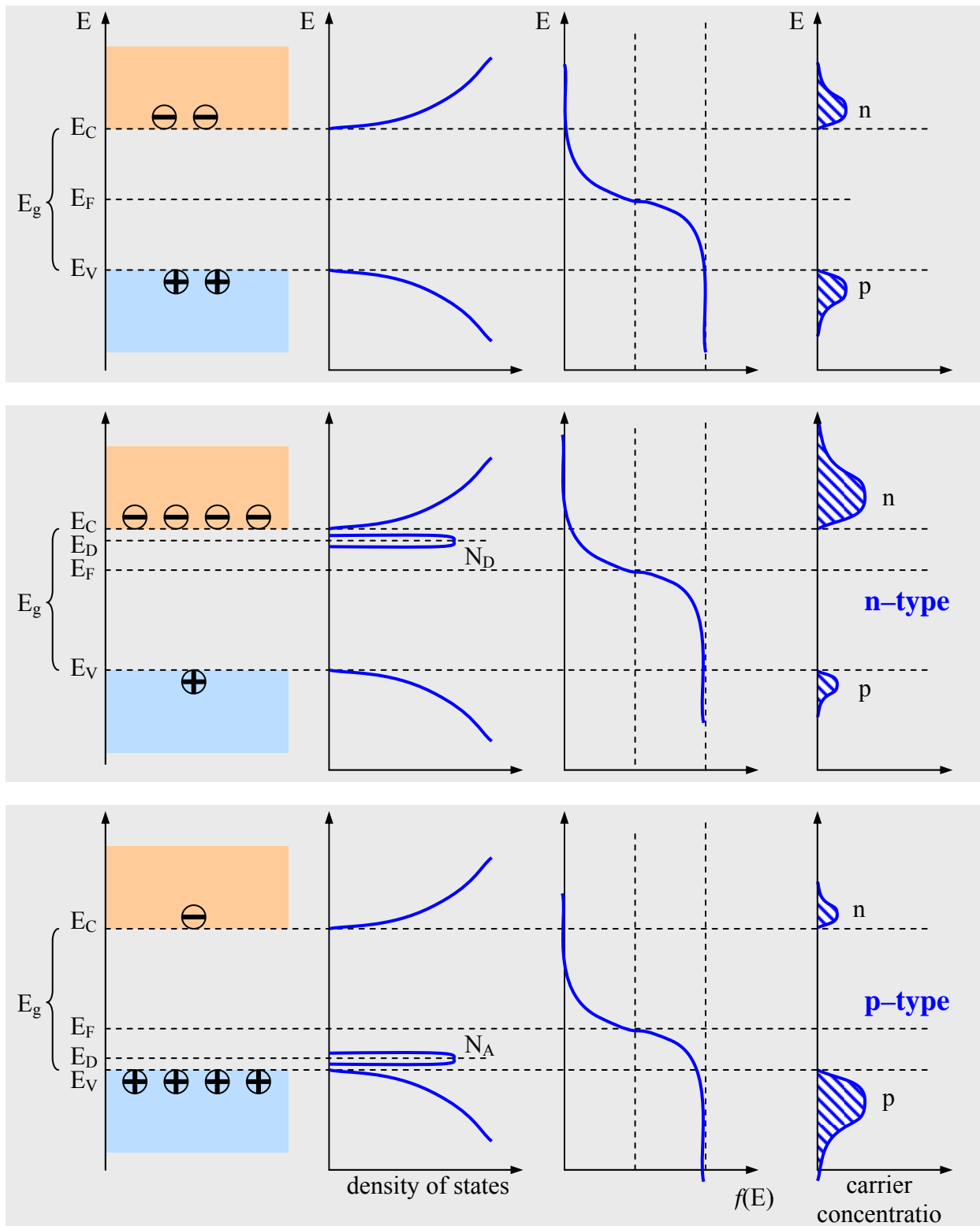


Figure 10. Schematic band diagram, density of states, Fermi-Dirac distribution and the carrier concentrations for intrinsic, n-type and p-type semiconductors at thermal equilibrium, from [7].

When the material is not under equilibrium conditions the Fermi level is influenced creating Quasi-Fermi energy levels (E_{Fn} and E_{Fp}) described by the distributions in Equation 2.4 and Equation 2.5. It is easy to see from these two equations that at equilibrium $E_F = E_{Fn} = E_{Fp}$.

$$f_n(E) = \frac{1}{e^{(E-E_{Fn})/kT} + 1} \quad \text{Eqn. 2.4}$$

$$f_p(E) = \frac{1}{e^{(E-E_{Fp})/kT} + 1} \quad \text{Eqn. 2.5}$$

As I will discuss later with respect to the tunneling effect, it is also possible to degenerately dope the material in order to push the Fermi level into the valence or conduction band. However, it is important to note that a heavily doped material may exhibit unintended electrical properties depending on the distribution of the dopant. Because the distribution of the dopant may not be homogenous throughout, different energy fluctuations may be found at different positions within a strongly compensated semiconductor. This is due to the mismatch of the lattices between the two materials, which can greatly affect the conductivity of a material.

G. MOBILITY

Mobility (μ) is the ratio of average speed (drift speed) to the applied field of a material and is analogous to permittivity (ϵ_s). Ideally (in a vacuum) an electron inside of an electric field will continuously accelerate. However, in a material the electron will accelerate only until it collides with an atom in the lattice. As expected, the higher doping in a material will result in a higher probability of a collision with atoms in the lattice and therefore mobility will decrease. Figure 11 illustrates this point for some common semiconductors.

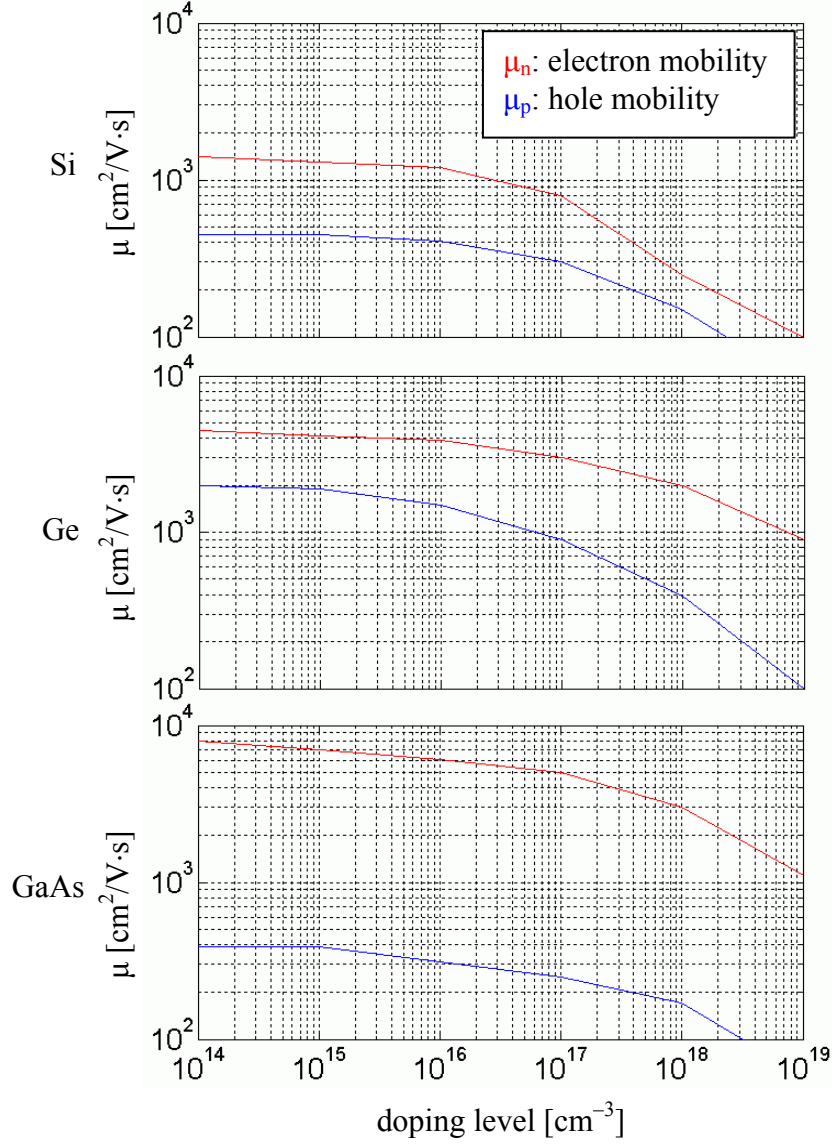


Figure 11. Mobility vs. doping level, from [7].

H. CURRENT DENSITY

The total particle current in a material is equal to the total current density (J) of both the holes (J_p) and electrons (J_n) which results from the drift and diffusion current densities. Diffusion current (I_D) is the result of electrons or holes in a concentrated area spreading themselves evenly through a material (Figure 12) in order to achieve a zero

concentration gradient ($\nabla n = 0$ for holes, $\nabla p = 0$ for electrons) throughout. Diffusion current density ($J_{p|diff}$ for holes, $J_{n|diff}$ for electrons) is analogous to the majority carrier concentration (doping) of a material and is described by Equation 2.6 and Equation 2.7 where D_p and D_n are the constants of proportionality.

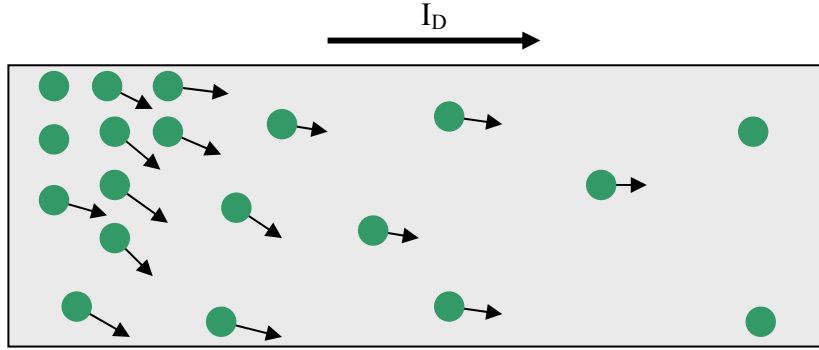


Figure 12. Diffusion current, from [2].

$$J_{p|diff} = -qD_p \nabla p \quad \text{Eqn. 2.6}$$

$$J_{n|diff} = qD_n \nabla n \quad \text{Eqn. 2.7}$$

Drift current (I_s) is the result of the introduction of an electric or magnetic field and is analogous to the minority carrier concentration and is proportional to the intensity of the field (\mathcal{E}). Figure 13 illustrates drift current in the presence of an electric field and Equation 2.8 and Equation 2.9 describe the mathematical model of drift current as a function of mobility (μ) and applied electric field.

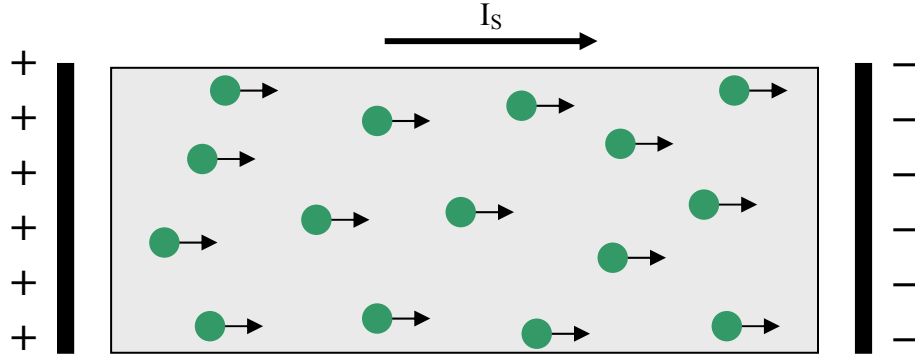


Figure 13. Drift current in the presence of an electric field, from [2].

$$J_{p|drift} = q\mu_p p \mathcal{E} \quad \text{Eqn. 2.8}$$

$$J_{N|drift} = q\mu_N n \mathcal{E} \quad \text{Eqn. 2.9}$$

Both the electron (μ_N) and hole (μ_p) current densities depend on their associated diffusion and drift currents (Eqn. 2.10 and Eqn. 2.11) which ultimately lead to the total current density (Eqn. 2.12).

$$J_p = J_{p|drift} + J_{p|diff} = q\mu_p p \mathcal{E} - qD_p \nabla p \quad \text{Eqn. 2.10}$$

$$J_N = J_{N|drift} + J_{N|diff} = q\mu_n n \mathcal{E} - qD_N \nabla n \quad \text{Eqn. 2.11}$$

$$J = J_N + J_p \quad \text{Eqn. 2.12}$$

I. GENERATION AND RECOMBINATION

Generation is the process whereby electrons and holes (carriers) are created. Conversely, recombination is the process whereby electrons and holes are annihilated. Both generation and recombination are order-restoring mechanisms to return the system to its equilibrium state ($p=n=n_i$) after the carrier excess or deficit in the semiconductor is stabilized or eliminated.

There are three important recombination-generation methods as shown in Figure 14. Band-to-band recombination (a) is the direct annihilation of a valence band hole and a conduction band electron when the hole and electron stray into the same vicinity within the semiconductor lattice. The loss of energy experienced by the electron must release an energy quantum equal to the total energy lost. This loss is typically realized in the form of light as described in Equation 2.2.

The R-G (recombination-generation) center recombination is caused by defects or special impurity atoms within the lattice and takes place only in special locations within the semiconductor known as R-G centers. The R-G center concentration is typically very low compared to the donor and acceptor concentration yet leads to the introduction of various energy levels near the center of the band gap known as the trap energy (E_T). The R-G center recombination is a two-step process and can take place in one of two ways as represented in Figure 14(b). The first method is when a carrier (hole or electron) is trapped at the impurity location until the opposite carrier is attracted to the first and recombination annihilates them both. The second is when an electron falls into the impurity location where it will initially lose energy equal to $|E_T - E_C|$. Once a hole comes into vicinity, the electron is attracted into the valence band after which it will lose the rest of its energy equal to $|E_T - E_V|$ before it recombines with the hole and disappears. This type of recombination will cause quantum lattice vibrations which will release thermal energy and ultimately increase the temperature of the semiconductor.

The third process is called Auger recombination (c), which is also a band-to-band recombination. However, this process occurs simultaneously with a collision between two like carriers. The energy transferred between the colliding carriers forces one carrier into the alternate energy band while the second carrier remains in the original band. The second carrier becomes highly energetic and then returns to its original energy level in small heat producing steps as it collides with the semiconductor lattice. This unique stepwise energy loss or “staircase” is defined as thermalization and also leads to an increased semiconductor temperature.

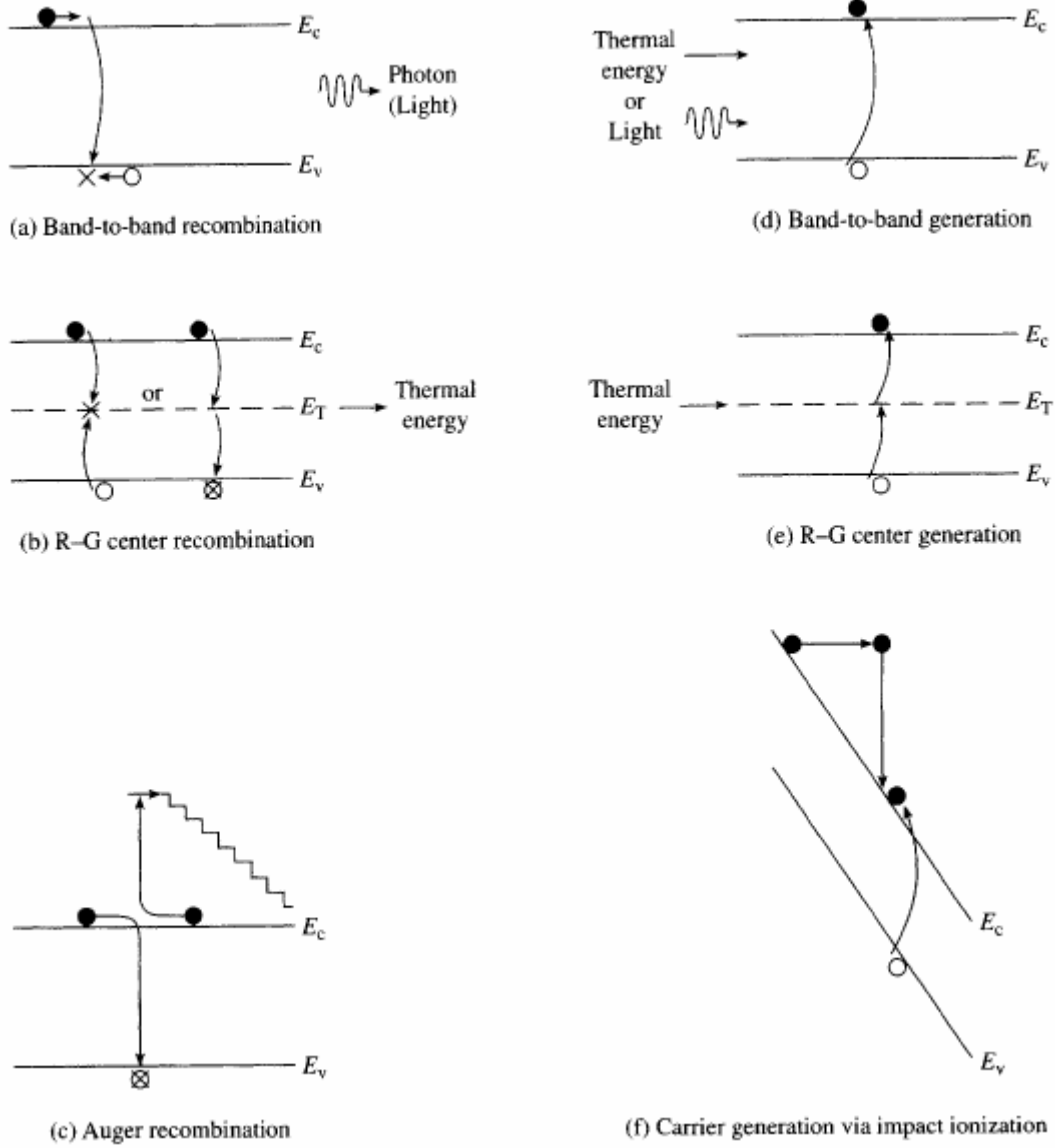


Figure 14. Energy band visualization of recombination and generation processes, from [5].

The generation process is simply the reverse of the recombination process. For band-to-band generation (d), thermal energy or light energy ($E_{ph} > E_G$) absorbed by a semiconductor will excite electrons from the valence band into the conduction band creating an EHP. Similarly, for R-G center generation (e), thermal energy absorbed by the semiconductor will excite the electron enough to achieve the trap energy at the impurity location and then again to the conduction band. Carrier generation via impact

ionization (f) is analogous to Auger recombination, because the creation of EHPs is the result of energy released when a highly energetic carrier collides with the semiconductor lattice.

J. SUMMARY

The basic understanding of semiconductor physics leads to a more advanced discussion of a p-n junction, which is discussed in the next chapter.

THIS PAGE INTENTIONALLY LEFT BLANK

III. P-N JUNCTIONS

A. INTRODUCTION TO JUNCTIONS

The successful implementation of a P-N junction is critical in modern electronics and semiconductor devices, including bipolar junction and metal on oxide transistors (BJT and MOSFET), rectifier and Zener diodes, and photovoltaics to name a few. Through the doping process, a P-N junction is formed to effectively control the electrical characteristics of a material.

B. BASIC STRUCTURE

A p-n junction is formed by a single crystal semiconductor where one side is doped with acceptors (p) and the other side is doped with donors (n). At the location of contact the metallurgical junction is formed as shown in Figure 15. Initially there is a very large majority carrier density gradient at the metallurgical junction. Equilibrium will be sought as the majority carriers in the p-type material (holes) will begin to diffuse into the n-type material while the majority carriers from the n-type material (electrons) will begin to diffuse into the p-type material.

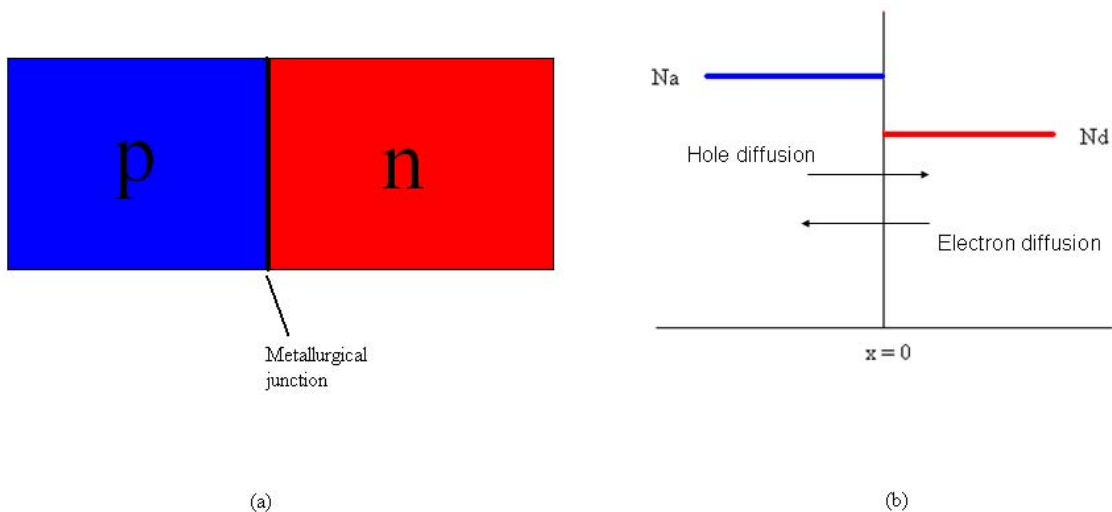


Figure 15. (a) Simplified P-N junction; (b) doping profile, from [9].

The diffusing carriers from both regions will combine with the minority carriers on the opposite side and disappear. Assuming that there is no outside electric field connected to the junction, this diffusion can not continue indefinitely. The holes diffusing from the p-region will leave behind negatively charged acceptor atoms and the electrons diffusing from the n-region will leave behind positively charged donor atoms. The net charges in the p- and n-regions will induce an electric field in the metallurgical junction, which will form what is known as a space charge region or depletion region as shown in Figure 16.

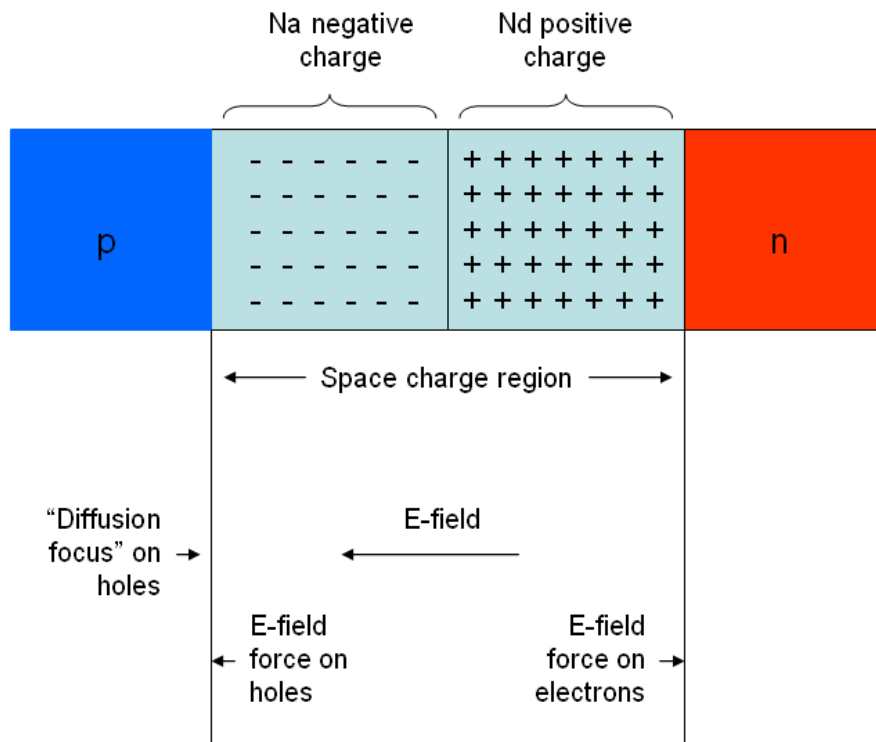


Figure 16. P-N junction depletion region formed by diffusion, from [9].

When in thermal equilibrium, the Fermi levels on both sides of the junction are equal (Figure 17). The potential barrier known as a built in voltage (V_{bi}) is responsible for maintaining equilibrium between the majority carrier electrons in the n-region and the

minority carrier electrons in the p-region. Similarly for the holes in the valence band, the built in voltage maintains equilibrium between the majority carrier holes in the p-region and the minority carrier holes in the n-region. As expected, the built in voltage depends on doping levels (N_a and N_d) within the n- and p-regions (Eqn. 3.1).

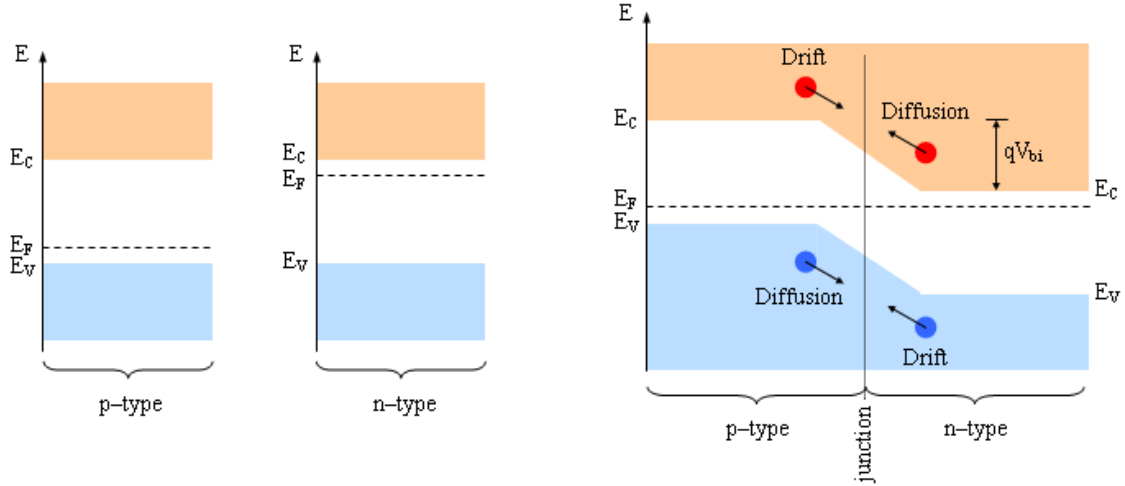


Figure 17. P-N junction energy band diagram with Fermi level.

$$V_{bi} = \frac{kT}{q} \ln \left(\frac{N_a N_d}{n_i^2} \right) \quad \text{Eqn. 3.1}$$

The width of the depletion region (W) is also related to the relative doping level of the two regions. This characteristic will become more important with the implementation of the tunnel junction (Section IV). The width of the depletion region (in cm) can be calculated by using Equation 3.2.

$$W = \left\{ \frac{2\epsilon_s V_{bi}}{e} \left[\frac{N_a + N_d}{N_a N_d} \right] \right\}^{1/2} \quad \text{Eqn. 3.2}$$

Applying different bias conditions between the two regions will disturb the p-n junction from equilibrium and the Fermi levels will no longer remain constant. For a standard doped junction, the three conditions of interest are reverse bias, forward bias and the breakdown voltage.

C. REVERSE BIAS

Applying a negative voltage (V_R) to the p-region with respect to the n-region results in a reverse bias condition as shown in Figure 18. The voltage applied attracts the majority carriers from their respective regions and leaves minority carriers in its place. This increases the voltage barrier and widens the depletion region. The difference between the two Fermi levels is equal to the bias voltage. Therefore, the total barrier voltage (V_{total}) realized by the system is the sum of the built in voltage and bias voltage (Eqn. 3.3). This barrier is easiest to visualize by the use of an energy band diagram in Figure 19.

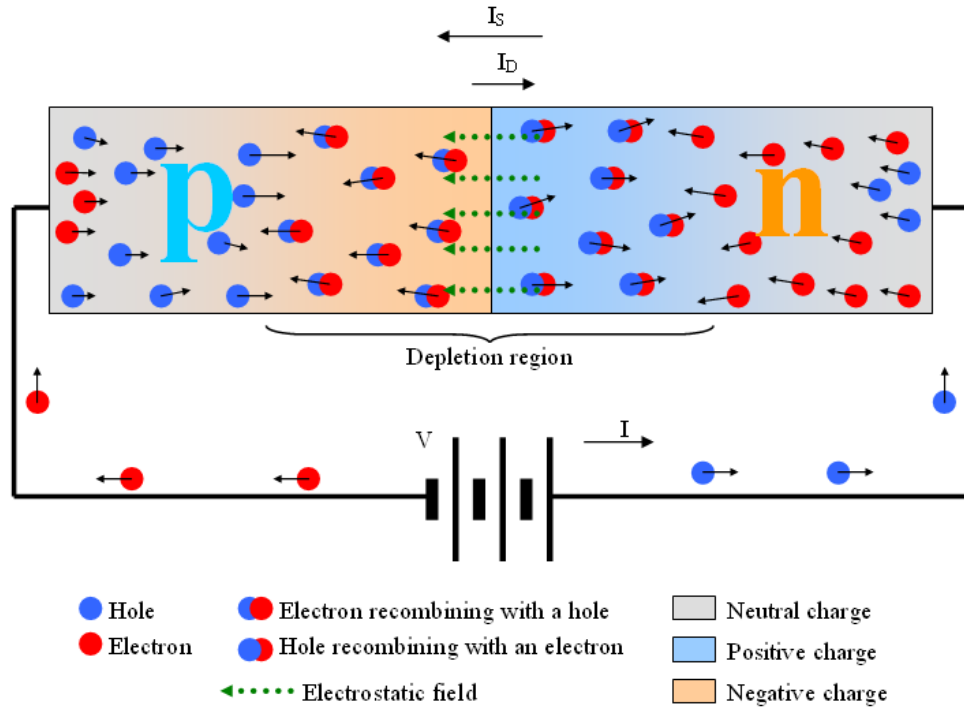


Figure 18. Reversed bias p-n junction schematic, from [2].

$$V_{total} = V_{bi} + V_R \quad \text{Eqn. 3.3}$$

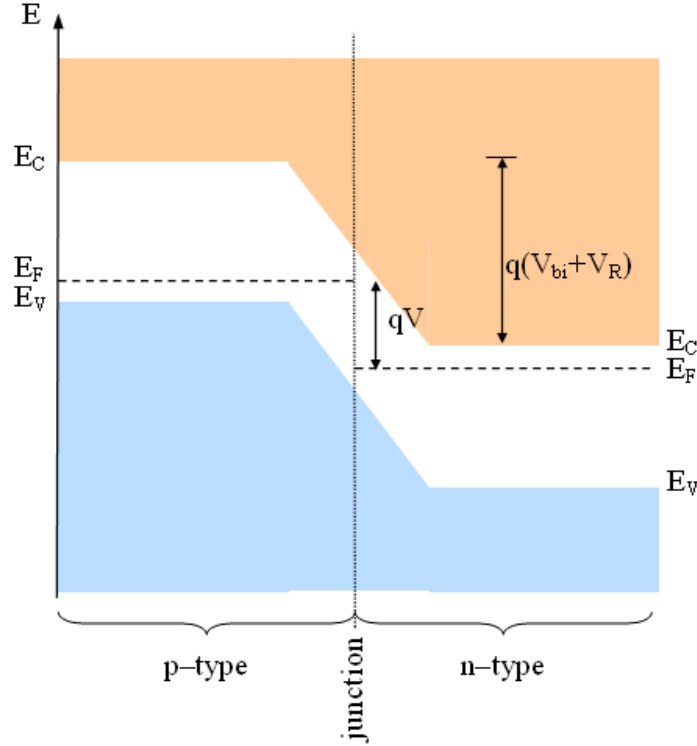


Figure 19. Reversed bias p-n junction energy band diagram.

The depletion region width is given by Equation 3.4. When in reverse bias the probability that an electron will gain enough energy to overcome the potential barrier is very small and the junction will act like an insulator, not allowing current to flow. With the increased depletion region, diffusion current (I_D) is very small and the total current in the system is approximately equal to the drift current (I_S) (Eqn. 3.5). Ideally, this current would be equal to zero, but, in reality, there is a small amount of drift current in the system, as illustrated in Figure 20.

$$W = \left\{ \frac{2\epsilon_s (V_{bi} + V_R)}{e} \left[\frac{N_a + N_d}{N_a N_d} \right] \right\}^{1/2} \quad \text{Eqn. 3.4}$$

$$I_{total} = I_S + I_D \approx I_S \quad (\text{very small}) \quad \text{Eqn. 3.5}$$

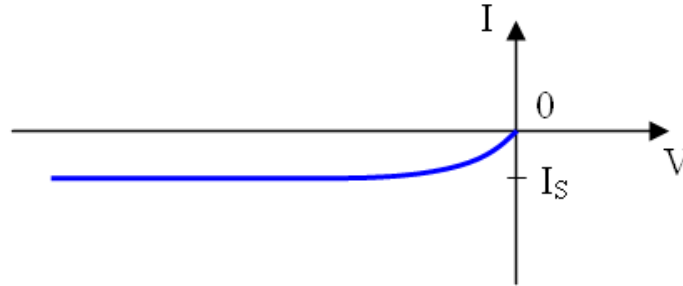


Figure 20. Reversed bias p-n junction I-V characteristic.

D. FORWARD BIAS

Applying a positive voltage (V_a) to the p-region with respect to the n-region is considered forward bias (Figure 21). The forward bias opposes the built in field developed in the depletion region and the region becomes narrower. When the junction is forward bias, the Fermi level in the p-region is increased and the Fermi level in the n-region is decreased to a point where electrons can overcome the small potential barrier (Eqn. 3.6), as illustrated by Figure 22.

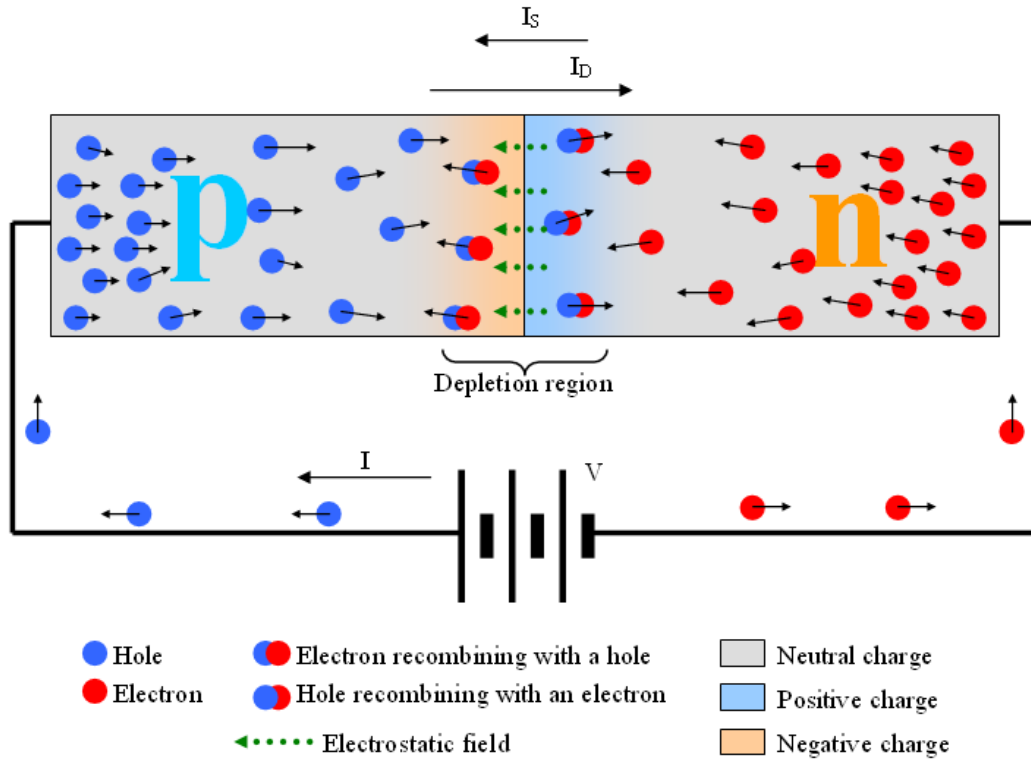


Figure 21. Forward bias p-n junction schematic, from [2].

$$(V_{bi} - V_a) \quad \text{Eqn. 3.6}$$

$$I_{total} = I_s + I_D \approx I_D \quad \text{Eqn. 3.7}$$

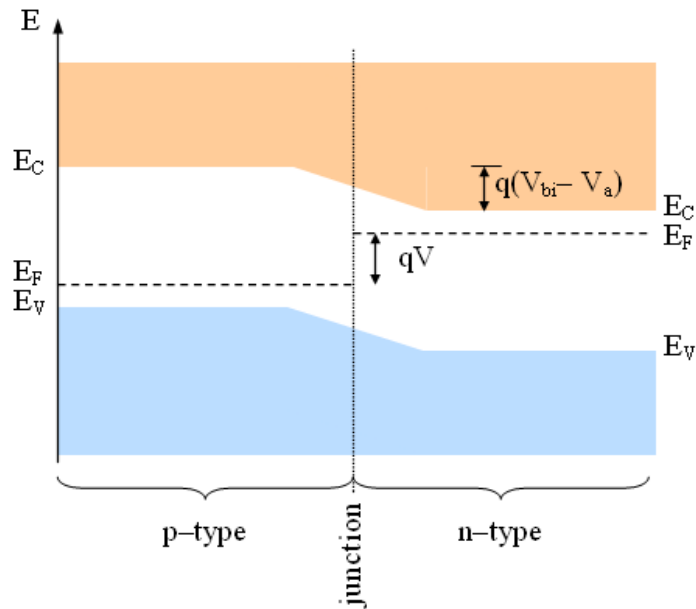


Figure 22. Forward bias p-n junction energy band diagram.

As the continuously supplied majority carriers from the n-region transition into the p-region, they become minority carriers where they diffuse and eventually combine with the majority holes. Similarly, the continuously generated holes in the p-region will be available to combine with the electrons traversing the potential barrier. Just as before, some of the current being produced is due to drift (I_S) and some is due to diffusion (I_D). However, in the forward bias condition the diffusion current is much greater than the drift current (Eqn. 3.7) due to the decreased depletion region. Figure 23 shows the I-V characteristic of a p-n junction in the forward bias condition. Notice that the current does not begin to flow until sufficient voltage is applied to overcome the potential barrier. This happens at approximately 0.7V for Si and 0.1V for Ge.

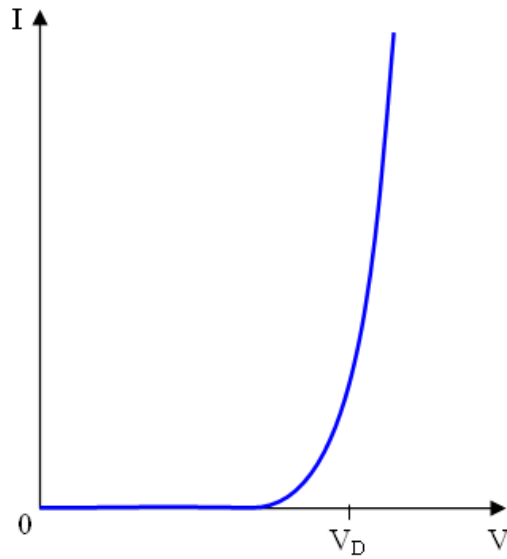


Figure 23. Forward bias p-n junction I-V characteristic.

E. BREAKDOWN/ZENER TUNNELING

Adding reverse bias beyond a certain threshold voltage will result in the breakdown of the p-n junction. This breakdown phenomenon is due to either a Zener effect or an avalanche effect.

The Zener or tunneling effect is similar to the tunneling which I will discuss at length in the next section. The difference here is that the Zener effect takes place when a minority carrier in the p-region valence band is able to penetrate through the energy barrier to an empty state in the n-region conduction band unaffected. This can only occur once the valence band of the p-region increases beyond the conduction band of the n-region due to the reverse bias. The exchange of minority carriers creates a large change in reverse current with a small change in reverse bias. Zener diodes are designed to achieve this result (Figure 24).

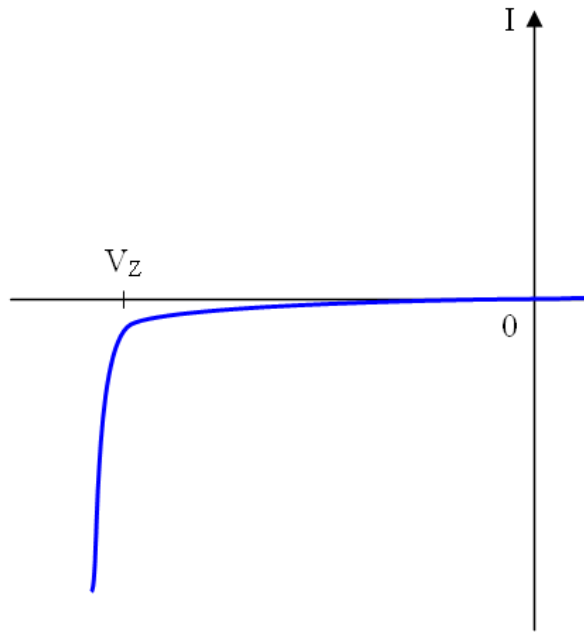


Figure 24. Zener breakdown p-n junction I-V characteristic.

The avalanche effect is also a minority carrier effect in which an electron from the p-region with a very large kinetic energy collides with atoms and breaks the covalent bonds. Often the EHPs created collide with other atoms to create even more EHPs, creating an avalanche-type effect. As more and more minority carriers are created, they are swept to the opposite region which creates a large reverse current. This runaway effect often leads to excess heat from the lattice vibrations and results in a damaged p-n junction.

F. LOSSES

Ideally there would be no losses in the system and the slope of the I-V curve would be perpendicular to the x-axis when on. However, since the semiconductor material has an inherent ohmic resistance due to atomic masses and impurities, there is a slight ohmic loss in the junction. Putting three regions together, a typical p-n junction I-V curve is realized (Figure 25).

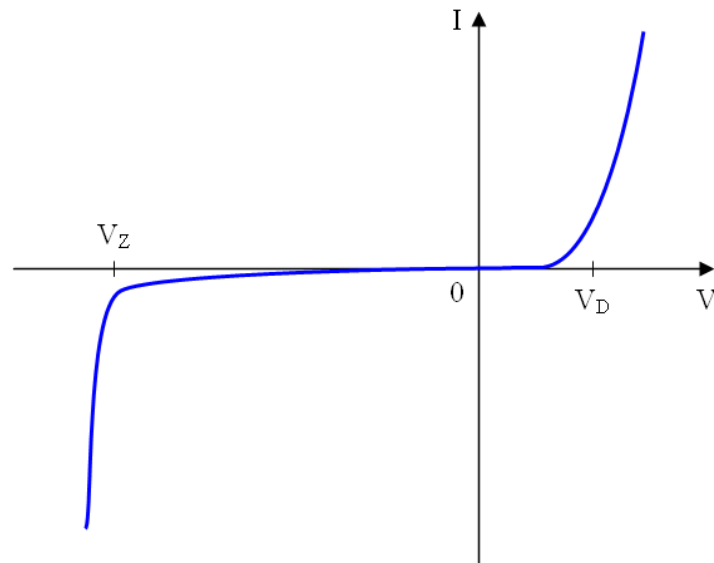


Figure 25. p-n junction I-V characteristic.

G. SUMMARY

Controlling the doping levels in the respective regions will shift the Fermi levels and affect the ability of an electron or hole to move through the lattice. Increasing the doping levels to a point where the Fermi levels are within the energy bands of the n- and p- regions is essential to tunneling phenomenon and will be discussed in the following Chapter.

THIS PAGE INTENTIONALLY LEFT BLANK

IV. TUNNEL JUNCTION

A. TUNNELING THEORY

The tunneling phenomenon is a majority carrier effect in which both the n- and p-regions are degenerately doped (very heavily doped with impurities) allowing an electron to tunnel through a potential barrier that, under normal conditions, would not be possible to penetrate. The tunneling is based on a quantum transition probability (T_t) per unit time and is proportional to the exponent of the average value of momentum ($\bar{k}(0)$) within the tunneling path across the depletion region (Eqn. 4.1). This momentum corresponds to an incident carrier with a transverse momentum of zero and energy equal to the Fermi energy. The tunneling probability equation will be further explained later in this section.

$$T_t = \exp \left[-2 \int_{-x_1}^{x_2} |\bar{k}(x)| dx \right] \quad \text{Eqn. 4.1}$$

B. PURPOSE

To achieve a higher power density, multiple cells with different I-V curves and decreasing bandgaps are placed in tandem as illustrated in Figure 26. As a result the incident light will be absorbed by the top cell allowing the unabsorbed photons to pass through to the sub cells. This results in the sum of the voltage produced by the individual cells.

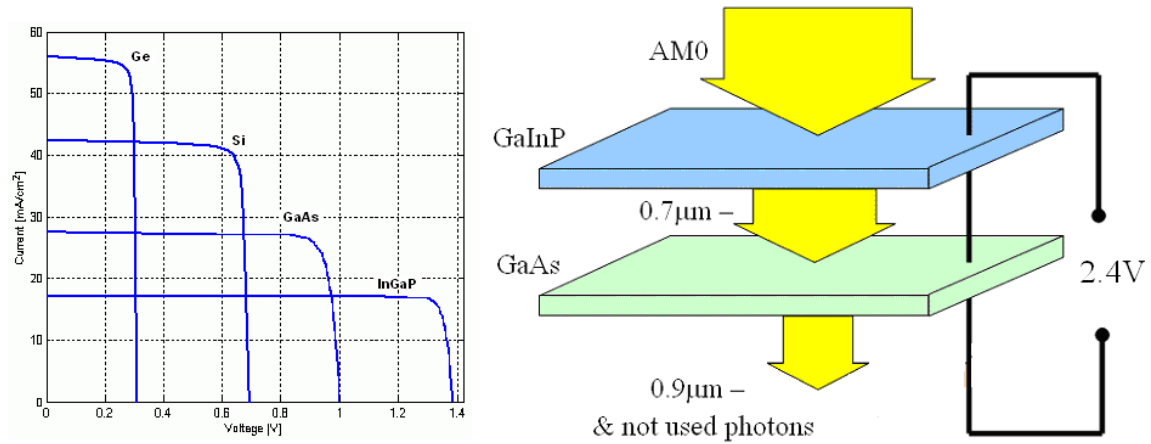


Figure 26. Tandem solar cells.

Unfortunately, stacking the cells in tandem would result in a parasitic junction formed by the two dissimilar regions of the different cells (Figure 27) and must be separated in order to allow current flow.

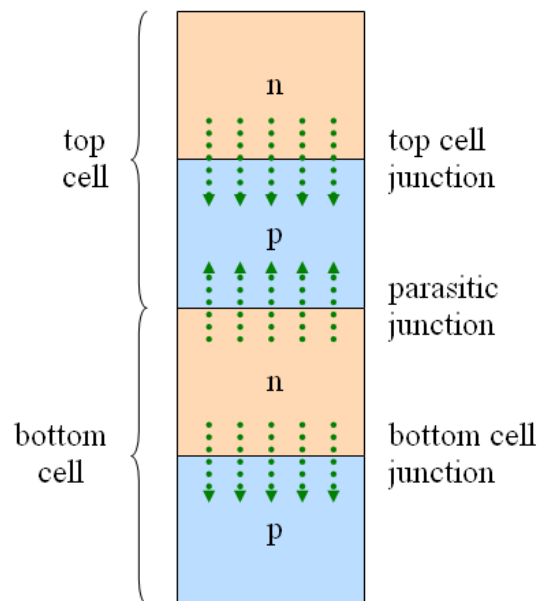


Figure 27. Tandem solar cell with parasitic junction.

One option is to mechanically stack the cells using an oxide/conductor contact as shown in Figure 28. However, the added contact material shadows the sub cells from the unused photons being passed through the top cell, limiting any efficiency gained by placing the cells in tandem.

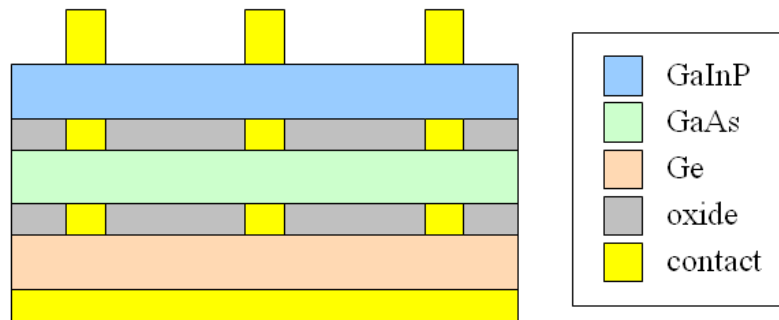


Figure 28. Tandem solar cell example with oxide/conductor contact separation, from [2].

Another solution to this issue is to use a tunnel junction to separate the individual cells in the tandem cell. The tunnel junction will allow photons to pass through as well as pass current with minimal voltage loss (Figure 29).

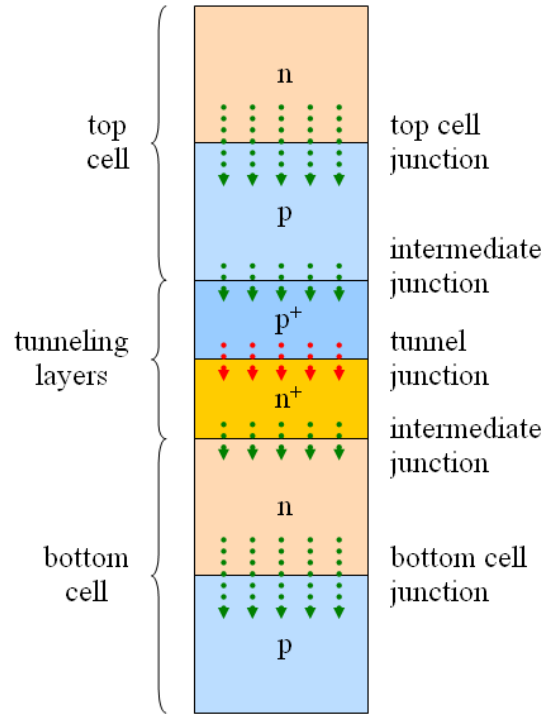


Figure 29. Tandem cell with tunnel junction.

C. THE JUNCTION

A tunnel junction is simply a tunnel diode or degenerately doped p-n junction commonly used in switching and oscillator circuit applications. The difference between the tunnel junction and the tunnel diode is that the tunnel junction is grown as a single crystal joining two solar cells, whereas a tunnel diode operates as a discrete component within a circuit. The purpose of mentioning the tunnel diode is for completeness, as tunnel diodes have been studied and used in electronics since their invention by Leo Esaki in 1958, who received the Nobel Prize in Physics in 1973 for his work. From this point on, there will be no distinction made between the two and I will focus on the tunnel junction and its application to photovoltaics.

A tunnel junction is formed with degenerately doped regions in order to push the respective Fermi levels into the valence and conduction bands (Figure 30). As a result, the p-region valence band will contain holes and the n-region conduction band will

contain electrons at thermal equilibrium. The depletion region width is also affected by the degenerately doped regions compressing it to $<100\text{\AA}$, which is essential to the tunneling effect and is significantly smaller than a conventional p-n junction.

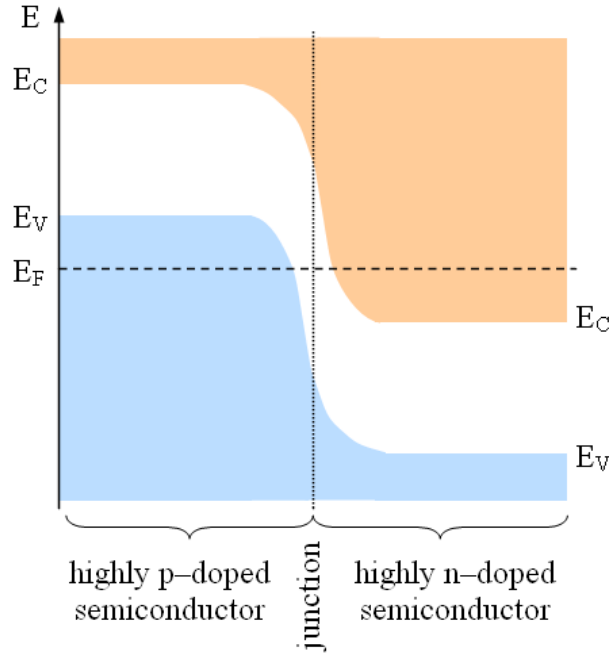


Figure 30. Degenerately doped tunnel junction energy band diagram.

In order for quantum tunneling to occur, four criteria must be met. The necessary conditions for tunneling are: (1) occupied energy states exist on the side from which the electron will tunnel; (2) unoccupied energy states exist at the same energy levels as those electrons in the occupied energy states; (3) the tunneling barrier width is small and the potential barrier height is low enough that there is a finite tunneling probability; and (4) the momentum is conserved in the tunneling process [2].

D. THERMAL EQUILIBRIUM

As in the conventionally doped p-n junction, the two Fermi levels of the p- and n- regions are equal at thermal equilibrium. Figure 31 illustrates the tunneling junction energy bands at thermal equilibrium as well as the corresponding I-V plot. The red dot

on the I-V plot corresponds to the location of interest on the curve. Since both regions are doped to the point where the Fermi levels exist inside the valence and conduction band and are therefore considered degenerately doped.

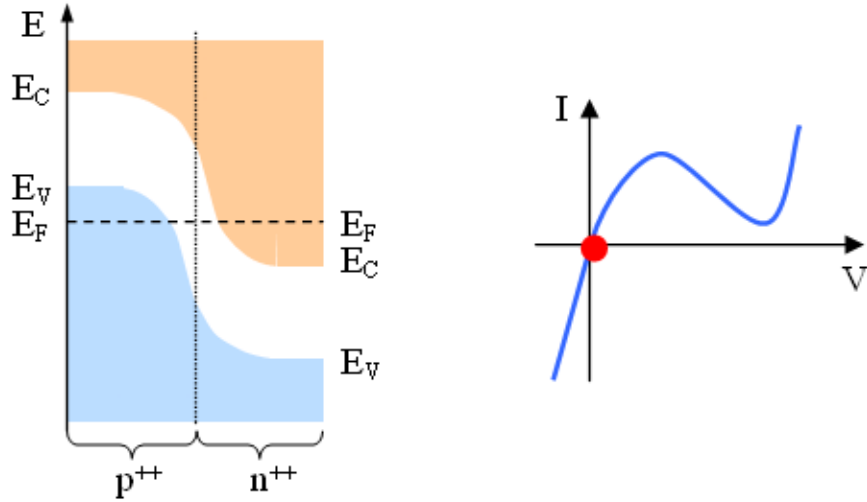


Figure 31. Tunnel junction energy band and I-V characteristic at thermal equilibrium, from [7].

E. REVERSE BIAS

Similar to the Zener effect discussed in the last section, in reverse bias the minority carrier in the p-region valence band is able to tunnel through the potential barrier to the conduction band of the n-region. Unlike the Zener effect in a standard p-n junction, the reverse bias tunneling in this junction occurs as soon as a reverse bias is applied to the junction. The reason for the immediate response is the degenerate doping of the regions. Since the Fermi levels are inside the respective valence and conduction bands at equilibrium, there are empty states available for the minority carrier to fill as soon as reverse bias is applied. Therefore, a large reverse current is realized for a small change in voltage. Figure 32 illustrates the minority carrier electron tunneling to the conduction band of the n-region as well as the location on the I-V curve where reverse bias tunneling takes place.

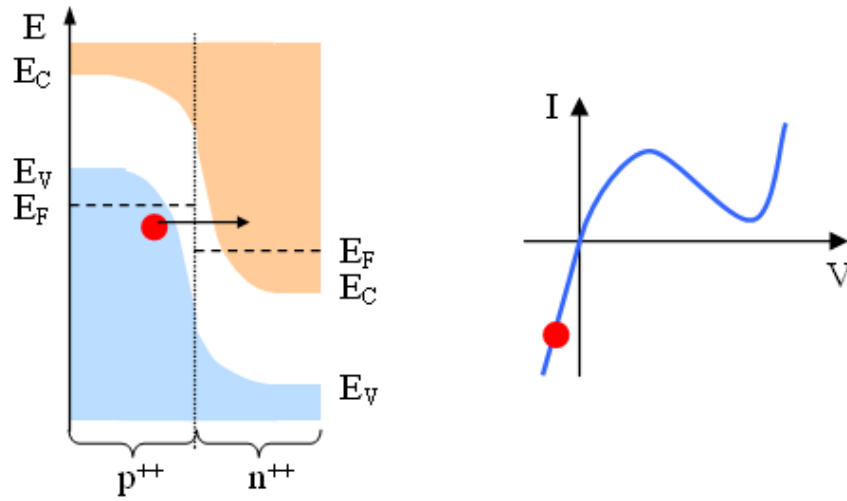


Figure 32. Tunnel junction energy band and I-V characteristic in forward bias (reverse bias), from [7].

F. FORWARD BIAS

At forward bias (Figure 33), the tunnel junction has available energy states in the p-region corresponding to filled energy states in the n-region. As the voltage is increased from zero to V_p , the valence band energy of the p-region and the conduction band energy of the n-region become closer in value.

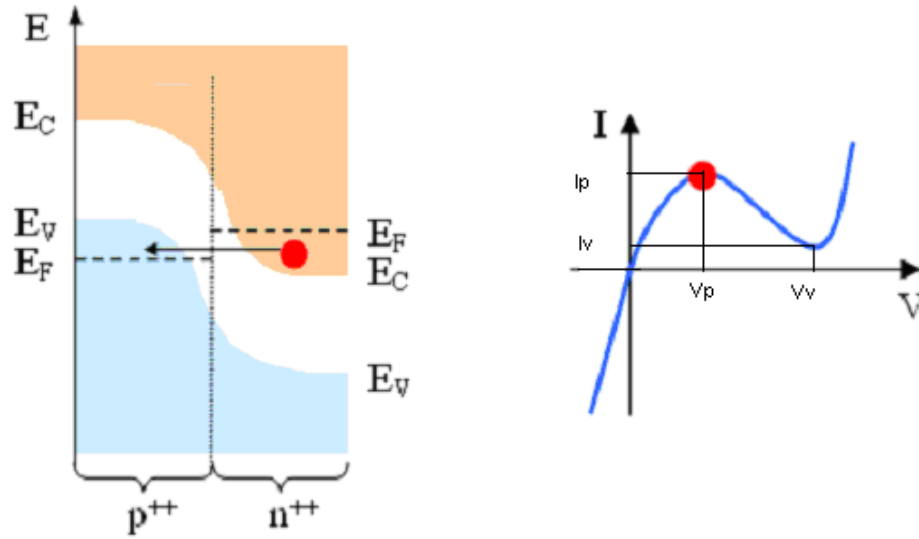


Figure 33. Tunnel junction energy band and I-V characteristic in forward bias (peak tunneling), from [7].

G. NEGATIVE RESISTANCE

From V_p to V_v , tunneling is still occurring but fewer and fewer empty states are available. With a small increase in forward bias ($>V_p$), the number of electrons in the n-region directly opposite the empty states in the p-region continues to decrease which will result in a decreased tunneling current. The region from V_p to V_v is described as negative resistance (Figure 34) and will continue until the valence band of the p-region is equal to the conduction band of the n-region at which time the tunneling current will be zero.

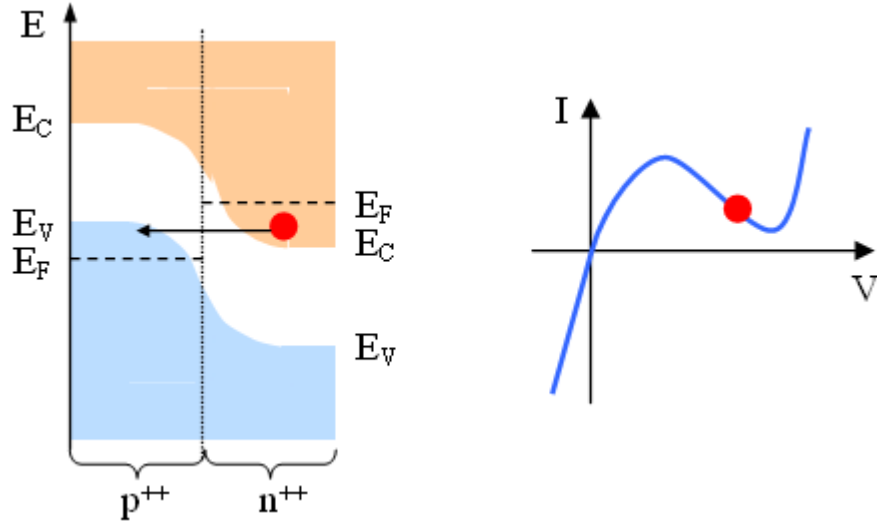


Figure 34. Tunnel junction energy band and I-V characteristic in forward bias (negative resistance), from [7].

H. THERMAL CURRENT FLOW

Increasing the forward bias even further beyond V_v will eventually result in the normal current flow of a p-n junction. As illustrated in Figure 35, the energy band diagrams of the p- and n-regions are reminiscent of the standard p-n junction with an applied forward bias. The relationship between a standard p-n junction and a degenerately doped tunnel junction can be further understood by comparing the two curves in Figure 36. As additional forward bias is applied, the current flow of the standard p-n junction and that of the tunnel junction merge.

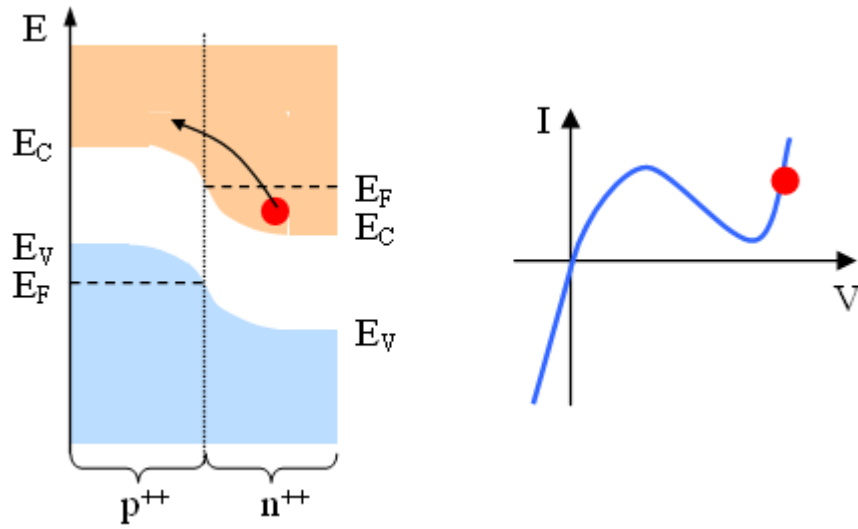


Figure 35. Tunnel junction energy band and I-V characteristic in forward bias (thermal current flow), from [7].

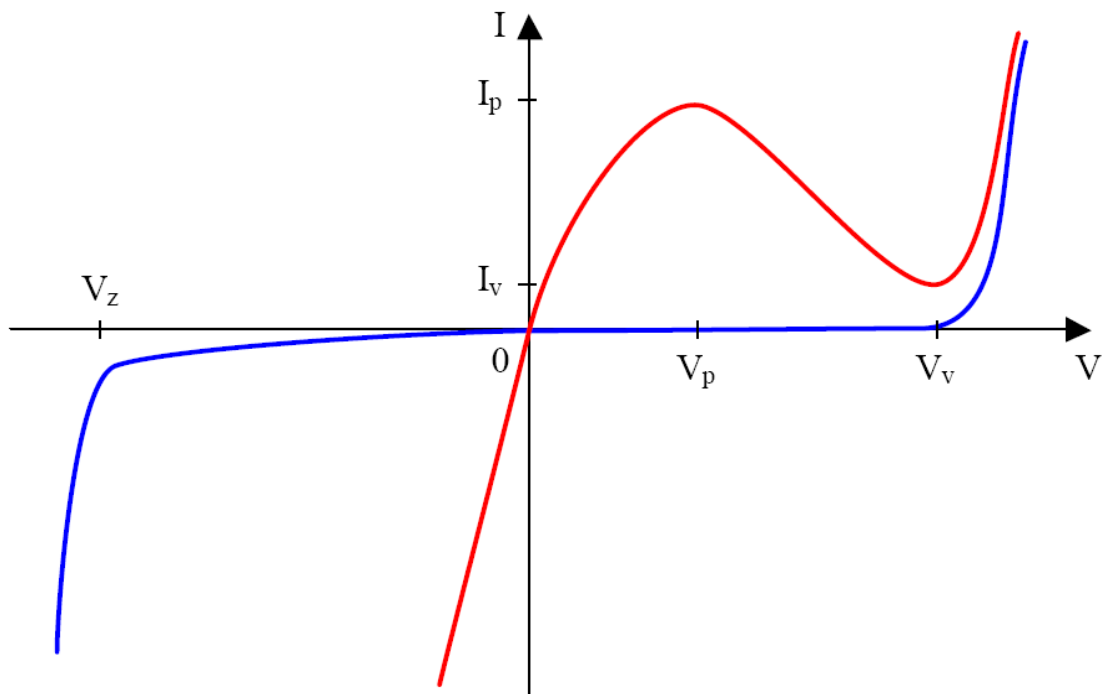


Figure 36. Characteristic I-V curve of a tunnel (red) and conventional (blue) p-n junction.

I. DIRECT AND INDIRECT TUNNELING

Just as there is a direct and indirect materials relationship, so too is there a direct and indirect tunneling process. Superimposing the E-k relationship at the classical turning points onto the E-x relationship of the tunnel junction reveals the direct and indirect tunneling differences. In Figure 37 (a) and (b) the electrons in the vicinity of the minimum of the conduction band energy-momentum can tunnel to a corresponding value of momentum in the vicinity of the valence band. However, the distinction lies in the electron and hole momentum.

For direct band tunneling to occur, the momentum for the valence band maximum and the conduction band minimum must be the same. This type of tunneling is illustrated in Figure 37 (a) and takes place in direct bandgap semiconductors such as GaAs and InP as well as indirect bandgap semiconductors where the voltage applied to the junction is large enough that the valence band maximum (Γ point) is in line with the conduction band minimum (Γ point) [7].

Conversely, indirect band tunneling occurs when the conduction band minimum and the valence band maximum do not occur at the same momentum, as shown in Figure 37 (b). As a result, momentum is conserved by scattering agents such as photons or impurities and is deemed photon assisted tunneling. Due to the complex nature of photon assisted tunneling, it is far less likely to take place when direct tunneling is possible. However, it is possible for both direct and indirect tunneling to occur at the same time.

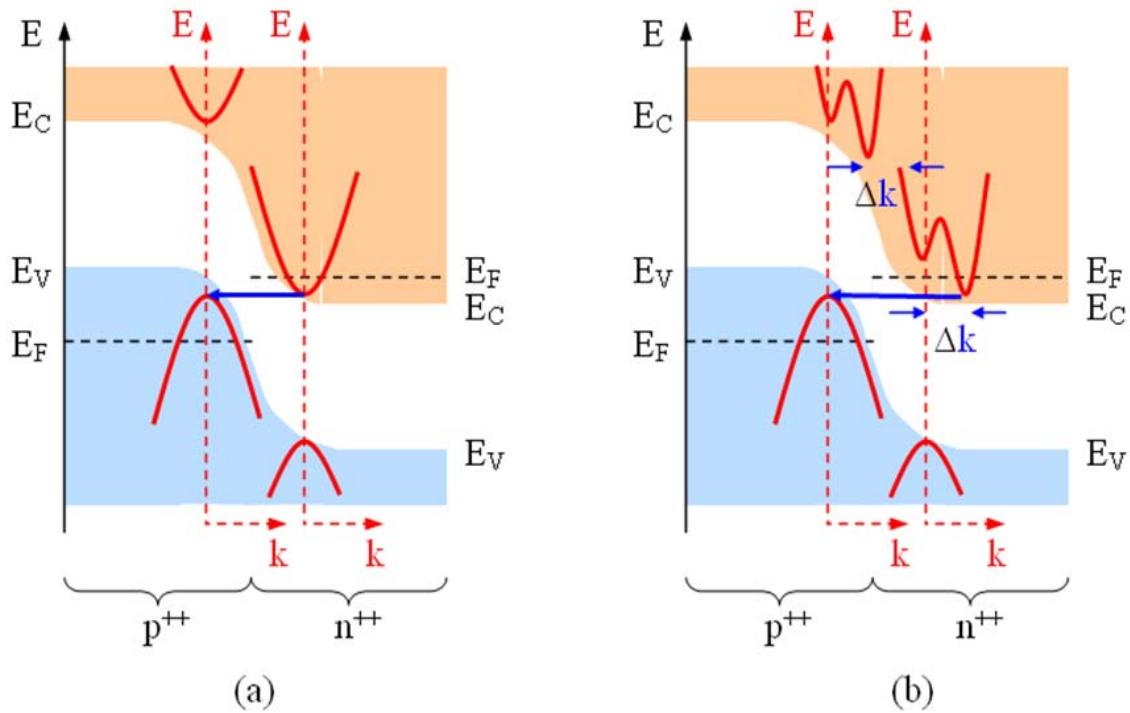


Figure 37. (a) Direct band tunneling process. (b) Indirect band tunneling process, from [7]

J. TUNNELING CURRENT

For quantum tunneling to exist, the electric field in the depletion region must be on the order of 10^6 V/cm. When this is achieved, there is a finite probability that an electron will be excited from the valence band directly to the conduction band of the semiconductor.

Local band-to-band tunneling models in Silvaco's ATLAS[®] account for the electric field at each node to calculate the generation rate due to tunneling. However, in reality the tunneling is non-local and it is therefore necessary to take the spatial profile of the energy bands into account as well as the spatial separation of the electrons generated in the conduction band from the holes generated in the valence band [9]. To achieve this, ATLAS[®] creates a series of 1-D slices through the device to calculate the tunneling

current. The slices are generated as an additional mesh through a series of *qty* and *qtx* statements, which are then placed over the top of the original mesh. We will discuss the mesh statements in detail in Section V.

With sufficiently high doping of both the p- and n-region of the junction, any electron within the appropriate energy range has a finite probability of tunneling from the valence band to the conduction band. ATLAS[®] considers each energy level within this range and calculates the spatial start ($-x_1$) and end (x_2) point at that level. The tunneling current can then be calculated as a function of the tunneling probability ($T(E)$), the effective mass (m^*), and the potential barrier height (E_g) as described by Equation 4.2, where k is Boltzmann's constant, q the electric charge, T is temperature, \hbar is the reduced planks constant and E is the electron energy.

$$J(E) = \frac{qkTm^*}{2\pi^2\hbar^3} T(E) \ln \left\{ \frac{1 + \exp[E_{Fl} - E]/kT}{1 + \exp[E_{Fr} - E]/kT} \right\} \Delta E \quad \text{Eqn. 4.2}$$

ATLAS[®] provides the tools to implement a number of probability equations for both local and non-local tunneling but none proved better at achieving the forward bias than the Wentzel-Kramers-Brillouin method (WKB).

K. WENTZEL-KRAMERS-BRILLOUIN METHOD (WKB)

The tunneling probability is given by the WKB method (Eqn. 4.3) in which the wave vector ($k(x)$) of a carrier is evaluated as an exponential function and integrated over the depletion region from $-x_1$ to the x_2 .

$$T_t \approx \exp \left[-2 \int_{-x_1}^{x_2} |k(x)| dx \right] \quad \text{Eqn. 4.3}$$

Although there are many ways to implement this equation based on the geometry of the potential barrier, the method I will use is based on a triangular geometry (Figure 38) because this is the method used by the ATLAS[®] modeling software.

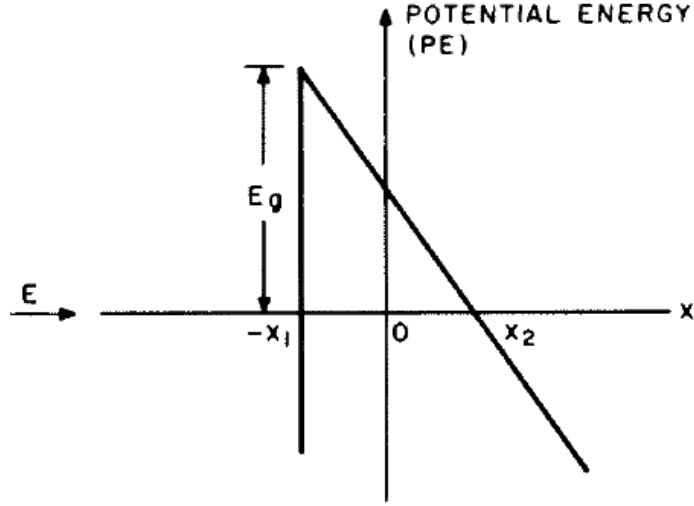


Figure 38. Triangular potential barrier for tunneling model, from [7]

For the triangular potential barrier in Figure 38 the wave vector is given as [7]:

$$k(x) = \sqrt{\frac{2m^*}{\hbar} (PE - E)} = \sqrt{\frac{2m^*}{\hbar} \left(\frac{E_g}{2} - q\mathcal{E}x \right)} \quad \text{Eqn. 4.4}$$

Where PE is the potential energy, E is the incoming electron energy, E_g is the energy bandgap, and \mathcal{E} is the electric field.

Substituting Equation 4.4 into Equation 4.3 yields [7]:

$$\begin{aligned}
T_t &\approx \exp \left[-2 \int_{-x_1}^{x_2} \left| \sqrt{\frac{2m^*}{\hbar} \left(\frac{E_g}{2} - q\mathcal{E}x \right)} \right| dx \right] \\
&= \exp \left[+ \frac{4}{3} \frac{\sqrt{2m^*}}{q\mathcal{E}\hbar} \left(\frac{E_g}{2} - q\mathcal{E}x \right)^{3/2} \right]_{-x_1}^{x_2}
\end{aligned}
\tag{Eqn. 4.5}$$

Since at $x = -x_1$, $\left(\frac{E_g}{2} - q\mathcal{E}x \right) = E_g$

And at $x = x_2$, $\left(\frac{E_g}{2} - q\mathcal{E}x \right) = 0$

The quantum tunneling probability can be simplified to:

$$T_t \approx \exp \left[- \frac{4}{3} \frac{E_g^{3/2} \sqrt{2m^*}}{q\mathcal{E}\hbar} \right]
\tag{Eqn. 4.6}$$

Where E_g is the bandgap of the material, m^* is the effective mass defined in Equation 4.7, q is the electric charge, \mathcal{E} is the electric field, and \hbar is the reduced Plank's constant.

$$m^* = m_0 \sqrt{m_e(x_2) m_h(x_1)}
\tag{Eqn. 4.7}$$

L. SUMMARY

The tunneling phenomenon presented is based on the probability that an electron is able to penetrate a potential barrier if there are occupied and unoccupied states at the same energy level on both sides of the potential barrier, the distance between the beginning and end of the potential barrier is sufficiently small, and momentum of the tunneling electron is conserved. The following Chapter will implement the given equations into the Silvaco software.

V. SIMULATION SOFTWARE

A. SILVACO

Silicon Valley Company (Silvaco) is a leading vendor in technology computer aided design (TCAD). Established in 1984 and located in Santa Clara, California, Silvaco has developed a number of exceptional CAD simulation tools to aid in semiconductor process and device simulation. Silvaco has an extensive support team to assist with the broad array of semiconductor technologies.

B. ATLAS[®]/DECKBUILD

The ability to accurately simulate a semiconductor device is critical to industry and research environments. The ATLAS[®] device simulator is specifically designed for 2D and 3D modeling to include electrical, optical and thermal properties within a semiconductor device. ATLAS[®] provides an integrated physics-based platform to analyze DC, AC and time-domain responses for all semiconductor-based technologies. The powerful input syntax allows the user to design any semiconductor device using both standard and user-defined material of any size and dimension. ATLAS[®] also offers a number of useful device examples to assist in your own unique design.

DeckBuild is the run time environment used to input a command file or deck and is given the extension “.in”. To run ATLAS[®] in the DeckBuild environment, the user must first call the ATLAS simulator with the command:

```
go atlas
```

There is other simulation software available that can be used in conjunction with DeckBuild, such as ATHENA and DevEdit (Figure 39), but ATLAS[®] is the most appropriate environment for this research.

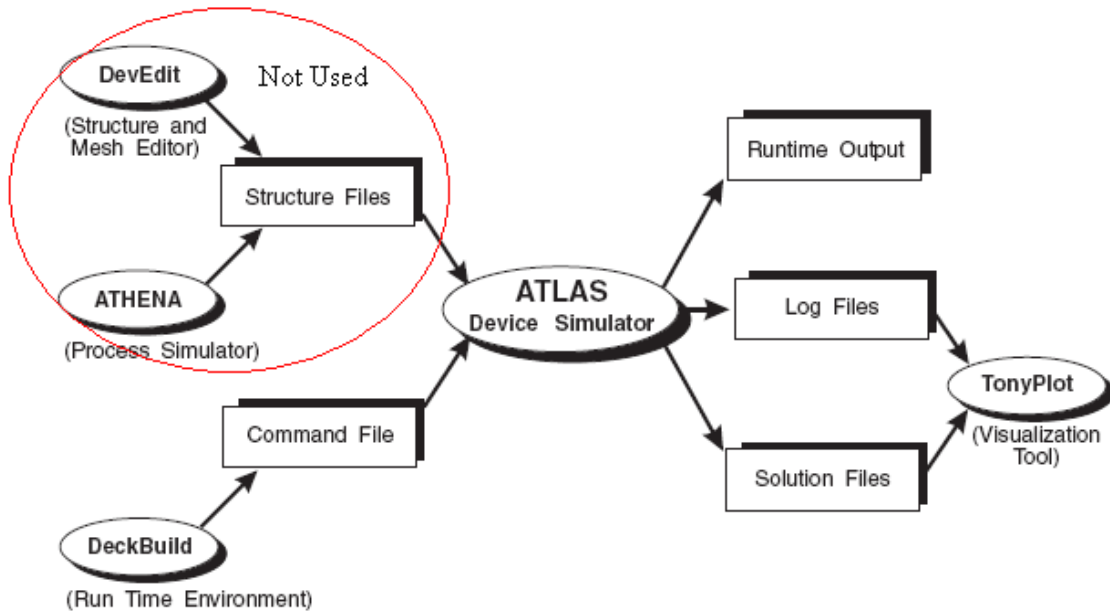


Figure 39. Silvaco Inc.'s simulation environment, from [10].

C. SYNTAX

Once ATLAS[®] is called there is a syntax structure that must be followed in order for ATLAS[®] to execute the command file successfully. Figure 40 is a list of primary group and statement structure specifications. Although there are a few input exceptions, the input file statements follow the general format of:

<STATEMENT> <PARAMETER>=<VALUE>

<i>Group</i>		<i>Statements</i>
1. Structure Specification	————	MESH REGION ELECTRODE DOPING
2. Material Models Specification	————	MATERIAL MODELS CONTACT INTERFACE
3. Numerical Method Selection	————	METHOD
4. Solution Specification	————	LOG SOLVE LOAD SAVE
5. Results Analysis	————	EXTRACT TONYPLOT

Figure 40. ATLAS[®] command groups with the primary statements in each group, from [11].

D. STRUCTURE SPECIFICATION

1. Mesh

The mesh statement is used to define the structure in an inverted 2D or 3D Cartesian grid. The x-axis is positive from left to right, the y-axis is negative from bottom to top and the z-axis is positive from the plane of the x-y axis into the workspace. The reason for the inverted y-axis is that the manufacturing coordinates are usually described as depth below the surface. All coordinates are entered in microns and the spacing is used to refine the sharpness and accuracy at an assigned location. ATLAS[®] produces a series of triangles to form the mesh based on the user input parameters. Figure 41 shows the mesh of a tunnel junction along with the parameters entered in ATLAS[®].

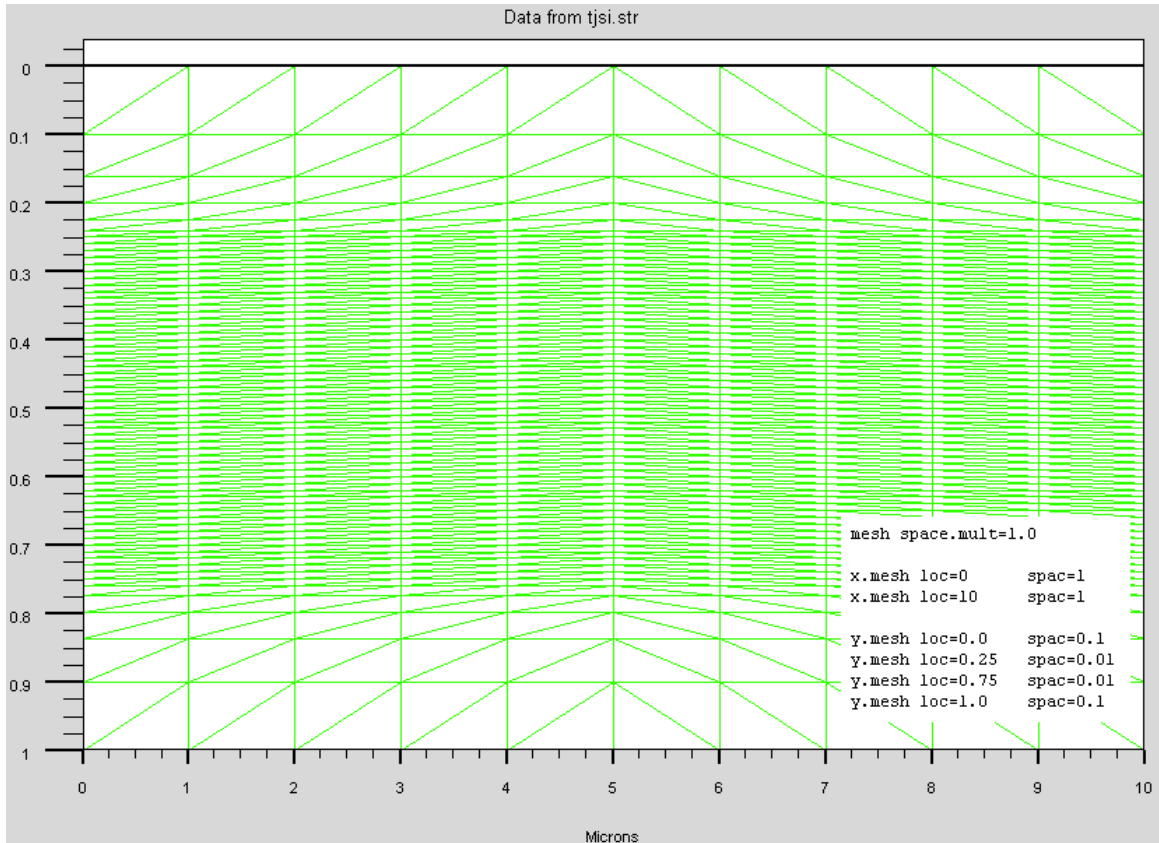


Figure 41. Tunnel junction mesh.

This particular tunnel junction is only $1\mu\text{m}$ thick and $10\mu\text{m}$ wide. The depth (z-direction) has a default value of $1\mu\text{m}$ but was defined as 1×10^7 to produce an output equal to one square centimeter, which corresponds to published data. Building this semiconductor as a $1\text{cm} \times 1\text{cm}$ square would only add nodes to the structure and ultimately increase the calculation time. The implementation of the junction to a solar cell required a smaller node set which I achieved by limiting the x-y dimensions to 10cm^2 .

The accuracy of any calculated value in ATLAS[®] is dependent on the refinement of the mesh at the junction of interest. The x.mesh is much larger than the y.mesh because the variables being measured/calculated are across the junction, which was defined horizontally.

2. Region

The region statement is used to separate the initial mesh statement into distinct blocks and sets the initial material parameters that can be referred to later by region number. All meshed areas of a structure must be assigned a region and the regions must be ordered from lowest to highest region. For instance, region 5 cannot be defined before region 4. The tunnel junction is described by the DeckBuild commands along with the region lines in Figure 42.

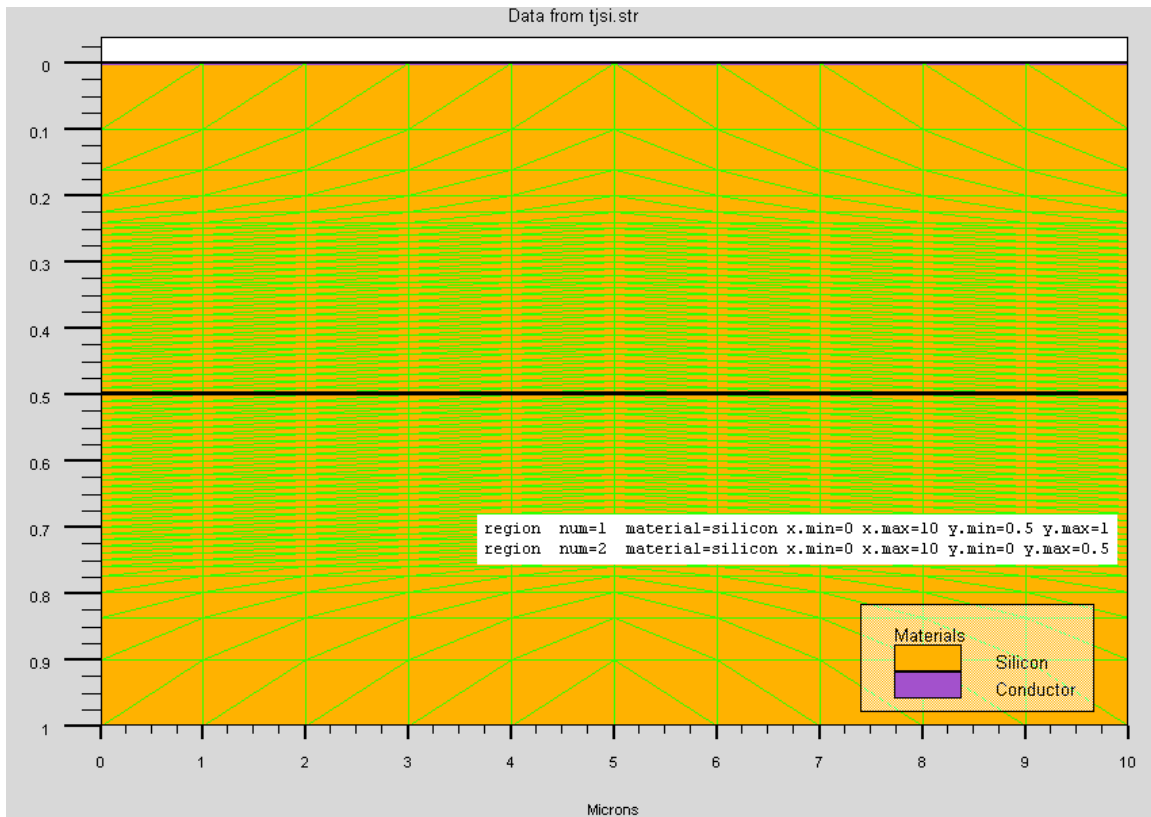


Figure 42. Tunnel junction region.

3. Electrode

Once the regions are set, the electrodes must be assigned to the desired region so that it can be electrically analyzed. The electrode can be assigned to any region or portion of a region including the “top” or “bottom” as it is in this research. Because this tunnel junction is intended to be used as an interconnect between two solar cells, it was

unnecessary to assign the electrodes to metal contacts or large areas that would constitute superfluous calculations or error. Therefore, the anode was assigned to the top of the junction and cathode was assigned to the bottom. The following statements were used to define these parameters:

```
#electrodes
electrode name=anode top
electrode name=cathode bottom
```

4. Doping

The last required input of the structure specification is the doping statement. The doping statement is used to assign the doping level within the previously assigned regions. Various properties can be appended to the doping statement to specify how the semiconductor was doped and of whether the region is n- or p-type. The desired I-V relationship in forward bias will determine the doping characteristics of the semiconductor. However, the following statements were developed for a Si junction with a forward bias current of approximately 12A at 0.06V:

```
doping uniform p.type conc=5e19 y.max=0.5
doping uniform n.type conc=1e20 y.min=0.5
```

Here the regions were already defined in a previous statement and were therefore referred to by their region number. Region 1 was uniformly doped with a p-type material with a concentration of 5e19. Similarly, region 2 was uniformly doped with an n-type material at a concentration of 1e20.

With the doping statement complete, the structure specifications are complete and it is possible to continue with the simulation following the guidelines in Figure 40. Unlike the structure specifications, the remaining four groups to be specified do not require all statements to run without error.

E. QUANTUM TUNNELING MESH

In order to calculate the quantum tunneling through a potential barrier, finer slices of the junction must be taken. ATLAS[®] does this with the definition of the qtx.mesh and qty.mesh statements. The direction of tunneling must also be specified with a different parameter in the models statement. Figure 43 illustrates the extremely refined qty.mesh along with the input parameters to achieve this level of precision. Although the qtx.mesh was defined, the slices are only extremely refined in the y-direction because this is the direction of tunneling. The new rectangular mesh is superimposed over the original triangular mesh and both mesh statements will be evaluated and accounted for in the tunneling current. As with all ATLAS[®] spacing parameters, the qty.mesh spacing is specified as μm .

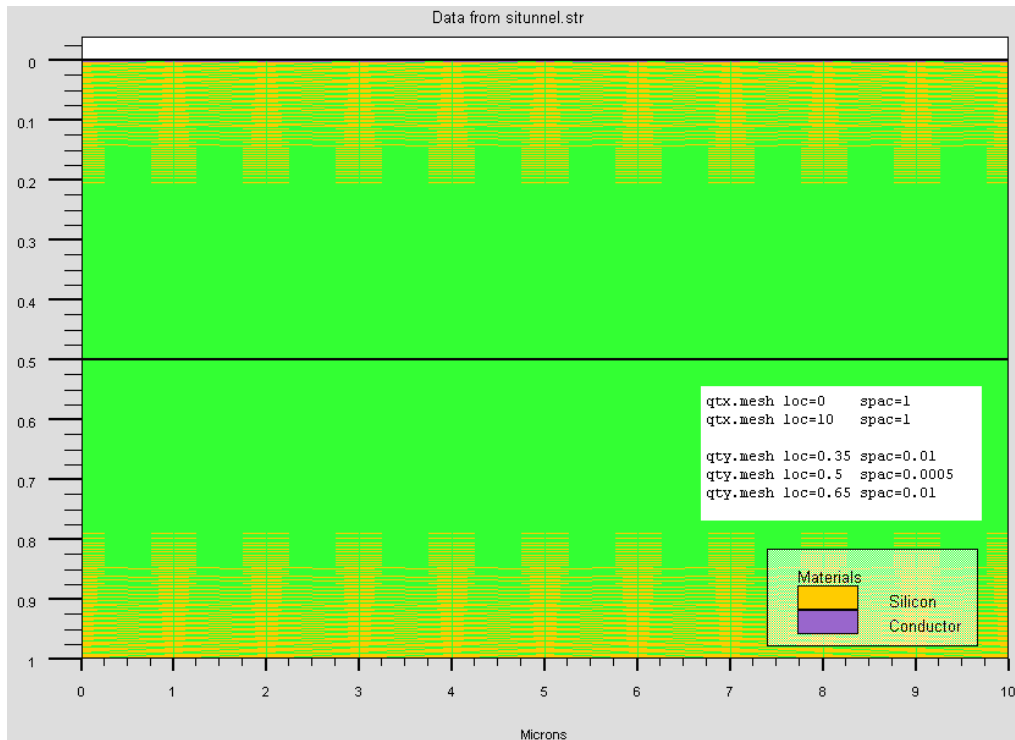


Figure 43. Tunnel junction qtx.mesh and qty.mesh.

F. MATERIAL MODELS SPECIFICATION

1. Material

The material statement relates physical parameters with the materials assigned to the mesh. The important material parameters for most standard semiconductors are already defined by ATLAS[®] and therefore do not require any changes. We utilized the extensive model libraries in ATLAS[®] since the developed tunnel junctions were based in Si, Ge, and GaAs which are all very well researched and documented.

2. Models

The models statement is essential to the accurate modeling of a particular phenomenon because it sets flags for ATLAS[®] to indicate the inclusion of different mathematical models, physical mechanisms and other global parameters such as substrate temperature. The model statement and parameters used in this research are listed below:

```
models temperature=300 srh fermi ni.fermi print qtunn.dir=0 \  
bbt.nonlocal bbt.forward bbt.nlderivs
```

As with all ATLAS[®] statements, a complete list of modeling parameters and their definitions can be found in the ATLAS[®] User's Manual [11]. The most notable parameters for the calculation of the quantum tunneling effect are qtunn.dir, bbt.nonlocal, bbt.forward and bbt.nlderivs. qtunn.dir specifies the direction of tunneling across the junction. Since this device was set up for tunneling across the y-axis, the parameter value was set to zero (to specify tunneling in x-direction, qtunn.dir = 1). The bbt.nonlocal, bbt.forward and bbt.nlderivs parameters enable the non-local band-to-band tunneling model to be used in forward bias and allows the use of the non-local derivatives in the Jacobian matrix which helps eliminate convergence problems.

3. Contact

Since the tunnel junction is meant to be used as an interconnect of a single crystal multi-junction solar cell there was no need to specify any contact parameters. The

electrode statements assigning the cathode and anode to the semiconductor were sufficient for calculating the current through the junction.

G. NUMERICAL METHOD SELECTION

The method statement specifies the numerical methods to be used in the calculations specified in the model statement. The quantum tunneling through a junction is highly dependent on the carrier concentration. Therefore, it is very important to accurately measure the carrier concentration for each iteration. This is done by defining the climit parameter in the method statement, which specifies the normalization factor to limit the step size of the potential update. The parameter dvmax sets the maximum allowed potential updates per iteration. Reducing dvmax dampens the oscillations in the small I-V calculations.

H. SOLUTION SPECIFICATION

The log/solve/save statements are used to create data files in ATLAS[®] simulations. These statements work together to provide data to be analyzed by other functions. This research I have used these three statements as a tool to check bias points, energy band diagrams and carrier concentrations as a result of varying stimuli.

1. Log

The log statement allows all terminal characteristics generated by a solve statement to be saved to a file.

2. Solve

The solve statement specifies which bias points are to be applied to produce an output. The bias points can be set in a number of different way including step, initial and lambda depending on what stimulus is desired.

3. Save

The save statement is used to save all node point data into an output file. A common use of the log/solve/save statements for the tunnel junction studied is shown below:

```
log outfile=tjsi.log
solve name=anode vanode =-1 vstep=0.1 vfinal=0.0
solve name=anode vanode =0.0 vstep=0.01 vfinal=0.2
solve name=anode vanode =0.2 vstep=0.1 vfinal=1.5
save outfile=tjsi.log
```

Here the output file tjsi.log has been set aside to store data from the solve statements and then saved so that the data can be called at a later time. The solve statements simply sweep the voltage from -1V to 1.5V in varying voltage steps depending on the degree of accuracy at the desired range. With the data stored in an outfile, it is ready to be displayed so that it can be analyzed.

I. RESULTS ANALYSIS

The tonyplot statement is used to start the graphical post-processor tool. Calling tonyplot to visualize tjsi.log displays the output file in Figure 44. The complete tunnel junction input deck can be found in Appendix A.

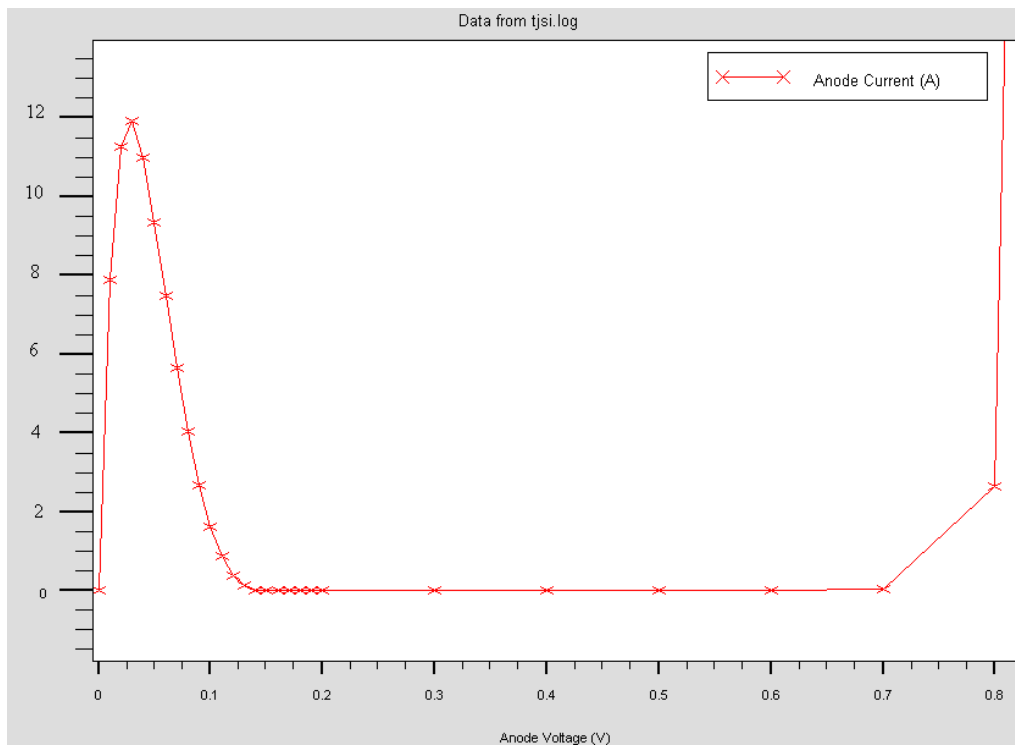


Figure 44. Silicon tunnel junction I-V curve in ATLAS[®].

THIS PAGE INTENTIONALLY LEFT BLANK

VI. TUNNEL JUNCTION RESULTS

After the successful modeling of the basic forward bias tunneling current in Si, it was necessary to test the validity of the model. This was accomplished by measuring the response of different materials and doping levels to similar bias conditions.

A. SEMICONDUCTOR MATERIAL

As an interconnect between two dissimilar solar cells it is important that a tunnel junction can be modeled for materials other than Si. Typical tunnel junctions used today are GaAs and InGaP due to their close lattice matching. The ATLAS[®] input deck presented here was developed so that cell parameters are easily changed and the tonyplot outputs are easy to compare.

The doping levels' initial calculations were based on the Fermi-Dirac equations presented in Section II. Figures 45 and 46 illustrate the tunnel junction energy band diagrams along with their associated I-V curves for GaAs and InGaP respectively.

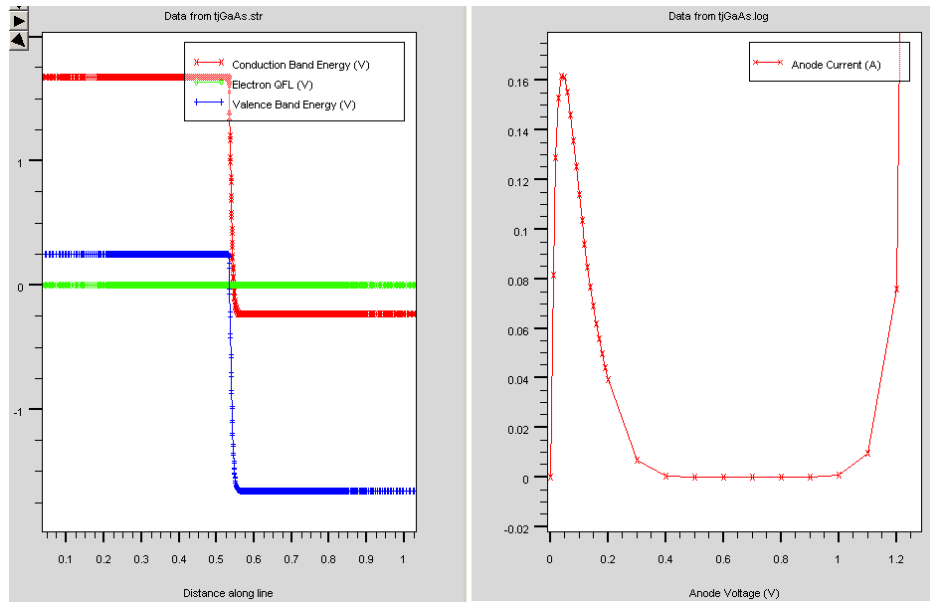


Figure 45. GaAs tunnel junction ($p = 3e20/cm^3$ $n = 9e18/cm^3$) (A/cm^2 versus volts in a $1\mu m$ thick junction).

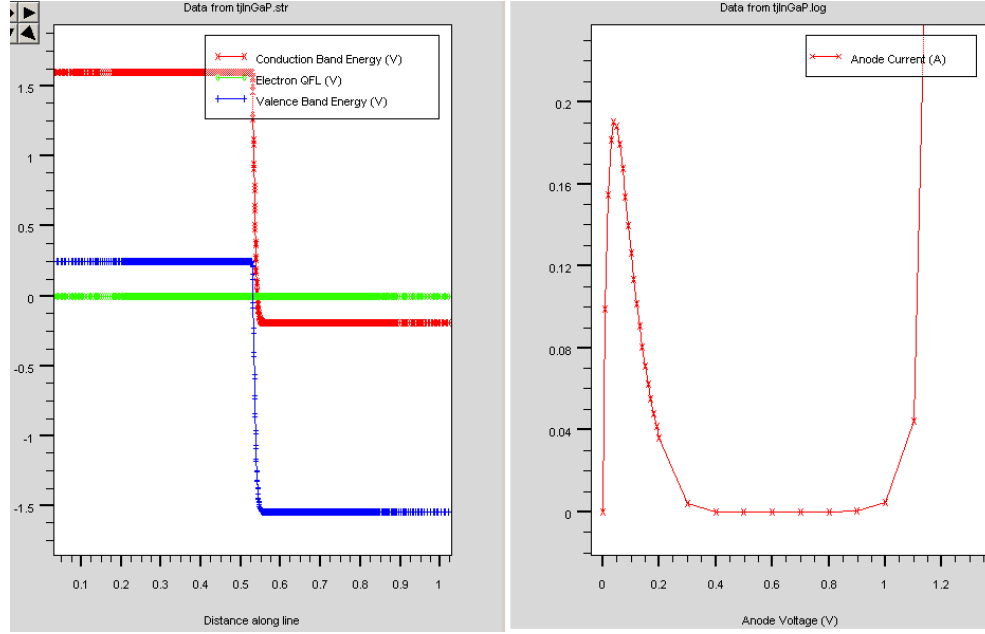


Figure 46. InGaP tunnel junction ($p = 2e20/cm^3$ $n = 9e18/cm^3$) (A/cm^2 versus volts in a $1\mu m$ thick junction).

By fine-tuning the doping levels, an output current of approximately 200mA was realized for both junctions. Though this current is slightly high for a typical current produced by a solar cell, we simply solved for 200mA as a baseline. With the successful modeling of the two junctions, we were able to manipulate the doping levels and analyze the different outputs.

B. TUNNEL JUNCTION DOPING

The doping levels of the tunnel junctions were changed for both the n- and p-regions to shift the Fermi level and ultimately vary the response to the given bias condition. Figures 47 through 52 illustrate the reaction to increased doping of the GaAs junction. Figures 53 through 58 show similar results for an InGaP junction.

Initially, the p-region was varied from a doping level within $3kT$ ($\sim 0.077eV$) of the valence band, then increased by a reasonable factor (between 2 and 3) to show the response in the I-V curve. Pushing the Fermi level further into the valence band

corresponds to an increased number of available holes that can recombine with electrons tunneling through the junction and therefore increases the current.

The n-region was varied in a similar manner. However, pushing the Fermi level further into the conduction band increases the number of electrons available to tunnel through the junction and similarly increases the current.

1. GaAs Tunnel Junction

a. p-region variation:

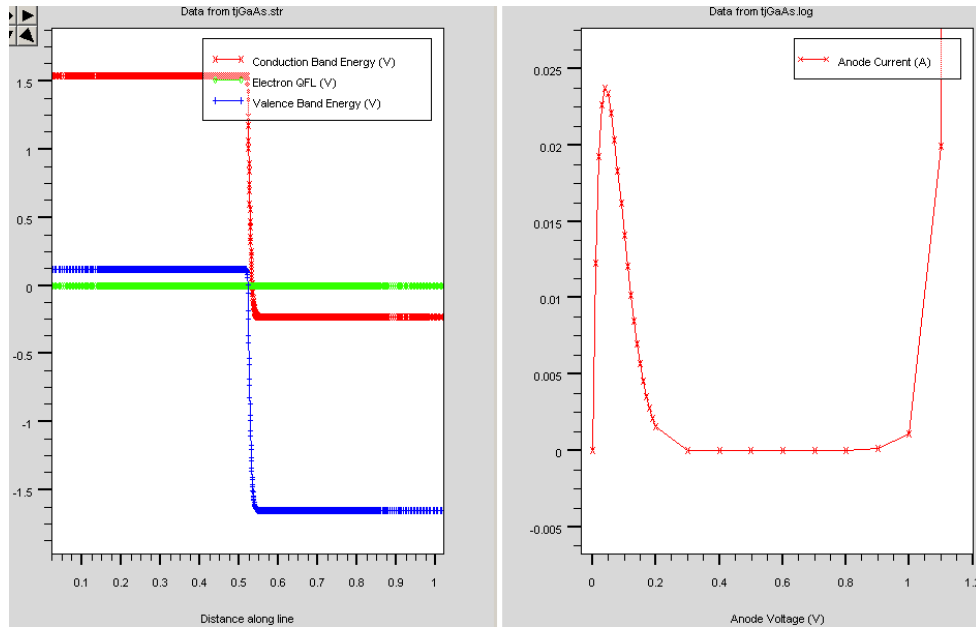


Figure 47. GaAs IV characteristics and energy band diagram ($p = 1e20/cm^3$ $n = 9e18/cm^3$) (A/cm^2 versus volts in a $1\mu m$ thick junction).

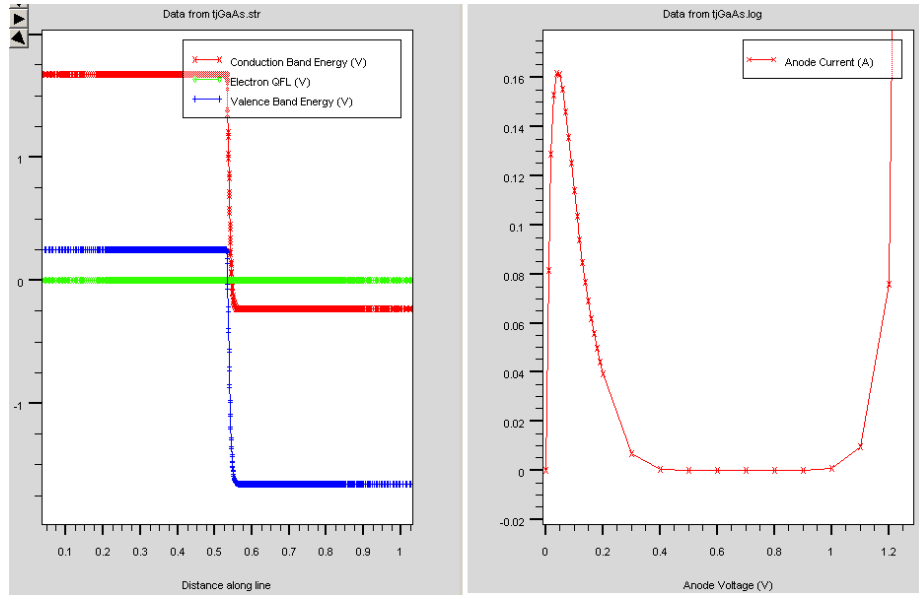


Figure 48. GaAs IV characteristics and energy band diagram ($p = 3e20/cm^3$ $n = 9e18/cm^3$) (A/cm^2 versus volts in a $1\mu m$ thick junction).

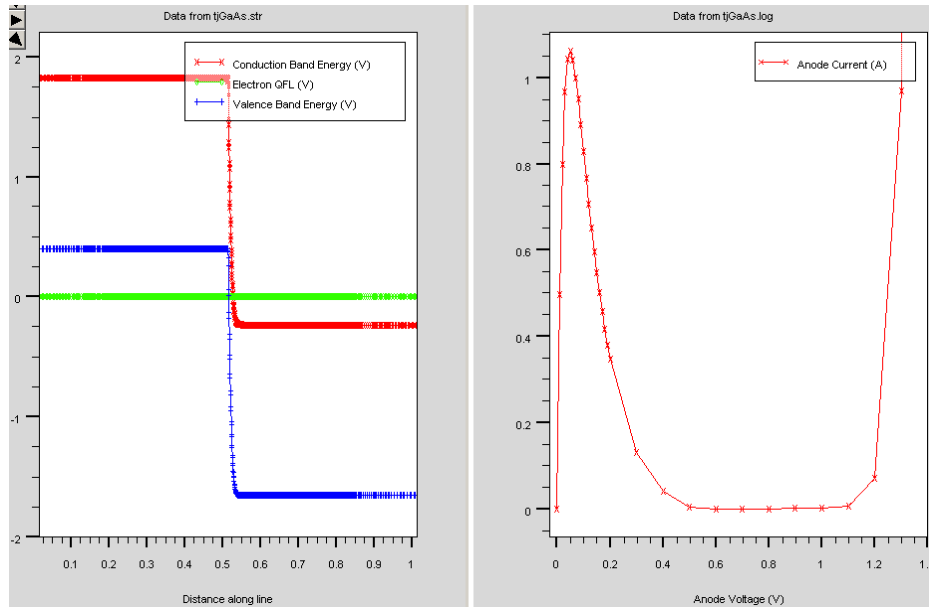


Figure 49. GaAs IV characteristics and energy band diagram ($p = 6e20/cm^3$ $n = 9e18/cm^3$) (A/cm^2 versus volts in a $1\mu m$ thick junction).

b. n-region variation:

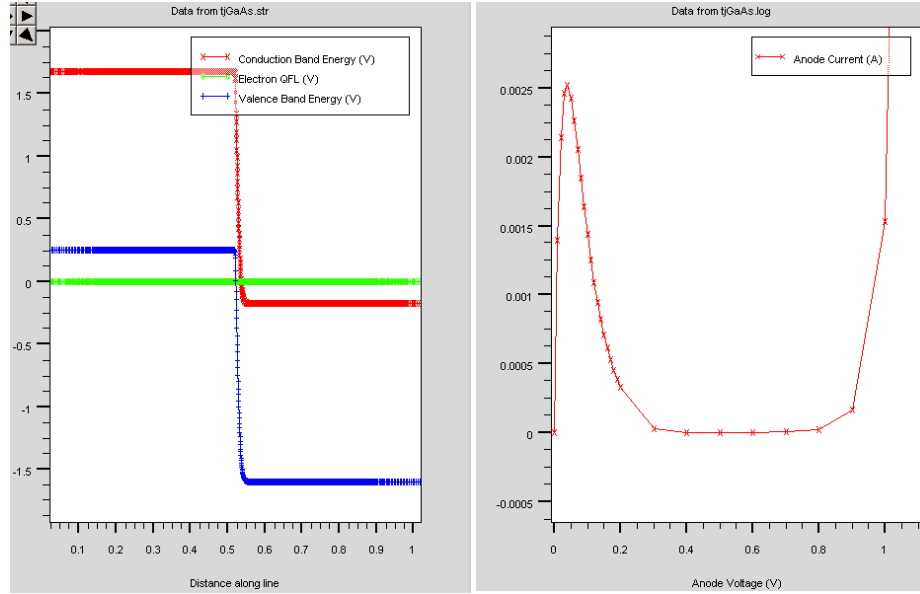


Figure 50. GaAs IV characteristics and energy band diagram ($p = 3 \times 10^{20} \text{ cm}^{-3}$ $n = 6 \times 10^{18} \text{ cm}^{-3}$) (A/cm^2 versus volts in a $1 \mu\text{m}$ thick junction).

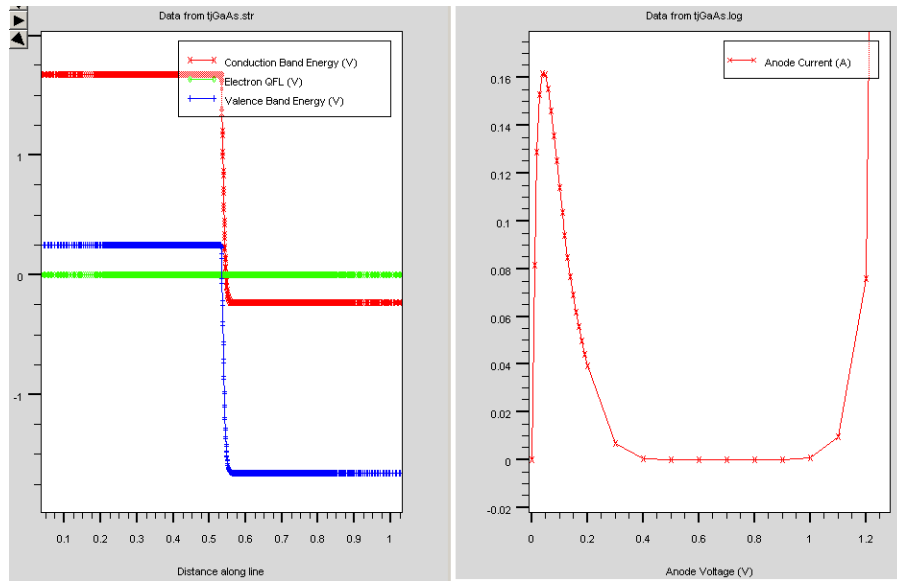


Figure 51. GaAs IV characteristics and energy band diagram ($p = 3 \times 10^{20} \text{ cm}^{-3}$ $n = 9 \times 10^{18} \text{ cm}^{-3}$) (A/cm^2 versus volts in a $1 \mu\text{m}$ thick junction).

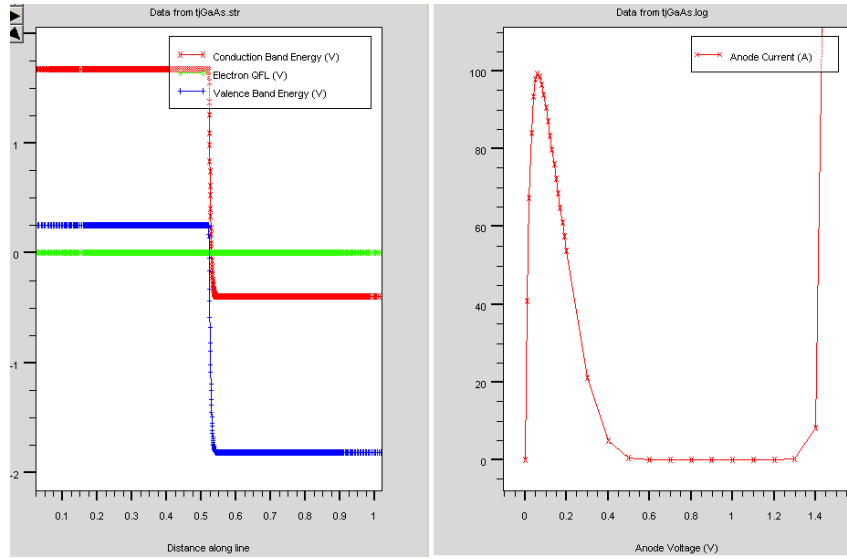


Figure 52. GaAs IV characteristics and energy band diagram ($p=3e20/cm^3$ $n=2e19/cm^3$) (A/cm^2 versus volts in a $1\mu m$ thick junction).

2. InGaP Tunnel Junction

a. p-region variation:

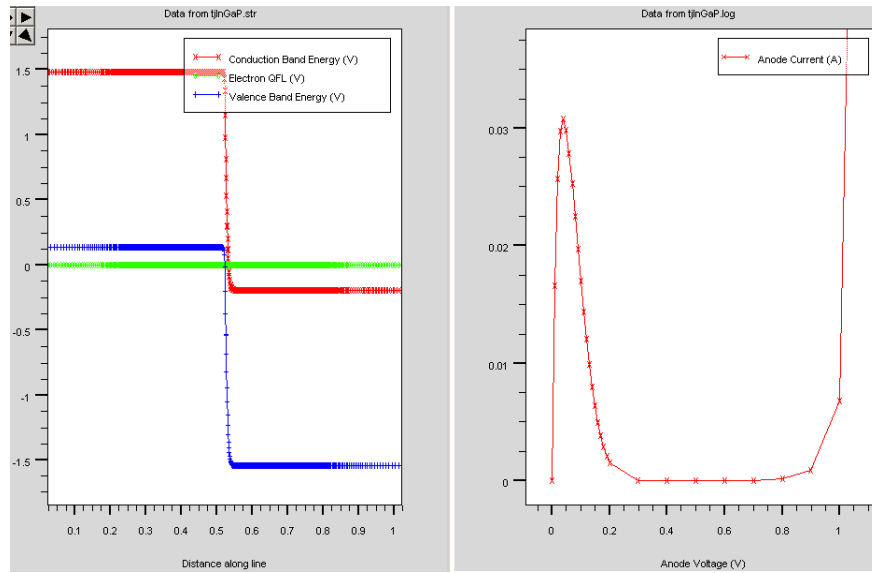


Figure 53. InGaP IV characteristics and energy band diagram ($p = 8e19/cm^3$ $n = 9e18/cm^3$) (A/cm^2 versus volts in a $1\mu m$ thick junction).

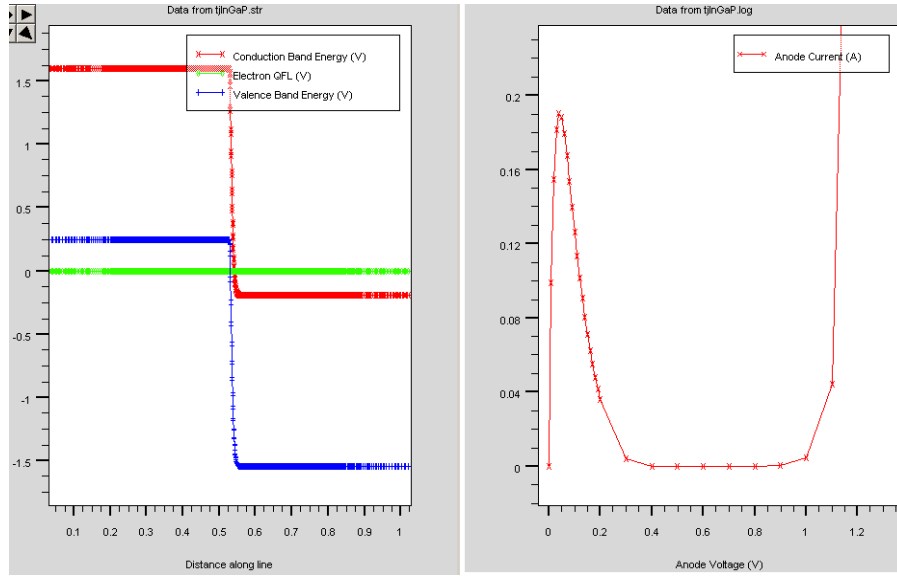


Figure 54. InGaP IV characteristics and energy band diagram ($p = 2e20/\text{cm}^3$ $n = 9e18/\text{cm}^3$) (A/cm^2 versus volts in a $1\mu\text{m}$ thick junction).

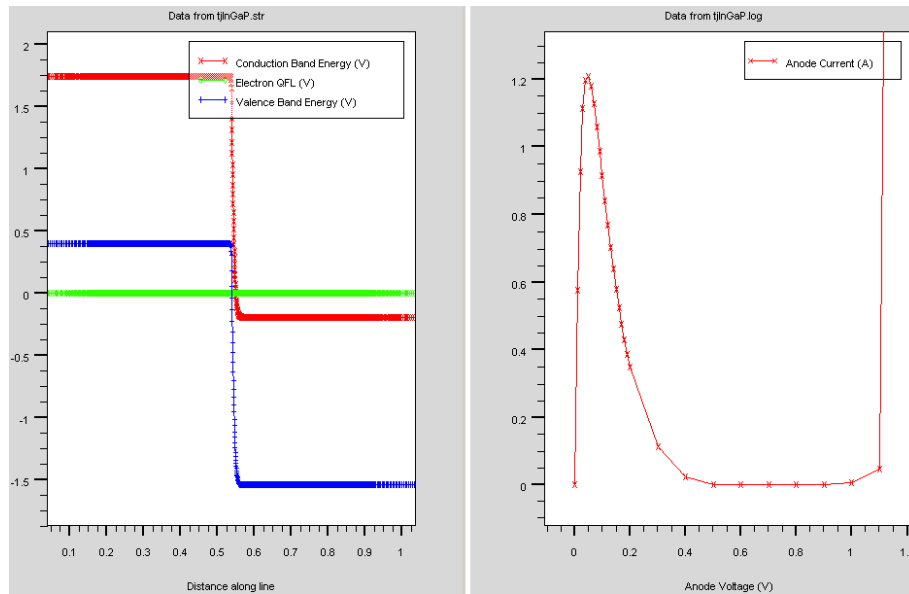


Figure 55. InGaP IV characteristics and energy band diagram ($p = 4e20/\text{cm}^3$ $n = 9e18/\text{cm}^3$) (A/cm^2 versus volts in a $1\mu\text{m}$ thick junction).

b. n-region variation:

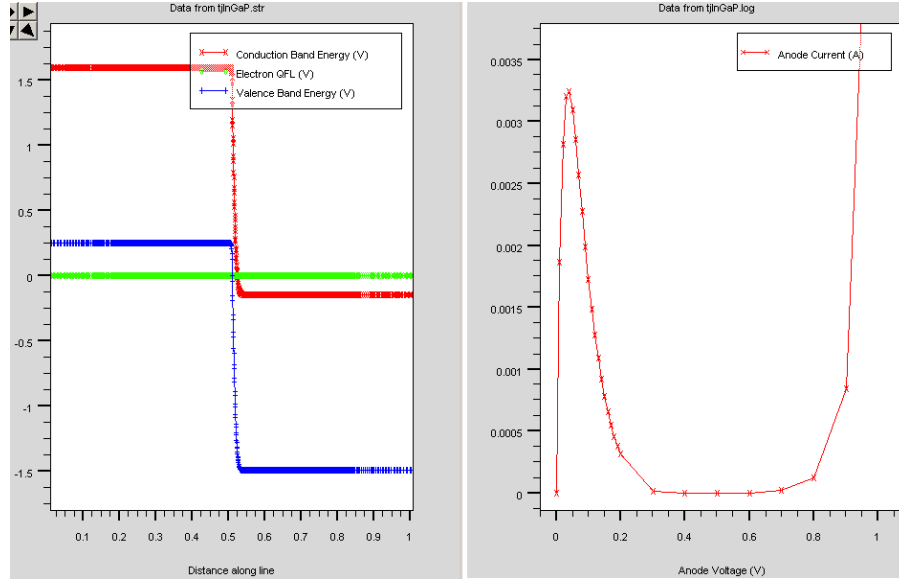


Figure 56. InGaP IV characteristics and energy band diagram ($p = 2e20/\text{cm}^3$ $n = 6e18/\text{cm}^3$) (A/cm^2 versus volts in a $1\mu\text{m}$ thick junction).

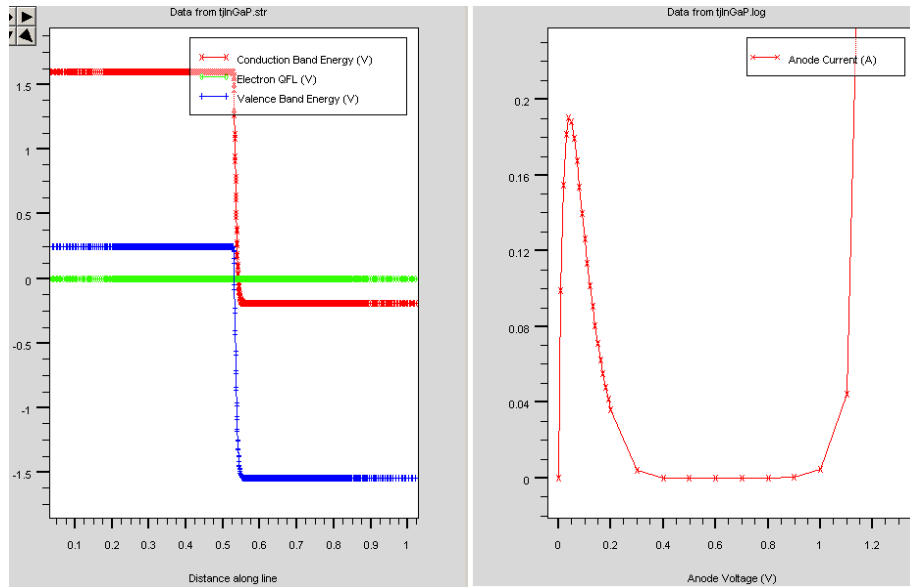


Figure 57. InGaP IV characteristics and energy band diagram ($p = 2e20/\text{cm}^3$ $n = 9e18/\text{cm}^3$) (A/cm^2 versus volts in a $1\mu\text{m}$ thick junction).

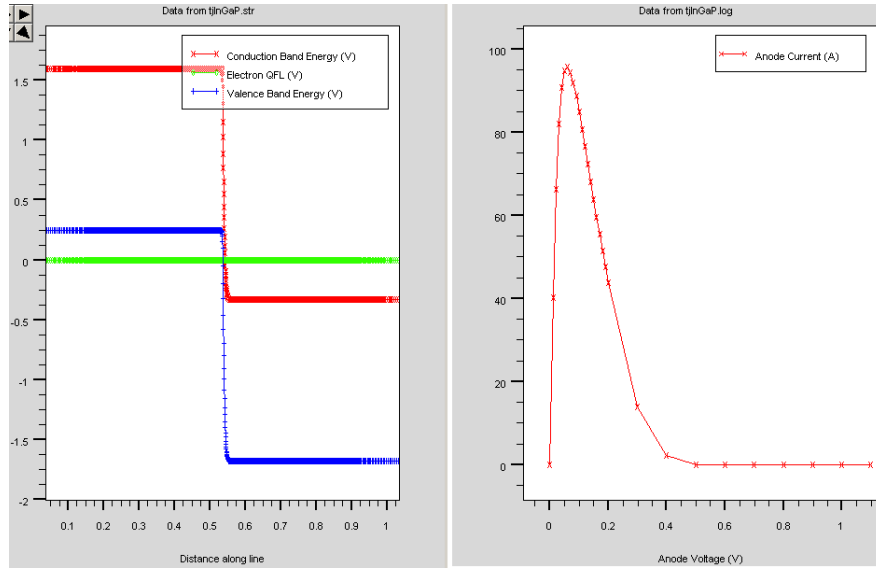


Figure 58. InGaP IV characteristics and energy band diagram ($p = 2 \times 10^{20} \text{ cm}^{-3}$, $n = 2 \times 10^{19} \text{ cm}^{-3}$) (A/cm^2 versus volts in a $1 \mu\text{m}$ thick junction).

C. SUMMARY

With the characteristic tunnel junction curve successfully modeled, I chose to take my research one step further and implement the tunnel junction into a solar cell simulation to verify the operation which will be discussed in the next chapter.

THIS PAGE INTENTIONALLY LEFT BLANK

VII. SOLAR CELL IMPLEMENTATION

The solar cell implementation was based on research completed by Panayiotis Michalopoulos [2] in 2002. Michalopoulos was a student of Prof. Sherif Michael at the Naval Postgraduate School and his research was developed using Silvaco software.

A. SOLAR RADIATION

The sun's energy is derived from nuclear fusion reactions where 6×10^{11} kg of hydrogen (H_2) is converted to helium (He) every second. The mass lost due to the conversion is approximately 4×10^3 kg. The energy produced by this loss can be determined by Einstein's famous mass-energy equation ($E=mc^2$) and is found to be 4×10^{20} J. This energy is emitted as electromagnetic radiation primarily at wavelengths from the ultraviolet to infrared and radio spectra (0.2 - $3\mu m$) [12].

The intensity of the sun's energy depends on the location of where it is measured. Outside the earth's atmosphere, the intensity is measured to be approximately $1365 W/m^2$ which produces a specific spectral response referred to as air mass zero (AM0). As the energy transits the earth's atmosphere, it is attenuated by ultraviolet absorption due to ozone, scattering due to airborne dust, and infrared absorption due to water vapor. AM1 and AM1.5 is used for terrestrial applications with incident solar power ranging from 925 to $963 W/m^2$.

B. I-V CURVE

As discussed in Chapter II, an electron must release energy to go from an outer shell (higher energy state) to an inner shell (lower energy state). Conversely, if a certain level of energy is absorbed, such as solar energy, an electron may transit from an inner shell to an outer shell or valence shell. In an intrinsic semiconductor this creation of carriers leads to an increase in conductivity. However, when a p-n junction is formed in a semiconductor the carriers will separate to create electron hole pairs (EHPs). The minority carrier will be swept across the junction due to the electrostatic field formed by the depletion region and the excess majority carriers created by the photogeneration will

develop a voltage differential between the two regions. If the junction is then connected to a load, current will flow (photocurrent). This phenomenon is known as photovoltaics because of the voltage potential generated by the photon (solar) energy.

As photons generate EHPs in a p-n junction, the standard diode dark current characteristic (Figure 59a-blue) is shifted down to produce the illuminated current characteristic (Figure 59a-red). Because a solar cell is usually presented as a power supply, the illuminated characteristic is most often reflected across the x-axis to show that the photocurrent conventionally flows in the opposite direction of the standard diode current (Figure 7.1b).

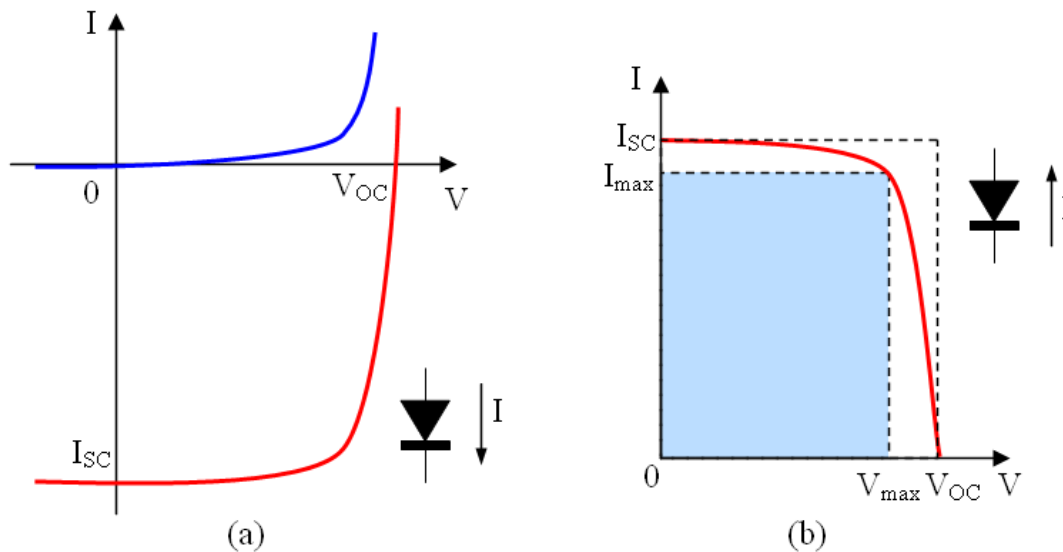


Figure 59. (a) Dark (blue) and illuminated (red) current characteristic curve of the solar cell. (b) Solar cell current characteristic curve with FF.

The number of EHPs generated in the semiconductor is proportional to the photons entering the semiconductor. However, many of the EHPs recombine inside the material before it is collected and are therefore not used to produce photocurrent. Thus, the maximum obtained power ($P_{obtained}$) is less than the maximum theoretical power

(P_{theory}). The ratio of obtained power to theoretical power is called fill factor or FF (Eqn. 7.1). The FF can be seen graphically in Figure 59 (b).

$$FF = \frac{P_{\text{obtained}}}{P_{\text{theory}}} = \frac{I_{\text{max}} V_{\text{max}}}{I_{\text{SC}} V_{\text{OC}}} \quad \text{Eqn. 7.1}$$

The power conversion efficiency (η) of a solar cell is given as the ratio of the maximum realized power to the incident power (P_{inc}).

$$\eta = \frac{P_{\text{max}}}{P_{\text{inc}}} = \frac{I_{\text{SC}} V_{\text{OC}} FF}{P_{\text{inc}}} \quad \text{Eqn. 7.2}$$

To maximize the power conversion efficiency, the FF, V_{oc} and I_{sc} must be optimized.

C. SINGLE CELL

Initially a single cell for each material in the multi-junction cell was modeled in ATLAS[®]. This simulation was based on the code already developed for a Naval Postgraduate School thesis by Panayiotis Michalopoulos in March 2002. Both cells were illuminated at AM0. The doping levels and thicknesses are illustrated in Figure 60 and 62 followed by their corresponding I-V curve (Figures 61 and 63).

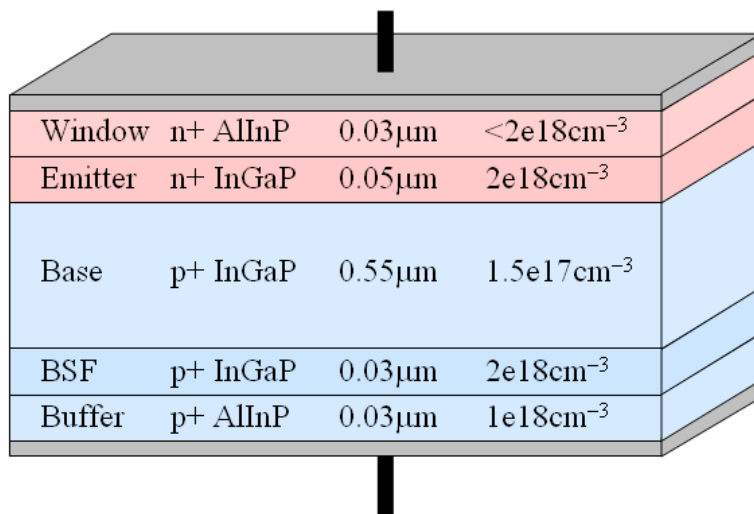


Figure 60. Optimized InGaP cell structure.

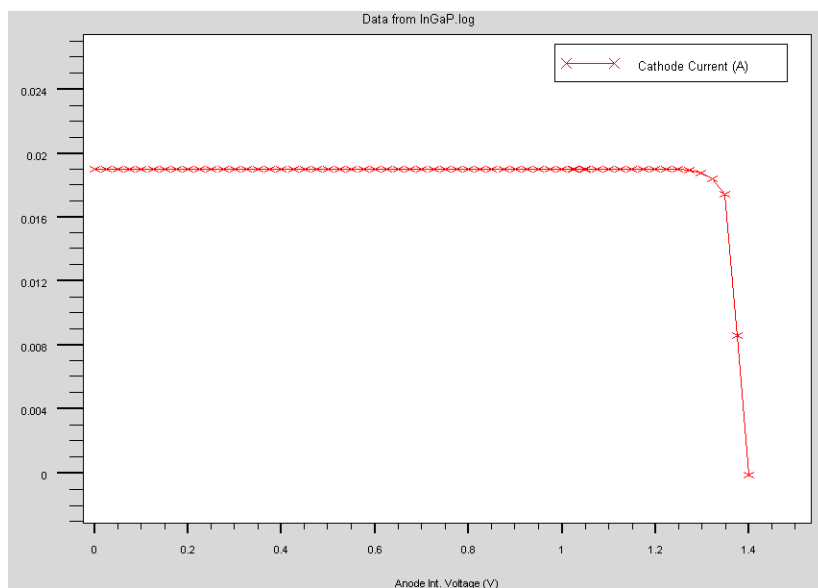


Figure 61. Optimized InGaP I-V curve. (A/cm^2 versus voltage).

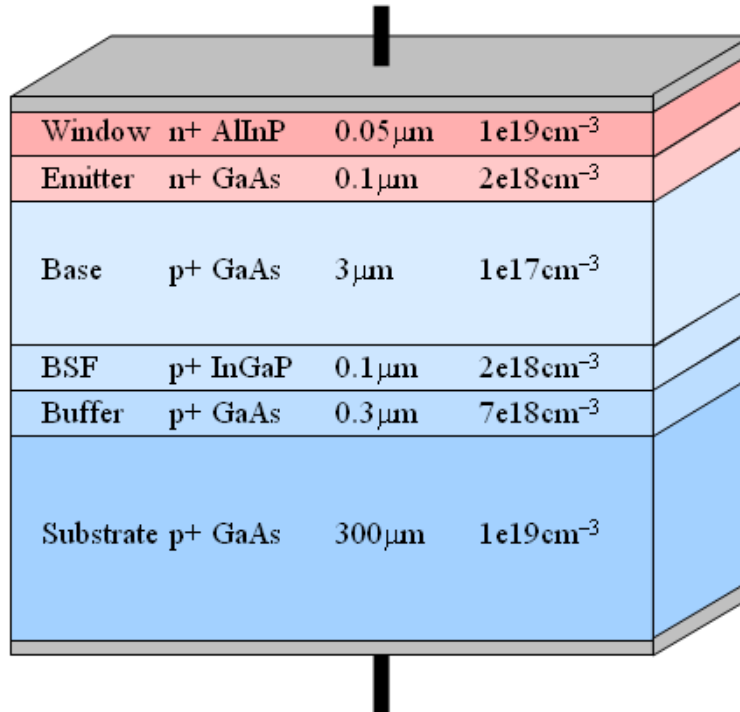


Figure 62. Optimized GaAs cell structure.

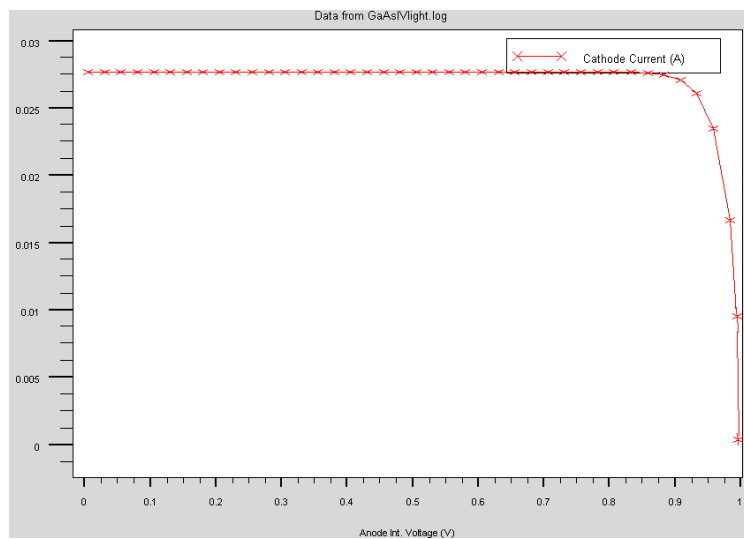


Figure 63. Optimized GaAs I-V curve. (A/cm^2 versus voltage).

The InGaP cell achieved a $V_{OC} = 1.43V$ and an $I_{SC} = 19mA/cm^2$. The GaAs cell achieved a $V_{OC} = 1.1V$ and an $I_{SC} = 27.4mA/cm^2$. Both cells were successfully modeled with 5% higher power than published data and 2% higher power than the results achieved by Michalopoulos [2].

With the single cells successfully modeled, the tunnel junction was implemented into the ATLAS[®] code.

D. MULTI CELLS

Similar to the single solar cells, the multi-junction cell in Figure 64 was illuminated at AM0 and the I-V curve was recorded (Figure 65).

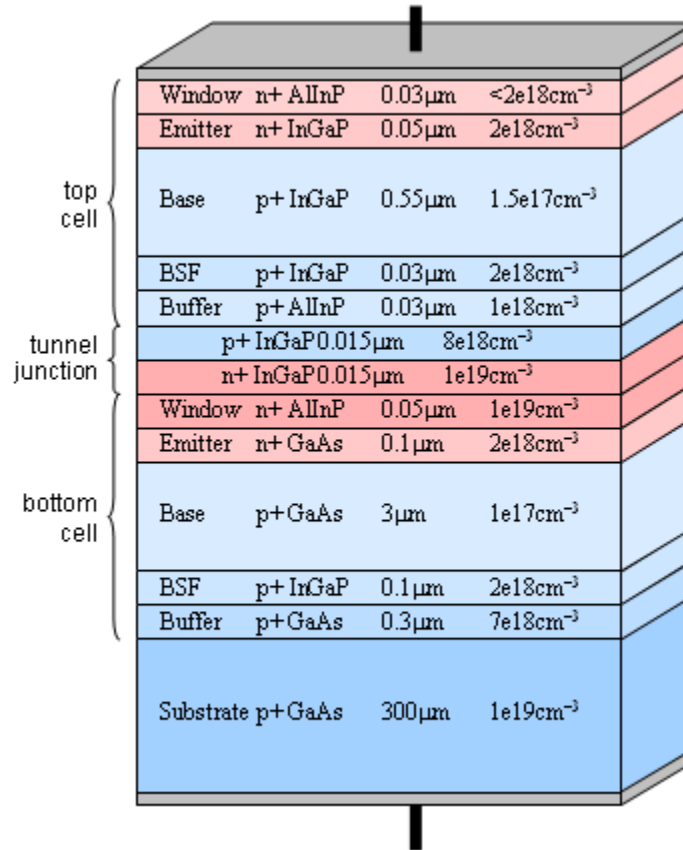


Figure 64. Multi-junction solar cell (InGaP/GaAs) with tunnel junction.

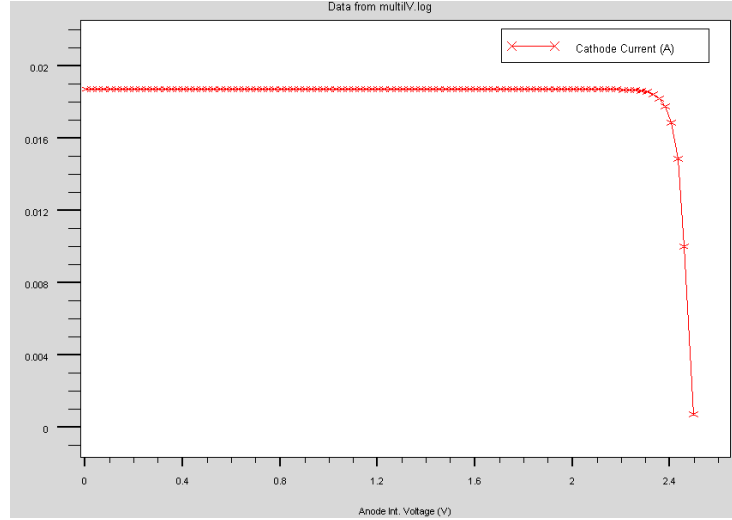


Figure 65. Multi-junction solar cell (InGaP/GaAs) I-V curve. (A/cm^2 versus voltage).

The multi-junction solar cell model achieved a $V_{OC} = 2.5\text{V}$ and an $I_{SC} = 18.7\text{mA}/\text{cm}^2$. As expected, the voltage is the sum of the two cells in the single cell models accounting for the small voltage drop across the tunnel junction. Ideally, both cells would generate the same current as in the single cell model and the realized current in the multi-junction cell would be the lower of the two. However, because the higher energy photons are absorbed by the InGaP top-cell, the GaAs bottom-cell is not able to generate as many EHPs and therefore realizes a slightly smaller current than ideal.

Taking the research one step further, the tunnel junction was implemented in the optimized multi-junction cell model. This was done so that the modeled output could be compared to empirical data in [3]. The optimized cell has an antireflective coating to absorb a greater number of photons and a back surface reflector to reflect some of the unutilized photons back into the semiconductor material. These additions help to create more EHPs and ultimately a higher current and power density.

Experimental data for an InGaP/GaAs photovoltaic cell produced a $V_{OC} = 2.488\text{V}$ and an $I_{SC} = 23\text{mA}/\text{cm}^2$ [3]. The optimized multi-junction cell model achieved a $V_{OC} = 2.5\text{V}$ and an $I_{SC} = 22\text{mA}/\text{cm}^2$ with a $FF = 84\%$ and $\eta = 29\%$ (Figure 66). This is only

3.8% greater power density than the experimental data and demonstrates the ability to model a tunnel junction for use in photovoltaic optimization.

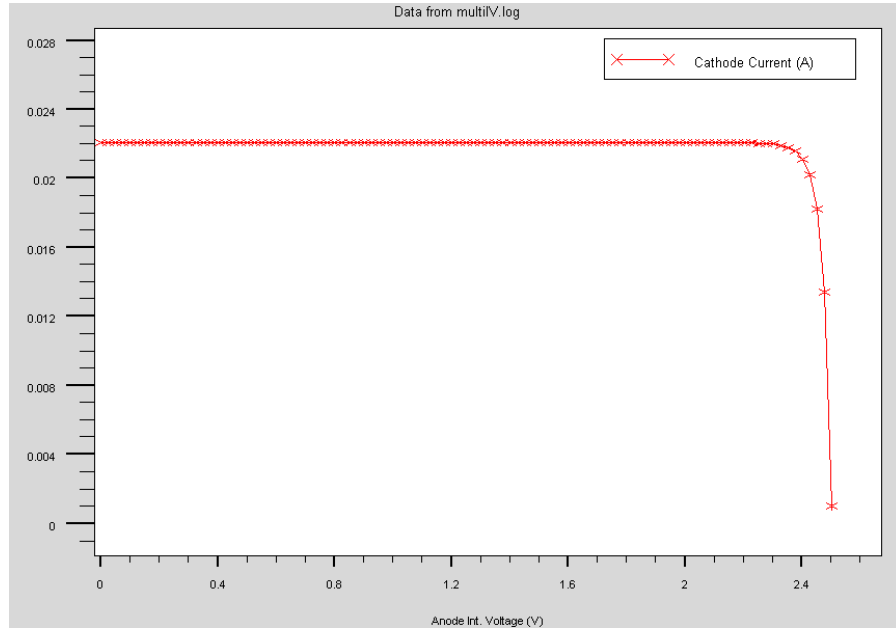


Figure 66. Optimized multi-junction solar cell (InGaP/GaAs) I-V curve.
(A/cm² versus voltage)

VIII. RECOMMENDATIONS AND CONCLUSION

A. RECOMMENDATIONS

1. Physical Experiment

The tunnel junction model presented here has produced very promising results. For this research the most important characteristic of the tunnel junction is the forward bias electron tunneling which was successfully modeled using Silvaco Inc's ATLAS[®] software. Unfortunately, time and resources did not allow for a physical model comparison. Although an implemented junction was compared to empirical values, the tunnel itself was only compared to theoretical values and responses based on mathematical models.

After further refinement and modeling, it is recommended that a project be funded to produce a junction with the precise specifications so that it may be tested and compared to the modeled parameters. Developing a more efficient tunnel junction and continuing to test the accuracy of the models, will lead to the development of more efficient solar cells.

2. Other Software

Throughout this study, a number of competing software programs were used in an effort to model the forward bias response of a tunnel junction. Some were geared more toward other aspects of the semiconductor industries such as MEMs design or computer architecture and were therefore difficult to use to implement a tunnel junction into a solar cell. Other programs were solar cell centric yet did not have the capacity or tools to realize the quantum tunneling effect of the degenerately doped junction.

There are other software packages available that are comparable to Silvaco's ATLAS[®] and would be beneficial to this research. It is recommended that the utility of these software packages be explored and compared.

3. Temperature and Radiation Effects

The use of photovoltaics in space applications is very important. Therefore, the tunnel junction should be adapted and tested under extreme conditions to ensure the accuracy of the model. The effects of temperature and radiation on a tunnel junction should be explored to ensure no anomalies exist.

B. CONCLUSION

The value of using simulation software such as ATLAS[®] to model semiconductors has revolutionized the semiconductor industry. Not only are time and money saved by minimizing the need to manufacture and test changes to a design, but efficiency is being pushed to the limit.

It has been have shown throughout this thesis that it is possible to model such effects as quantum tunneling in a photovoltaic solar cell. To this point, the tunnel junction in a multi-junction cell was modeled as a vacuum to insulate the layers, then hardwired to pass the current between cells. Although this is effective, the cell being modeled is not fully optimized.

A paper entitled “*Multi-Junction Photovoltaic Model Optimizations for Space and Solar Concentrator Applications*” [13], was presented by Professor Michael and the author on September 3, 2008, at the 23rd European Photovoltaic Solar Energy Conference, that was held in Valencia, Spain. The paper focused on the application of multi-junction photovoltaic cells using tunnel junction technology for use in space applications. The tunnel junction modeling has the potential to push photovoltaic technology to a new level of optimization and power density and it is necessary to model this phenomenon accurately.

APPENDIX. ATLAS[®] SOURCE CODE

A. MAIN STRUCTURE

```
go atlas
# Definition of constants
# Mesh
# X-Mesh
# Y-Mesh
# Regions
# Electrodes
# Doping
# QT Mesh
# Material properties
# Models
# Light beams
# Solving
```

B. TUNNEL JUNCTION

```
go atlas
```

1. X-Mesh

```
mesh width=1e7
#x-mesh
x.mesh loc=0      spac=1
x.mesh loc=10     spac=1
```

2. Y-Mesh

```
y.mesh loc=0.0     spac=0.01
y.mesh loc=0.25    spac=0.001
y.mesh loc=0.75    spac=0.001
y.mesh loc=1.0     spac=0.01
```

3. Regions

```
region num=1 material=InGaP x.min=0 x.max=10 y.min=0.5 y.max=1
region num=2 material=InGaP x.min=0 x.max=10 y.min=0 y.max=0.5
```

4. Electrodes

```
elec name=anode      top
elec name=cathode    bottom
```

```
doping uniform p.type conc=2e20 y.max=0.5
doping uniform n.type conc=2e19 y.min=0.5
```

5. QT-Mesh

```
qtx.mesh loc=0      spac=1
qtx.mesh loc=10     spac=1

qty.mesh loc=0.35   spac=0.01
qty.mesh loc=0.5    spac=0.0005
qty.mesh loc=0.65   spac=0.01
```

6. Models/Output

```
models temperature=300 srh fermi ni.fermi print \
qtunn.dir=0 bbt.nonlocal bbt.forward bbt.nlderivs

output band.temp traps u.srh taurn taurp band.param con.band val.band \
qfn qfp

log outfile=tjInGaP.str
solve init
save outfile=tjInGaP.str
tonyplot tjInGaP.str

method climit=1.0 dvmax=0.05

solve init
solve prev
log outfile=tjInGaP.log
```

7. Solve

```
solve name=anode vanode =-1 vstep=0.1 vfinal=0.0
solve name=anode vanode =0.0 vstep=0.01 vfinal=0.2
solve name=anode vanode =0.2 vstep=0.1 vfinal=1.1
tonyplot tjInGaP.log
```

8. Plot

```
save outfile=tjInGaP.str
tonyplot tjInGaP.str
```

C. COMMON SECTIONS

1. X-Mesh

```
mesh space.mult=1
# X-Mesh: surface=500 um2 = 1/200,000 cm2
x.mesh loc=-250 spac=50
```

```
x.mesh loc=0 spac=10
x.mesh loc=250 spac=50
```

2. Material Properties

```
material TAUN=1e-7 TAUP=1e-7 COPT=1.5e-10 AUGN=8.3e-32 AUGP=1.8e-31
```

```
# Vacuum
material material=Vacuum real.index=3.3 imag.index=0
```

```
# Ge
material material=Ge EG300=0.67 PERMITTIVITY=16 AFFINITY=4
material material=Ge MUN=3900 MUP=1800
material material=Ge NC300=1.04e19 NV300=6e18
material material=Ge index.file=Ge.opt
```

```
# GaAs
material material=GaAs EG300=1.42 PERMITTIVITY=13.1 AFFINITY=4.07
material material=GaAs MUN=8800 MUP=400
material material=GaAs NC300=4.7e17 NV300=7e18
material material=GaAs index.file=GaAs.opt
```

```
# InGaP
material material=InGaP EG300=1.9 PERMITTIVITY=11.62 AFFINITY=4.16
material material=InGaP MUN=1945 MUP=141
material material=InGaP NC300=1.3e20 NV300=1.28e19
material material=InGaP index.file=InGaP-1.9.opt
```

```
# AlInP (=InAsP)
material material=InAsP EG300=2.4 PERMITTIVITY=11.7 AFFINITY=4.2
material material=InAsP MUN=2291 MUP=142
material material=InAsP NC300=1.08e20 NV300=1.28e19
material material=InAsP index.file=AlInP.opt
```

```
# AlInGaP (=InAlAsP)
material material=InAlAsP EG300=2.4 PERMITTIVITY=11.7 AFFINITY=4.2
material material=InAlAsP MUN=2150 MUP=141
material material=InAlAsP NC300=1.2e20 NV300=1.28e19
material material=InAlAsP index.file=AlInP.opt
```

3. Models

```
models fermi ni.fermi qtunn.dir=0 bbt.nonlocal bbt.forward bbt.nlderivs
      bbt.std
```

4. Light Beams

```
beam num=1 x.origin=0 y.origin=-5 angle=90 \
      power.file=AM0silv.spec wavel.start=0.21 wavel.end=4 wavel.num=50
```

D. INGAAS / GAAS SINGLE AND DUAL JUNCTION CELL

1. Bottom Cell (GaAs)

a. Y-Mesh

```
# Vacuum
y.mesh loc=-0.15 spac=0.001
# Window (0.05 um)
y.mesh loc=-0.1 spac=0.01
# Emitter (0.1 um)
y.mesh loc=0 spac=0.01
# Base (3 um)
y.mesh loc=1.5 spac=0.3
y.mesh loc=3 spac=0.01
# BSF (0.1 um)
y.mesh loc=3.1 spac=0.01
# Buffer (0.3 um)
y.mesh loc=3.4 spac=0.05
# Substrate (300 um)
y.mesh loc=303.4 spac=50
```

b. Regions

```
# Window AlInP (=InAsP)
region num=1 material=InAsP x.min=-250 x.max=250 y.min=-0.15 y.max=-0.1
# Emitter
region num=2 material=GaAs x.min=-250 x.max=250 y.min=-0.1 y.max=0
# Base
region num=3 material=GaAs x.min=-250 x.max=250 y.min=0 y.max=3
# BSF
region num=4 material=InGaP x.min=-250 x.max=250 y.min=3 y.max=3.1
# Buffer
region num=5 material=GaAs x.min=-250 x.max=250 y.min=3.1 y.max=3.4
# Substrate
region num=6 material=GaAs x.min=-250 x.max=250 y.min=3.4 y.max=303.4
```

c. Electrodes

```
electrode name=cathode x.min=-250 x.max=250 y.min=-0.15 y.max=-0.15
electrode name=anode x.min=-250 x.max=250 y.min=303.4 y.max=303.4
```

d. Doping

```
# Window
doping uniform region=1 n.type conc=1e19
# Emitter
doping uniform region=2 n.type conc=2e18
# Base
doping uniform region=3 p.type conc=1e17
# BSF
doping uniform region=4 p.type conc=2e18
```

```
# Buffer
doping uniform region=5 p.type conc=7e18
# Substrate
doping uniform region=6 p.type conc=1e19
```

e. Solving

```
method newton maxtraps=10 itlimit=100 climit=1 dvmax=0.05
solve initial
solve bl=0.9

log outf=multiIV.log
solve vanode=0.0 name=anode vstep=0.025 vfinal=2.7

extract init infile="multiIV.log"
extract name="Jsc" y.val from curve(v."anode", i."anode") where
    x.val=0.0
extract name="Voc" x.val from curve(v."anode", i."anode") where
    y.val=0.0
```

2. Top Cell (InGaP)

a. Y-Mesh

```
# Vacuum
y.mesh loc=-0.87 spac=0.003
# Window (0.03 um)
y.mesh loc=-0.84 spac=0.003
# Emitter (0.05 um)
y.mesh loc=-0.79 spac=0.003
# Base (0.55 um)
y.mesh loc=-0.5 spac=0.1
y.mesh loc=-0.24 spac=0.003
# BSF (0.03 um)
y.mesh loc=-0.21 spac=0.003
# Buffer (0.03 um)
y.mesh loc=-0.18 spac=0.002
```

b. Regions

```
# Window AlInP (=InAsP)
region num=1 material=InAsP x.min=-250 x.max=250 y.min=-0.87 y.max=-
0.84
# Emitter
region num=2 material=InGaP x.min=-250 x.max=250 y.min=-0.84 y.max=-
0.79
# Base
region num=3 material=InGaP x.min=-250 x.max=250 y.min=-0.79 y.max=-
0.24
# BSF
region num=4 material=InGaP x.min=-250 x.max=250 y.min=-0.24 y.max=-
0.21
```

```
# Buffer AlInP (=InAsP)
region num=5 material=InAsP x.min=-250 x.max=250 y.min=-0.21 y.max=-
0.18
```

c. Electrodes

```
electrode name=cathode x.min=-250 x.max=250 y.min=-0.87 y.max=-0.87
electrode name=anode x.min=-250 x.max=250 y.min=-0.18 y.max=-0.18
```

d. Doping

```
# Window
doping uniform region=1 n.type conc=1.95e18
# Emitter
doping uniform region=2 n.type conc=2e18
# Base
doping uniform region=3 p.type conc=1.5e17
# BSF
doping uniform region=4 p.type conc=2e18
# Buffer
doping uniform region=5 p.type conc=0.95e18
```

e. Solving

(1) I_{sc} and V_{oc}

```
method newton maxtraps=10 itlimit=100 climit=1 dvmax=0.05
solve initial
solve bl=0.9

log outf=multiIV.log
solve vanode=0.0 name=anode vstep=0.025 vfinal=2.7

extract init infile="multiIV.log"
extract name="Jsc" y.val from curve(v."anode", i."anode") where
    x.val=0.0
extract name="Voc" x.val from curve(v."anode", i."anode") where
    y.val=0.0
```

3. Stacked Cell

a. *Y-Mesh*

```
# Vacuum
y.mesh loc=-0.87 spac=0.003
# Window (0.03 um)
y.mesh loc=-0.84 spac=0.003
# Emitter (0.05 um)
y.mesh loc=-0.79 spac=0.003
# Base (0.55 um)
y.mesh loc=-0.5 spac=0.1
y.mesh loc=-0.24 spac=0.003
```

```

# BSF (0.03 um)
y.mesh loc=-0.21 spac=0.003
# Buffer (0.03 um)
y.mesh loc=-0.18 spac=0.002
# Vacuum (0.015 um)
y.mesh loc=-0.165 spac=0.002
# Vacuum (0.015 um)
y.mesh loc=-0.15 spac=0.001
# Window (0.05 um)
y.mesh loc=-0.1 spac=0.01
# Emitter (0.1 um)
y.mesh loc=0 spac=0.01
# Base (3 um)
y.mesh loc=1.5 spac=0.3
y.mesh loc=3 spac=0.01
# BSF (0.1 um)
y.mesh loc=3.1 spac=0.01
# Buffer (0.3 um)
y.mesh loc=3.4 spac=0.05
# Substrate (300 um)
y.mesh loc=303.4 spac=50

```

b. Regions

```

# Window AlInP (=InAsP)
region num=1 material=InAsP x.min=-250 x.max=250 y.min=-0.87 y.max=-
0.84
# Emitter
region num=2 material=InGaP x.min=-250 x.max=250 y.min=-0.84 y.max=-
0.79
# Base
region num=3 material=InGaP x.min=-250 x.max=250 y.min=-0.79 y.max=-
0.24
# BSF
region num=4 material=InGaP x.min=-250 x.max=250 y.min=-0.24 y.max=-
0.21
# Buffer AlInP (=InAsP)
region num=5 material=InAsP x.min=-250 x.max=250 y.min=-0.21 y.max=-
0.18
# Vacuum
region num=6 material=Vacuum x.min=-250 x.max=250 y.min=-0.18
y.max=-0.165
region num=7 material=Vacuum x.min=-250 x.max=250 y.min=-0.165
y.max=-0.15
# Window AlInP (=InAsP)
region num=8 material=InAsP x.min=-250 x.max=250 y.min=-0.15
y.max=-0.1
# Emitter
region num=9 material=GaAs x.min=-250 x.max=250 y.min=-0.1 y.max=0
# Base
region num=10 material=GaAs x.min=-250 x.max=250 y.min=0 y.max=3
# BSF
region num=11 material=InGaP x.min=-250 x.max=250 y.min=3 y.max=3.1
# Buffer
region num=12 material=GaAs x.min=-250 x.max=250 y.min=3.1 y.max=3.4

```

```
# Substrate
region num=13 material=GaAs x.min=-250 x.max=250 y.min=3.4 y.max=303.4
```

c. Electrodes

```
electrode name=cathode x.min=-250 x.max=250 y.min=-0.87 y.max=-0.87
electrode name=cc x.min=-250 x.max=250 y.min=-0.18 y.max=-0.18
electrode name=ee x.min=-250 x.max=250 y.min=-0.15 y.max=-0.15
electrode name=anode x.min=-250 x.max=250 y.min=303.4 y.max=303.4
```

d. Doping

```
# Window
doping uniform region=1 n.type conc=1.95e18
# Emitter
doping uniform region=2 n.type conc=2e18
# Base
doping uniform region=3 p.type conc=1.5e17
# BSF
doping uniform region=4 p.type conc=2e18
# Buffer
doping uniform region=5 p.type conc=0.95e18
# Window
doping uniform region=8 n.type conc=1e19
# Emitter
doping uniform region=9 n.type conc=2e18
# Base
doping uniform region=10 p.type conc=1e17
# BSF
doping uniform region=11 p.type conc=2e18
# Buffer
doping uniform region=12 p.type conc=7e18
# Substrate
doping uniform region=13 p.type conc=1e19
```

e. Solving

```
method newton maxtraps=10 itlimit=100 climit=1 dvmax=0.05
solve initial
solve bl=0.9
```

```
log outf=multiIV.log
solve vanode=0.0 name=anode vstep=0.025 vfinal=2.7
```

```
extract init infile="multiIV.log"
extract name="Jsc" y.val from curve(v."anode", i."anode") where
x.val=0.0
extract name="Voc" x.val from curve(v."anode", i."anode") where
y.val=0.0
```


4. Tunnel Junction

a. *Y-Mesh*

```
y.mesh loc=-0.18 spac=0.002
# Tunnel emitter (0.015 um)
y.mesh loc=-0.165 spac=0.002
# Tunnel base (0.015 um)
y.mesh loc=-0.15 spac=0.001
```

b. Regions

```
region num=1 material=InGaP x.min=-250 x.max=250 y.min=-0.18 y.max=-
0.165
region num=2 material=InGaP x.min=-250 x.max=250 y.min=-0.165 y.max=-
0.15
```

c. Electrodes

```
electrode name=cathode x.min=-250 x.max=250 y.min=-0.18 y.max=-0.18
electrode name=anode x.min=-250 x.max=250 y.min=-0.15 y.max=-0.15
```

d. Doping

```
doping uniform region=1 p.type conc=8e18
doping uniform region=2 n.type conc=1e19
```

e. QT Mesh

```
qtx.mesh loc=-250      spac=50
qtx.mesh loc=0         spac=10
qtx.mesh loc=250      spac=50

qty.mesh loc=-0.165    spac=.001
qty.mesh loc=-0.1575   spac=.0005
qty.mesh loc=-0.15     spac=.001
```

f. Solving

```
method newton maxtraps=10 itlimit=100 climit=1 dvmax=0.05
solve initial
solve bl=0.9
```

```
log outf=multiIV.log
solve vanode=0.0 name=anode vstep=0.025 vfinal=2.7
```

```
extract init infile="multiIV.log"
extract name="Jsc" y.val from curve(v."anode", i."anode") where
    x.val=0.0
extract name="Voc" x.val from curve(v."anode", i."anode") where
    y.val=0.0
```

5. MJ Cell

a. *Y-Mesh*

```
# Vacuum
y.mesh loc=-0.87 spac=0.003
# Window (0.03 um)
y.mesh loc=-0.84 spac=0.003
# Emitter (0.05 um)
y.mesh loc=-0.79 spac=0.003
# Base (0.55 um)
y.mesh loc=-0.5 spac=0.1
y.mesh loc=-0.24 spac=0.003
# BSF (0.03 um)
y.mesh loc=-0.21 spac=0.003
# Buffer (0.03 um)
y.mesh loc=-0.18 spac=0.002
# Tunnel emitter (0.015 um)
y.mesh loc=-0.165 spac=0.002
# Tunnel base (0.015 um)
y.mesh loc=-0.15 spac=0.001
# Window (0.05 um)
y.mesh loc=-0.1 spac=0.01
# Emitter (0.1 um)
y.mesh loc=0 spac=0.01
# Base (3 um)
y.mesh loc=1.5 spac=0.3
y.mesh loc=3 spac=0.01
# BSF (0.1 um)
y.mesh loc=3.1 spac=0.01
# Buffer (0.3 um)
y.mesh loc=3.4 spac=0.05
# Substrate (300 um)
y.mesh loc=303.4 spac=50
```

b. **Regions**

```
# Window AlInP (=InAsP)
region num=1 material=InAsP x.min=-250 x.max=250 y.min=-0.87 y.max=-0.84
# Emitter
region num=2 material=InGaP x.min=-250 x.max=250 y.min=-0.84 y.max=-0.79
# Base
region num=3 material=InGaP x.min=-250 x.max=250 y.min=-0.79 y.max=-0.24
# BSF
region num=4 material=InGaP x.min=-250 x.max=250 y.min=-0.24 y.max=-0.21
# Buffer AlInP (=InAsP)
region num=5 material=InAsP x.min=-250 x.max=250 y.min=-0.21 y.max=-0.18

# Tunnel emitter
```

```

region num=6 material=InGaP x.min=-250 x.max=250 y.min=-0.18
    y.max=-0.165
# Tunnel base
region num=7 material=InGaP x.min=-250 x.max=250 y.min=-0.165
    y.max=-0.15

# Window AlInP (=InAsP)
region num=8 material=InAsP x.min=-250 x.max=250 y.min=-0.15 y.max=-0.1
# Emitter
region num=9 material=GaAs x.min=-250 x.max=250 y.min=-0.1 y.max=0
# Base
region num=10 material=GaAs x.min=-250 x.max=250 y.min=0 y.max=3
# BSF
region num=11 material=InGaP x.min=-250 x.max=250 y.min=3 y.max=3.1
# Buffer
region num=12 material=GaAs x.min=-250 x.max=250 y.min=3.1 y.max=3.4
# Substrate
region num=13 material=GaAs x.min=-250 x.max=250 y.min=3.4 y.max=303.4

```

c. Electrodes

```

electrode name=cathode x.min=-250 x.max=250 y.min=-0.87 y.max=-0.87
electrode name=anode x.min=-250 x.max=250 y.min=303.4 y.max=303.4

```

d. Doping

```

# Window
doping uniform region=1 n.type conc=1.95e18
# Emitter
doping uniform region=2 n.type conc=2e18
# Base
doping uniform region=3 p.type conc=1.5e17
# BSF
doping uniform region=4 p.type conc=2e18
# Buffer
doping uniform region=5 p.type conc=0.95e18
# Tunnel
doping uniform region=6 p.type conc=8e18
# Tunnel
doping uniform region=7 n.type conc=1e19
# Window
doping uniform region=8 n.type conc=1e19
# Emitter
doping uniform region=9 n.type conc=2e18
# Base
doping uniform region=10 p.type conc=1e17
# BSF
doping uniform region=11 p.type conc=2e18
# Buffer
doping uniform region=12 p.type conc=7e18
# Substrate
doping uniform region=13 p.type conc=1e19

```

e. Solving

```
method newton maxtraps=10 itlimit=100 climit=1 dvmax=0.05
solve initial
solve b1=0.9

log outf=multiIV.log
solve vanode=0.0 name=anode vstep=0.025 vfinal=2.7

extract init infile="multiIV.log"
extract name="Jsc" y.val from curve(v."anode", i."anode") where
    x.val=0.0
extract name="Voc" x.val from curve(v."anode", i."anode") where
    y.val=0.0
```

LIST OF REFERENCES

- [1] Renewable Resource Data Center (www.rredc.nrel.gov). Last accessed on August 10, 2008.
- [2] P. Michalopoulos, "A Novel Approach for the Development and Optimization of State-of-the-Art Photovoltaic Devices Using Silvaco," Master's Thesis, Naval Postgraduate School, Monterey, California, 2002.
- [3] T Agui, T. Takamoto, E. Ikeda, and H. Kurita, "High-efficient dual-junction InGaP/GaAs solar cells with improved tunnel interconnect," Indium Phosphide and Related Materials, 1998 International Conference on, pp 203-206, 1998.
- [4] S. M. Sze, *Semiconductor Devices*, 2nd edition, John Wiley & Sons, Inc, 2001.
- [5] R. F. Pierret, *Semiconductor Device Fundamentals*, Addison-Wesley Publishing Company, Inc., 1996.
- [6] Oklahoma State University Solid State/Chemistry Website (www.okstate.edu/jgelder/solstate.html). Last accessed on July 2, 2008.
- [7] S. M. Sze, *Physics of Semiconductor Devices*, 2nd edition, John Wiley & Sons, Inc, 1981.
- [8] D. A. Fraser, *The Physics of Semiconductor Devices*, Clarendon Press – Oxford, 1986.
- [9] D. A. Neamen, *Semiconductor Physics and Devices*, McGraw-Hill companies, Inc, 2003.
- [10] SILVACO International website (www.silvaco.com). Last accessed on August 15, 2008.
- [11] S. M. Sze, *Modern Semiconductor Device Physics*, John Wiley & Sons, Inc, 1998.
- [12] A. D. Bates, "Novel Optimizatoin Techniques for Multijunction Solar Cell Design Using Silvaco Atlas," Master's Thesis, Naval Postgraduate School, Monterey, California, 2005.
- [13] S. Michael and J. Lavery, "Multi-Junctoin Photovoltaic model Optimizatoins for Space and Solar Concentrator Applications," *Proceedings of the 23rd European Photovoltaic Solar Energy Conference, Valencia, Spain, September 1-5, 2008*.
- [14] M. Shur, *Physics of Semiconductor Devices*, Prentice–Hall, Inc, 1990.
- [15] R. P. Feynman, *The Feynman Lectures on Physics*, Volume I, Addison-Wesley Publishing Company, 1989.
- [16] Georgia State University hyperphysics website (<http://hyperphysics.phy-astr.gsu.edu>). Last accessed on May 28, 2008.

- [17] T. Takamoto, I. Kurita, and H. Ohmori, “*High efficiency InGaP solar cells for InGaP/GaAs tandem cell application*,” Photovoltaic Energy Conversion in 1994, Volume: 2, pp. 1729–1732, 1994.
- [18] B. Cavicchi, D. Krut, D. Lillington, S. Kurtz, and J. Olson, “*The design and evaluation of dual-junction GaInP/sub 2//GaAs solar cells for space applications*,” Photovoltaic Specialists Conference in 1991, pp. 63-67, vol. 1, 1991.
- [19] D. Lillington, H. Cotal, J. Ermer, D. Friedman, T. Moriarty, and A. Duda, “*32.3% efficient triple junction GaInP/sub 2//GaAs/Ge concentrator solar cells*,” Energy Conversion Engineering Conference and Exhibit in 2000, (IECEC) 35th Intersociety, Volume: 1 , 2000, pp. 516 -521.
- [20] J. Granata, J. Ermer, P. Hebert, M. Haddad, R. King, D. Krut , J. Lovelady, M. Gillanders, N. Karam, and B. Cavicchi, “*Triple-junction GaInP/GaAs/Ge solar cells-production status, qualification results and operational benefits*,” Photovoltaic Specialists Conference in 2000, pp. 1181 -1184.
- [21] R. King, N. Karam, J. Ermer, N. Haddad, P. Colter, T. Isshiki, H. Yoon, H. Cotal, D. Josli, D. Krut, R. Sudharsanan, K. Edmondson, B. Cavicchi, and D. Lillington, “*Next-generation, high-efficiency III-V multijunction solar cells*,” Photovoltaic Specialists Conference in 2000, Conference Record of the Twenty-Eighth IEEE, 2000, pp 998-1001.
- [22] Department of Energy (www.doe.gov). Last accessed on June 24, 2008.
- [23] J. Slotboom, “The PN Product in Silicon,” *Solid State Electronics* 20 (1977): 279-283.
- [24] I. Vurgaftman, J. Meyer, and L. Ram–Mohan, “Band parameters for III–V compound semiconductors and their alloys,” *Applied Physics Review, Journal of Applied Physics*, vol. 89, number 11, June 1, 2001, pp. 5815–5875.
- [25] P. Sharps, J. Hills, and H. Hou, “AlGaAs/InGaAlP TUNNEL JUNCTIONS for MULTI-JUNCTION SOLAR CELLS,” EMCORE Photovoltaics. IEEE 2000.

INITIAL DISTRIBUTION LIST

1. Defense Technical Information Center
Ft. Belvoir, Virginia
2. Dudley Knox Library
Naval Postgraduate School
Monterey, California
3. Chairman, Department of Electrical and Computer Engineering
Naval Postgraduate School
Monterey, California
4. Dr. Sherif Michael, Code EC/Mi
Department of Electrical and Computer Engineering
Monterey, California
5. Dr. Todd Weatherford, Code EC/Wt
Department of Electrical and Computer Engineering
Monterey, California